Stochastic Dynamics Simulations of Surfactant Self-Assembly

by

Friedrich K. von Gottberg

Submitted to the Department of Chemical Engineering
in partial fulfillment of the requirements for the degree of

Doctor of Philosophy

at the

MASSACHUSETTS INSTITUTE OF TECHNOLOGY

June, 1997

Author .....
Department of Chemical Engineering
May 12, 1997

Certified by .....
T. Alan Hatton
Ralph Landau Professor of Chemical Engineering Practice
Thesis Supervisor

Certified by .....
Kenneth A. Smith
Edwin R. Gilliland Professor of Chemical Engineering
Thesis Supervisor

Accepted by .....
Robert E. Cohen
St. Laurent Professor of Chemical Engineering
Chairman, Committee for Graduate Students

Stochastic Dynamics Simulations of Surfactant Self-Assembly

by

Friedrich K. von Gottberg

Submitted to the Department of Chemical Engineering on
May 12, 1997, in partial fulfillment of the requirements for
the degree of Doctor of Philosophy in Chemical Engineering.

Abstract

Amphiphiles self-assemble in solution to form micelles and other ordered structures. The equilibrium and dynamic properties of these systems are important in such diverse areas as detergency, bioprocessing, separations, and emulsification. The dynamic processes occurring in bulk micellar solutions and at interfaces in surfactant-laden systems have been studied in this work to probe factors affecting the rates of interfacial solubilisation and micelle formation and dissolution.

In Part I of the thesis, the self-assembly of short amphiphilic molecules of type A_2B_2 (A =hydrophilic, B=hydrophobic) is investigated using Stochastic Dynamics simulations (SD) with a scalar frictional coefficient. The utility of SD simulations is that the computationally intensive solvent effects are accounted for in an approximate manner via a stochastic noise term and a solvent-modified interaction potential. Equilibrium properties were calculated and explained in the context of existing thermodynamic theories. Spherical micelles are observed to form and the effect of temperature and total surfactant concentration on the structural properties are investigated. Above the critical micelle concentration, a decline in the free surfactant concentration is observed, contrary to existing theories dealing with micelle formation. By incorporating excluded volume effects into the theory for micelle formation, the observed behavior can be explained.

The dynamics involved in self-assembly were also investigated for the model amphiphile A_2B_2. Temperature jump computer "experiments" were performed and the evolution of the system to its new equilibrium state was monitored. The results were interpreted based on the Aniansson and Wall theory of micellar kinetics. To solve the resulting set of flux equations describing the evolution of the number of aggregates, the initial and final micelle size distributions were required, together with the micellar dissociation rate constant. The transient behavior predicted using the Aniansson-Wall theory agrees well with the simulated data, particularly at short times. At long times, deviations are observed which may be ascribed to errors in estimating the dissociation rate and number density of aggregates in the all important micelle-depleted zone.

The micellar dissociation constant was calculated from independent tagging simulations. Initially all surfactants in the micellar phase were tagged. If a surfactant left the micellar phase, the tag would be removed. An exit rate constant, which can be related to the micelle dissociation constant, was then determined by monitoring the number of tagged surfactants as a function of time. The exit kinetics proved to be a first order process. The amphiphile exit rate constant was calculated at different temperatures from which an activation energy associated with the removal of a surfactant chain from a micelle was found to be approximately 13 kT. The activation energy was found to be independent of the frictional coefficient, in contrast to the pre-exponential factor. The diffusivities of free and associated surfactants were evaluated to explain the observed dependency on the friction coefficient. The Helmholtz free energy profile associated with the extraction of a

surfactant chain from a micelle was determined. A typical micelle, aggregation number 38, was taken from an equilibrated system (reduced temperature, T_r=0.50) and used as an initial configuration for small scale NVT simulations, at the same total surfactant concentration ([S]=0.12). The micelle was in dynamic equilibrium and was observed to lose and gain monomers throughout the simulation, maintaining an average aggregation number of 36. A surfactant chain associated with the micelle was chosen at random and the first hydrophobic bead was constrained to lie a prescribed distance from the center of mass of the micelle. The surfactant molecule was perturbed, and the free energy associated with the perturbation was calculated. This process was repeated for a range of separation distances to yield a free energy profile. A free energy barrier height of 5 kT was obtained.

A potential of mean force (PMF) was incorporated into SD simulations of short linear chains (length $N = 4 - 16$) to account for solvent structure. The effect of solvent quality on the conformation of these chains (radius of gyration, mean end-to-end distance) was investigated using SD simulations and then compared to full Molecular Dynamics (MD) simulations which account for the solvent contributions exactly. The results obtained from MD and SD-PMF were statistically indistinguishable for a few simple test cases. Multiple chain systems were also investigated in non-associating and associating conditions. The structure and size distributions of the formed aggregates (pre-micelles) were indistinguishable from MD simulations over the range of concentration, temperature and chain structures investigated. The SD simulations are far more efficient since they do not take into account the solvent effects explicitly but attempt to incorporate their effect through the PMF and a stochastic noise term. The limitations of this approach are also addressed.

In part II of the thesis a normal mode stability analysis is employed to explain the presence of electrical oscillations across, and large scale motion of the interface between an aqueous solution of cetyltrimethylammonium bromide and a nitrobenzene solution containing picric acid. A two phase system (α,β) in which a solute $\mathcal{A}$ (in phase α) diffuses to the interface where it reacts with solute $\mathcal{B}$ (from phase β) to form product $\mathcal{P}$ is considered. Kinetics of the surface reaction are assumed to be infinitely fast. The stability of the system was examined with respect to small perturbations in the spirit of normal mode stability analysis. Both oscillatory and stationary regimes were identified. For the simplified case in which component $\mathcal{A}$ is insoluble in phase β and components $\mathcal{B}$ and $\mathcal{P}$ are insoluble in phase α, the presence of three diffusing components considerably modifies the stability criteria relative to those for the diffusion of a single component across the interface. Over a narrow concentration range, an oscillatory instability with a period of order one second is predicted. This compares well with observed experimental results.

Thesis Supervisors: T. Alan Hatton
Ralph Landau Professor of Chemical Engineering Practice

Kenneth A. Smith
Edwin R. Gilliland Professor of Chemical Engineering

Acknowledgments

Thanks to my thesis advisors, Alan Hatton and Ken Smith. Not only did they provide an open ended project, but they waited patiently as I tried many approaches to tackle the posed problem. My foray into parallel computing, German, Statistical Mechanics etc. were all encouraged. The research environment was always friendly and supportive. Thanks to Alan for creating such diversions as Pratice School.

A special thanks must go to Talid Sinno who initially spiked my interest in atomistic simulations and was always willing to listen to my ideas and concerns. Many a late night were spent parallelizing and many an hour running, wine tasting and skiing.

To the Practice School crowd, Dave, Matt and Chris. Thanks for the support and help that you provided. The many activities provided a welcome relief from work and enriched my stay in the USA. I could always count on you.

My research group and office members varied constantly and are to many to name individually, but they all contributed to my MIT experience. A special thanks must go to Isabella who kept my cup of coffee overflowing and introduced me to neutrons and the Russian philosophy. The visitors to the group, Kristina, Joachim, Luis, Andrea, Arijit and Arnold provided an international flavor to the group and many entertaining discussions. Carol beat me in every morning and provided never ending logistics help and despite great adversity remained cheerful.

To my friends and supporters at AECI Limited in South Africa, especially at Ammonia 4, thanks for allowing a young EIT to persue studies abroad, knowning the risk that I would not return.

I must acknowledge that without my MIT experience I would never have met my lovely wife Antonia. Patiently she waited while I worked at my research, tolerating late nights, afternoon runs and me spending her hard earned money. After knowing each other for only a few months, she courageously decided to stay in the States so that I could continue my studies. Her support, advice and excellent cooking kept me going. Finally, I must acknowledge my extended parents, whose love, support and guidance enabled me to persue my dreams.

Contents

List of Figures

List of Tables

Part I

Simulation of Surfactant Self-Assembly

Chapter 1

Introduction

Amphiphilic molecules, i.e. molecules with both hydrophilic and hydrophobic components, have the ability to associate cooperatively to form aggregates in solution. The aggregation of surfactants in solution to form micelles and other structured microphases was suggested as far back as 1913 by McBain [1] who coined the term micelle and to Hartley's description of a spherical micelle with a water free core in 1936 [2]. These supermolecular aggregates influence the macroscopic properties of the solution, for example the ability to solubilize hydrophobic components; and hence have long been of interest to researchers and practitioners alike. Microemulsions may be defined as being transparent, homogeneous mixtures of water and oil which are stabilized by surfactants. Microemulsions are thermodynamically stable and exhibit a rich phase behaviour [3], including but not limited to micelles, vesicles, lamellar, and bicontinuous structures. Typical length scales are from a few nanometers to tenths of microns. Applications in industry include detergency [4], biotechnology (protein separation [5, 6], drug delivery [7]), enhanced oil recovery [8], cosmetics [4], and novel reaction environments [9, 10, 11]. Extensive reviews of microemulsions exist, including those of Wennerström and Lindman [12], Kresheck [13] and Chevalier and Zemb [14], to which the reader is referred.

Micelles form an interesting subset of microemulsions. Phase separation occurs at a microscopic length scale but the system still comprises a single homogeneous phase on a macroscopic scale. The disparity of length scales in these systems makes them particularly difficult to study. The solvent and amphiphilic molecules have dimensions in the Angstrom range, but aggregates may vary from a few nanometers (spherical micelles [14]) to hundreds

of nanometers (vesicles [15]). Concomitant with the range of length scales are the relaxation times related to both the formation and evolution of these structures. Typically, micelles form in less than a millisecond [13], but vesicles have been known to evolve over months [15]. Important properties of micellar systems include critical micelle concentrations, average size and size distributions of the micelles, solubilization efficiency, and the dynamics of aggregate formation and rearrangement. Of particular interest are the formation of micelles, the fusion or fission of interfaces, and the exchange of material between micelles. Currently there is a lack of understanding at the fundamental level of such dynamic processes in microemulsions. Dynamic effects are particularly important in the use of micelles (normal or reversed) as compartmentalised reaction environments or their use as *in vivo* drug dispensers.

The complexity of the problem is evident when we consider that the evolution of a microemulsion to its equilibrium state is a dynamic process which is further complicated by the formation of mesophases. Dynamic equilibrium phenomena such as droplet collisions are no less trivial. The structure of surfactant molecules, hydrodynamics, steric hindrance, and electrostatic interactions add to the problem complexity. Theoretical efforts to understand and predict surfactant solution properties rely on both phenomenological thermodynamic analyses and atomistic simulations. Thermodynamic theories are unable to deal with dynamic aspects. Microscopic models, such as molecular dynamics (MD) and Monte Carlo (MC) simulation schemes, are unable to deal efficiently with such large systems while continuum models lack essential microscopic details. In order to simulate micelle structures, large systems (order 10^5 particles) and long periods (order 10 - 100 microseconds) are required. The problem is intractable using current computational methods. Hence there is a need for a theoretical approach which bridges this gap between microscopic and continuum models. Our philosophy will be to study simple systems which contain only the essential physics of the problem. Although these systems may lack some of the structural details, they are computationally less intensive and hence tractable. In this thesis we explore the potential for atomistic Stochastic Dynamics (SD) simulation techniques to predict micelle equilibrium properties and compare these results to existing thermodynamic theories. The dynamics of micelle formation are also investigated and the ability to incorporate solvent structure via a potential of mean force is evaluated.

1.1 Review of Modelling Approaches

1.1.1 Thermodynamic Theories

The prediction of equilibrium microstructures from molecular architecture and intermolecular interactions has received a great deal of attention. Simple space-filling packing arguments, together with an estimated optimal surface area per surfactant, allow one to predict micellar and vesicular structures in dilute surfactant solutions [16, 17]. Thermodynamic theories can yield important information about micellization, phase behaviour, critical micelle concentration (cmc), and droplet size distribution [16, 17]. This approach assumes the microstructure *a priori*. One calculates the free energy for different assumed microstructures, the microstructure with the lowest free energy being taken to be most stable and most likely to occur. A major drawback is that complicated or as yet unimagined microstructures are ignored. For single surfactant systems Tanford [18] developed a phenomenological theory of micellization while Nagarajan and Ruckenstein [19] used a molecular approach. Puvvada and Blankschtein [20] provide a molecular-thermodynamic approach that takes into account the nature of the surfactant molecule and successfully predicts a variety of micellar thermodynamic properties [21]. This molecular-thermodynamic approach has also been extended to mixed vesicles [22] and been used to evaluate the effect of surfactant tail-length asymmetry on vesicle formation [23].

Simple phenomenological models to describe the phase equilibria and structural properties of microemulsions were developed by Talmon and Prager [24, 25] and later refined by Andelman *et al.* [26] and Davis *et al.* [3]. Space is divided into cells (initially polyhedrals), each of which is filled either with oil or water. It is assumed that surfactants form incompressible monolayers at cell faces separating oil and water regions. The free energy is calculated taking into account curvature effects, and a phase diagram constructed by suitable minimization. These techniques represent an interfacial approach and are ideally suited to probe long range order (continuum length scales), e.g. the phases that form in microemulsions. In contrast, a molecular/microscopic approach would require tens of thousands of molecules to sample similar length scales.

A common shortcoming of these thermodynamic theories is that they are unable to probe the dynamics of microemulsions or to present transition states or pathways by which these systems evolve. The thermodynamic theories have, however, advanced to the stage

where they have predictive capabilities.

An alternative approach to molecular theories is the use of atomistic/molecular level simulations and this work falls predominately into two categories; lattice models and molecular dynamics (MD). Throughout the subsequent discussion a consistent notation that may not correspond to that used by the orginal authors will be employed in order to facilitate comparison between different works in the literature. The hydrophilic or solvophilic components will be designated by A and the hydrophobic or solvophobic elements as B.

1.1.2 Lattice Models

Lattice models have been employed extensively over the last three decades to probe surfactant self-assembly. Initial work in this area involved lattice systems that could be recast in the framework of Ising and lattice gas models whose solutions could be determined analytically. Recently more complicated lattice systems that require solution via Monte Carlo (MC) simulations have been used.

Wheeler and Widom [27] modelled a three component system of difunctional molecules of type AA, AB and BB on square and cubic lattices. The molecules are confined to the bonds of the lattice and atoms may meet at lattice sites (nodes). The association of an A and B atom at the same site is disallowed. As a result, every lattice site is unambiguously identified as an A site or a B site, allowing for the problem to be recast in the form of the analytically tractable Ising-$\frac{1}{2}$ model. The phase behaviour of the three component system was evaluated and showed a characteristic plait point at high surfactant concentrations. Above the plait point, a single, homogeneous phase is evident. Surface excess concentrations and molecule orientations at the interface were calculated by analogy to the temperature dependence of the surface tension in a single component lattice gas system [28]. Finally an interface bending energy was incorporated by including next-nearest neighbour interactions between the AB molecules [29]. Three phase regions were identified. With the constraint that the amphiphile, AB, be the length of the lattice cell, a coherence length was automatically included in this model from the onset. Wheeler and Stockfish [30] used two interpenetrating lattices, one for the amphiphiles and the other for the solvents. Each cell corresponded to an oil molecule or a water molecule, and hence no coherence length was included from the outset. In addition, interaction energies between all components were allowed for.

Larson [31] performed MC simulations of simplified amphiphile-oil-water systems in

2-D. The oil- (B) and water- (A) like molecules occupied individual sites, while the amphiphile was represented as a chain of sites (A_iB_j). New configurations were generated by chain reptation, chain twisting and interchange of the solvent sites (for detailed discussion of MC see [32, 33]). This system is characterised by a single energy parameter $\omega = [\epsilon_{AB} - \frac{1}{2}(\epsilon_{AA} + \epsilon_{BB})]/kT$, where ϵ_{AA}, ϵ_{BB}, ϵ_{AB} are the interaction energies associated with hydrophilic-hydrophilic, lyophilic-lyophilic and hydrophilic-lyophilic contacts respectively, and T is the temperature. Phase diagrams were presented and compared to predictions of the zeroth and first order (quasichemical) lattice theories [34]. Interestingly, multiphase systems, as identified by a constant free energy surface, were not evident from viewing the system configurations [31]. The interfaces are distorted by thermally driven fluctuations (capillary waves). This problem is compounded by the low interfacial tensions (hence larger distortions) and 2-D simulations (larger box sizes lead to only a slow decrease in disturbance size relative to the box size). Head-group hydration was found to play an important role in the solubilizing ability of the amphiphile, since, if head-head interactions are equivalent to head-solvent interactions it was found that the amphiphiles clumped at some locations of the oil-water interface, i.e. the head groups were not evenly distributed on the micelle surface. The work was later extended to 3-D [35] (lattice coordination number = 26) and composition dependent transitions in microstructure from lamellar to cylindrical to spherical were observed. The influence of tail length, concentration and temperature on ordering transitions, including the formation of micelles, was also investigated [36]. The amphiphile A_2B_2 did not form micelles at the inverse temperature $\omega = 0.1538$. A_3B_3 and A_4B_4 formed micelles, whereas A_1B_3 precipitated out of the water phase. Presented are size distributions, average sizes and polydispersity of micelles formed for a range of surfactants at different concentrations. Subsequent work focused exclusively on the structure of ordered amphiphilic phases [37, 38]. A simplification of Larson's model (AN_4B where N represents a neutral block, lattice coordination number 6) was used to demonstrate the existence of a three phase coexistence region and to obtain a stable (time invariant) peak in the cluster size distribution [39]. The phase behavior was inferred from the time and system size dependence of the mean aggregation number, i.e. if the aggregate size continues to grow with time the authors conclude that the system phase separates.

Small scale (only 20 chains) lattice simulations of large diblock copolymers ($A_{10}B_{10}$) were used to investigate the effect of the interaction strength on the size of the aggregates

formed [40]. At low interaction energies, small aggregates are observed, however, a single micelle results when the interaction energy is increased further. The system is trapped in a metastable state since surfactants in the micelle are unable to leave the micelle over the duration of the simulation. As the length of the soluble block is increased, so smaller aggregates are formed due to steric interaction between the head-groups. The segmental distribution function for a single micelle comprised of such diblock copolymers (equivalent to $\epsilon_{BB} = -1, \epsilon_{AA} = \epsilon_{AB} = 0,\ \omega = 0.5$) was subsequently studied [41]. The system size was limited to twenty chains which formed a single micelle and hence the structure cannot necessarily be viewed as an equilibrium structure. An internal core comprised of the insoluble blocks was surrounded by a corona region. Unlike current analytical models, the interface separating the core and corona regions was not sharp. These results are, however, compatible with self consistent mean field theory predictions [42, 43].

Wang *et al.* [44] performed Monte Carlo simulations of the self-assembly of diblock copolymers ($A_{N_A}B_{N_B}$) into micelles on a cubic lattice. An equal energy penalty was assigned to AB and BS (S=solvent) interactions ($\epsilon_{BS} = 0.45, \omega = 0.45$). The critical micelle concentration, cmc, (based on number fraction of free surfactants or on volume fraction of the B block V_B) was found to be only weakly dependent on N_A (soluble block length) provided that N_A was not too different from N_B. The dependence of the cmc on the interaction $\epsilon_{BS}N_B$ was found to follow an exponential behavior as predicted by Leibler's theory [45]. Issues of equilibration are discussed, including existence of two timescales; the faster associated with equilibration of free chains and the slower the equilibration of the average aggregate size. A radial distribution function through a micelle of size 16 was calculated. There is some concern as to whether the system was at equilibrium in this study, since the free surfactant concentration had levelled off but the average aggregation number was still showing significant variation. The free surfactant concentration was shown to decline at high surfactant volume fractions. Part of this drop off may be explained by the increase of the volume of micelle phase (hence a reduction in the volume of the solvent phase), which was recognized subsequently [46]. Whether this explains all of the drop-off must still be established.

Wang *et al.* [47] also investigated the effect of the pair interaction parameters on the cmc of diblock copolymers. By tripling the size of the soluble block, the cmc doubles if $\epsilon_{AB} = 0$, but produces no effect if $\epsilon_{AB} = 0.7$ at constant $\epsilon_{BS} = 0.45$ (i.e. by changing

the repulsive interaction between A and B blocks). The authors ascribe this to an entropy effect relating to a reduction in the flexibility of the soluble blocks. As ϵ_{AB} is increased the excluded volume entropic effect is less significant due to repulsion between AB blocks. ϵ_{AB} in the range 0.0 - 0.7 has no effect on the cmc for N_A/N_B=3, but doubles the cmc for N_A/N_B=1. Not surprisingly, the effect of ϵ_{AB} is much smaller (order 3) than the effect of ϵ_{BS} (order 20 variation). The effect of varying ϵ_{AS} in range -0.5 - 0.0, for $\epsilon_{BS} = \epsilon_{AB} = 0.45$ was insignificant. As diblock copolymer concentration increases (volume fraction range 0.45-0.85) different aggregate morphologies have been identified [48], including spherical, cylindrical, monocontinuous catenoid-lamellar and lamellar morphologies. The transition concentrations were identified visually and by monitoring the anisotropy of the translation diffusion coefficient. The effect of chain stiffness was investigated [46] by assigning an energy penalty ω_B whenever two successive bonds form an angle of 90°. As the insoluble block became stiffer (ω_B increases) the cmc decreased and the weight average aggregate size increased. The stiffer the chain, the greater the number of contacts with the solvent and hence the greater the enthalpic gain if it is incorporated into a micelle.

More recently Haliloğlu and Mattice [49] developed autocorrelation functions to look into the exchange of chains between micelles and the free surfactant pool as a function of concentration. Unfortunately, due to the the size of the amphiphiles considered ($A_{10}B_{10}$), the dynamics are excruciatingly slow and hence the correlation functions do not decay to zero.

Symmetric triblock copolymers ($B_{N_B}A_{N_A}B_{N_B}$), where the solvent interacts preferentially with the beads in the internal block, have also been simulated [50] and found to form micelles in the strong segregation limit. To my knowledge, no MC simulations have been performed for triblock copolymers with soluble outer blocks, which would correspond to the commercially available Pluronic®(BASF) and Synperonic®(ICI) surfactants. However, the self consistent mean field theory of Scheutjens and Fleer [51] was extended to triblock copolymers by Hurter *et al.* [42] and Linse [43].

A brief mention should be made of the work of Bernardes *et al.* [52], in which the self-assembly of amphiphiles is modelled on a 2-D lattice, since they attempt to use the results from simple mass action models to fit their data.

Lattice MC simulations of the ternary system (oil-water-amphiphile) were used to determine the phase diagram of symmetric and asymmetric amphiphiles and compared to the

quasichemical theory [53]. The removal and regrowth of whole chains by configurational bias methods is used to assist equilibration and sampling. A cubic lattice with coordination number 26 was used. Runs were performed at $kT/\epsilon = 6.5$ which is well below the critical point for the oil/water mixture (11.8) and is the same temperature used in Larson's work. Of particular interest is that the surfactant A_2B_2 showed no macroscopic phase separations at zero oil concentration and in the low amphiphile concentration region of the phase diagram. Problems were experienced in using the Gibbs ensemble technique for determining the free energy, hence the authors opted for NVT ensemble with interfaces. Considerable density fluctuations were still observed even far from the interface and averaged over the entire run. It is interesting to note that, for the asymmetric surfactant A_1B_3, a two phase region exists even in the absence of the oil phase (at this temperature). It thus becomes clear that before simulating micelle formation we need to ensure that we are indeed in a single phase region (difficult for A_1B_3). This can be done by calculating the free energy by thermodynamic integration and looking for regions of constant chemical potential which would be indicative of phase separation (as done by Larson [31]). Near quantitative agreement is found between the quasichemical theory and the simulations except where either phase self-assembles.

Desplat and Care [54] recently modeled a short surfactant chain (one head bead and three tail beads, AB_3) and used the resulting equilibrium micelle size distribution to back out the excess chemical potential $(\mu_s^o - \mu_1^o)$ which was then compared to existing analytical expressions [55]. The effects of temperature, surfactant concentration and head - solvent interactions were thoroughly investigated. Earlier work focussed on characterising the phase diagram for this system [56] and obtaining a cluster size distribution for a simplified 2-D amphiphile system [57].

1.1.3 Molecular Dynamics

Molecular Dynamics simulations of surfactant aggregation fall into two categories. Firstly, the surfactant models used may involve complicated all atom potentials in an attempt to represent real surfactants and solvents. Since this approach is computationally intensive, the micelle structures have to be preassembled (i.e. the structure must be selected *a priori*) and only a single aggregate can be simulated for short periods (typically less than 0.1 ns). Examples of this work include : reverse micelles [58], n-decyltrimethylammonium chloride

micelles in water [59], sodium octanoate micelles [60]. This method is unsuitable for probing the dynamics of self-assembly and relies heavily on the choice of initial structure.

The second approach uses simplified surfactants (only having the essential characteristics of amphiphiles) but allows the surfactants to self-assemble into structures they prefer. At best qualitative behaviour may be obtained from such model systems. Work in this area is discussed in greater detail in the subsequent paragraphs.

Gunn and Dawson [61] made an attempt to bridge the gap between primitive lattice models and highly complex all atom descriptions of amphiphilic systems. Ellipsoids were used for the lipid molecules and spheres for the water molecules. Modified Lennard Jones 6-12 potentials were used where ϵ and σ are not only a function of separation distance, but also of orientation. A constant temperature molecular dynamics study (10000 water molecules, 500 lipids), in which the divergence of the pressure tensor was constrained to zero, was performed. Preliminary results are presented, in particular the structure of the lamellar phase over the temperature range for which it is stable.

Smit [62] used molecular dynamics to model a simple liquid-liquid amphiphile system. The model comprised two liquid layers of 256 particles of A and 256 particles of B. The particles interact via a shifted Lennard Jones 6-12 potential and the repulsive interactions between A and B are obtained by truncating the potential at $2^{\frac{1}{6}}\sigma$. Simple dumbbell amphiphiles (A-B connected by a harmonic spring) are generated and their effect on surface tensions is evaluated. Density profiles are also obtained across the interface. The interface is found to broaden as the concentration of the amphiphiles is increased.

The first MD simulation to show the spontaneous formation of micelles was performed by Smit *et al.* [63]. A system comprising some 32 000 particles was simulated using a parallel molecular dynamics algorithm and run on a system of 100 transputers. Each time step took around 2.8 seconds. Oil and water molecules were modelled using Lennard-Jones interactions (cut-off distance 2.5σ). The oil-water interactions were obtained by truncating the Lennard-Jones potential at $2^{\frac{1}{6}}\sigma$, hence they were purely repulsive. The surfactants were comprised of five oil-like beads and two water-like beads (A_2B_5) strung together using harmonic potentials. A surfactant monolayer at the interface and micelles in the water phase were found to develop spontaneously. A depletion zone, containing only water molecules, separates the monolayer from the micelles (solvation effect). Oscillations in micelle density were observed. Surface tensions were calculated for various surfactant concentrations by

integrating the difference of the normal and tangential components of pressure tensor across the interface. The probability and density distributions of surfactants in a micelle was also obtained. No micelles were observed for simple dumbbell surfactants (A_1B_1). Subsequently Smit *et al.* [64] were able to obtain a complete micellar size distribution and observe dynamical processes such as the entering of single surfactants into micelles, the fusion of micelles and the slow breakdown of micelles for the branched surfactant A_3AB_5. A comprehensive summary of this work is provided by Esselink *et al.* [65]. These simulations, which require weeks of cpu time, provide useful snapshots of the system but are typically not long enough to obtain statistically significant information on the structure of the system.

Molecular dynamics simulations were performed on a simple water/oil/surfactant model to mimic the solubilization of non-polar molecules into aqueous solutions. Three mechanisms were identified [66] for the uptake of oil molecules into micelles : (i) dissolution of oil molecules into the solvent phase (finite solubility) before being captured by micelles; (ii) exchange of oil molecules between the oil droplet and the micelles during soft collision; (iii) collective desorption of surfactants and oil molecules from the oil droplet surface. Mechanism (i) was dominant for small oil molecules.

The morphologies of aggregates formed by gemini (hydrophilic head groups connected with a spacer chain) surfactants was investigated by Karaborni *et al.* [67] using large scale parallel MD. Aggregate structure was found to vary drastically with spacer length. Tree-like micelles also formed (aggregation number around 200).

Rector *et al.* [68] performed NPT MD simulations of model surfactant - solvent systems. Surfactant molecules were modelled as heteronuclear diatoms (connected by non-harmonic springs of finite extension). In addition to using the cut-off distance to control the type of interaction, the size of the tail (σ_t) was taken to be a third of the head group size (σ_h). Chemical potentials (of surfactant and solvent) were obtained as a function of concentration using the Widom test particle method.

Recent NPT MD simulations probing the effect of chain length [69] and the presence of solute on micelle formation [70] are, unfortunately, restricted to small systems and short times. Equilibrium properties are, therefore, not accessible. The results represent a snapshot in time (and not necessarily even an equilibrium snapshot). Unlike the work of Smit *et al.*, the head-head interactions are different from the solvent-solvent and head-solvent interactions. The simulation of the spontaneous formation of vesicles has also been reported

[71], but appears to be an intermediate structure caused by the aggregation of micelle-like aggregates (system phase separates). The number and size of vesicles formed was found to be dependent on system size.

Although considerable progress has been made in simulating self-assembling systems, equilibrium properties are still beyond the scope of these techniques even with current computational capabilities. Very little effort has been made to demonstrate that structures that are observed are in fact equilibrium structures and that the simulation time is sufficient to sample equilibrium properties.

1.1.4 Hybrid Models

Langevin dynamics has been used to model phase separation in binary immiscible fluids and more recently in surfactant systems [72, 73]. Due to the continuum nature of these equations and the ability to take into account microscopic fluctuations, it is possible to sample a greater time range than that accessible in molecular level simulations. The hybrid model of Kawakatsu and Kawasaki [74] may bridge the gap between continuum and microscopic models for these systems.

A review of different modelling approaches is given by Kawakatsu *et al.* [75], with particular emphasis on continuum and hybrid models. In continuum models a coarse grained free energy expression is obtained from a power series expansion in the continuous field variables (local surfactant density and relative concentration of the binary mixture). From symmetry arguments, relevant terms in the power series expansion may be retained. This approach is phenomenological but has been used extensively to investigate critical phenomena. Alternatively, a macroscopic model may be obtained by coarse graining the microscopic degrees of freedom, using mean field approximations or the renormalization group method to yield a free energy expression. The equations of motion for the conserved variables (e.g. order parameter) take the form of the continuity equation while surfactant position and orientation evolve from dissipative equations. Using this method, the early and late stages of phase separation of a binary mixture including surfactants has been investigated in 2-D.

1.2 Conclusion

Thermodynamic theories are in a position to provide quantitative information about surfactant systems and are being used successfully to predict cmc's, phase behaviour, micelle structures, the formation of vesicles and other thermodynamic properties. Unfortunately these techniques are unable to probe the dynamics of self-assembly or to identify novel aggregate structures that might form. Alternative methods, such as microscopic simulations (MD, MC or hybrid approaches) are unable to give quantitative information, since the computational overhead associated with incorporating realistic interaction potentials is beyond current computational means. Simplified amphiphiles and solvents are therefore simulated. Clearly only qualitative information is available from such simplified systems. Unfortunately, the difficulty in successfully sampling the configuration phase space, even for such simplified systems, has led to much data which are clearly non-equilibrium or poorly sampled.

In the next chapter we will address the theoretical basis for performing stochastic dynamic simulation, namely the generalised Langevin equation (GLE). In self-assembling surfactant systems, the time scales associated with surfactant motion and the formation of aggregates are vastly different from the time scales associated with solvent motion and therefore the memory kernel in the GLE may be assumed to be delta correlated in time. This provides the basis for approximating the solvent effects using stochastic noise terms and a solvent modified potential and leads to a considerable reduction in the system size to be simulated.

Bibliography

[1] J. W. McBain, Trans. Faraday Soc. **9,** 99 (1913).

[2] G. S. Hartley, *Aqueous Solutions of Paraffin Chain Salts*, (Hermann, Paris, 1936).

[3] H. T. Davis, J. F. Bodet, L. E. Scriven, and W. G. Miller, In *Springer Proceedings pf Physics Vol 21 : Physics of Amphiphilic Layers*, edited by J. Meunier, D. Langevin, and N. Boccara, (Springer-Verlag, New York, 1987).

[4] D. R. Karsa, *Industrial Applications of Surfactants*, (Whitstable Litho Ltd., Whitstable, Kent, UK, 1987).

[5] K. E. Göklen and T. A. Hatton, Separation Science and Technology **22,** 831 (1987).

[6] P. D. I. Fletcher and D. Parrott, J. Chem. Soc., Faraday Trans. 1 **84,** 1131 (1988).

[7] A. V. Kabanov, E. V. Batrakova, N. S. Melik-Nubarov, N. A. Fedosev, T. Yu. Dorodnich, V. Yu. Alakhov, V. P. Chekhonin, I. R. Nazarova, and V. A. Kabanov, J. Controlled Release **22,** 141 (1992).

[8] V. K. Bansal and D. O. Shah, In *Microemulsions*, edited by L. M. Prince, (Academic Press, New York, 1977).

[9] P. D. I. Fletcher and D. Parrott, J. Chem. Soc., Faraday Trans. 1 **80,** 2417 (1984).

[10] P. L. Luisi, Angew. Chem. **24,** 439 (1985).

[11] M. P. Peleni, J. Phys. Chem. **97,** 6961 (1993).

[12] H. Wennerström and B. Lindman, Physics Reports **52,** 1 (1979).

[13] G. C. Kresheck, In *Water, A Comprehensive Treatise, Vol 4. Aqueous Solutions of Amphiphiles ans Macromolecules*, edited by F. Franks, (Plenum Press, New York, 1975), p. 95.

[14] Y. Chevalier and T. Zemb, Rep. Prog. Phys. **53,** 279 (1990).

[15] M. T Yatcilla, K. L. Herrington, L. L. Brasher, E. W. Kaler, S. Chiruvolu, and J. A. Zasadzinski, J. Phys. Chem. **100,** 5874 (1996).

[16] R. J. Hunter, *Foundations of Colloid Science Vol. 1*, (Oxford Science Publications, 1991).

[17] J. Israelachvili, *Intermolecular and Surface Forces*, (Academic Press, London, 1991).

[18] C. Tanford, *The Hydrophobic Effect*, (Wiley, New York, 1980).

[19] R. Nagarajan and E. J. Ruckenstein, J. Colloid and Interface Sci. **60,** 221 (1977).

[20] S. Puvvada and D. Blankschtein, J. Phys. Chem. **96,** 5567 (1992).

[21] N. Zoeller and D. Blankschtein, Ind. & Eng. Chem. Res. **34,** 4160 (1995).

[22] P. K. Yuet and D. Blankschtein, Langmuir **12,** 3802 (1996).

[23] P. K. Yuet and D. Blankschtein, Langmuir **12,** 3819 (1996).

[24] Y. Talmon and S. Prager, J. Chem. Phys. **69,** 2984 (1978).

[25] Y. Talmon and S. Prager, J. Chem. Phys. **69,** 1535 (1982).

[26] D. Adelman, M. E Cates, D. Roux, and S. A Safran, J. Chem. Phys. **87,** 7229 (1987).

[27] J. C. Wheeler and B. Widom, J. Am. Chem. Soc. **90,** 3064 (1968).

[28] B. Widom, J. Phys. Chem. **88,** 6508 (1984).

[29] B. Widom, J. Chem. Phys. **84,** 6943 (1986).

[30] J. C. Wheeler and T. P. Stockfish, In *Springer Proceedings pf Physics Vol 21 : Physics of Amphiphilic Layers*, edited by J. Meunier, D. Langevin, and N. Boccara, (Springer-Verlag, New York, 1987).

[31] R. G. Larson, L.E. Scriven, and T. E. Davis, J. Chem. Phys. **83,** pages 2411–2420 (1985).

[32] M. P. Allen and D. J. Tildesley, *Computer Simulations of Liquids*, (Oxford Science Publications, Oxford Press, 1992).

[33] K. Binder, *Monte Carlo and Molecular Dynamics Simulations in Polymer Science*, (Oxford University Press, New York, 1995).

[34] H. Tompa, *Polymer Solutions*, (Academic Press, New York, 1956).

[35] R. G. Larson, J. Chem. Phys. **89,** 1642 (1988).

[36] R. G. Larson, J. Chem. Phys. **96,** 7904 (1992).

[37] R. G. Larson, Macromolecules **27,** pages 4198–4203 (1994).

[38] R. G. Larson, Chemical Engineering Science **49,** pages 2833–2850 (1994).

[39] D. Stauffer, N. Jan, Y. He, R. B. Pandey, D. G. Marangoni, and T. Smith-Palmer, J. Chem. Phys. **100,** 6934 (1994).

[40] K. Rodrigues and W. L. Mattice, J. Chem. Phys. **94,** pages 761–766 (1991).

[41] K. Rodrigues and W. L. Mattice, J. Chem. Phys. **95,** pages 5341–5346 (1991).

[42] P. N. Hurter, J. M. H. M. Scheutjens, and T. A. Hatton, Macromolecules **26,** 5592 (1993).

[43] P. Linse, Macromolecules **26,** 4437 (1993).

[44] Y. Wang, W. L. Mattice, and D. H. Napper, Langmuir **9,** 66 (1993).

[45] L. Leibler, H. Orland, and J. C. Wheeler, J. Chem. Phys. **79,** 3550 (1983).

[46] P. Adriani, Y. Wang, and W. L. Mattice, J. Chem. Phys. **100,** 7718 (1994).

[47] Y. Wang, W. L. Mattice, and D. H. Napper, ACS Symposium Series **532,** pages 45–52 (1993).

[48] M. B. Ko and W. L. Mattice, Macromolecules **28,** pages 6871–6877 (1995).

[49] T. Haliloğlu and W. L. Mattice, Chem. Eng. Sci. **49,** 2851 (1994).

[50] Y. Wang, W. L. Mattice, and D. H. Napper, Macromolecules **25,** 4073 (1992).

[51] J. M. H. M. Scheutjens and G. J. Fleer, J. Phys. Chem. **83,** 1619 (1979).

[52] A. T. Bernardes, V. B. Henriques, and P. M. Bisch, J. Chem. Phys. **101,** pages 645–650 (1994).

[53] A. D. Mackie, K. Onur, and A. Z. Panagiotopolous, J. Chem. Phys. **104,** 3718 (1996).

[54] J.-C. Desplat and C. M. Care, Molec. Phys. **87,** 441 (1996).

[55] R. E. Goldstein, J. Chem. Phys. **84,** 3367 (1986).

[56] D. Brindle and C. M. Care, J. Chem. Soc. Faraday Trans. **88,** 2163 (1992).

[57] C. M. Care, J. Chem. Soc. Faraday Trans. 1 **83,** 2905 (1987).

[58] D. Brown and J. H. R. Clarke, J. Phys. Chem **92,** 2881 (1988).

[59] J. Böcker, J. Brickmann, and P. Bopp, J. Phys. Chem. **98,** 712 (1994).

[60] J. C. Shelly, M. Sprik, and M. Klein, Langmuir **9,** 916 (1993).

[61] J. R. Gunn and K. A. Dawson, J. Chem. Phys. **91,** 6393 (1989).

[62] B. Smit, Phys. Rev. A **37,** pages 3431–3433 (1988).

[63] B. Smit, P. A. J. Hilbers, K. Esselink, L. A. M. Rupert, and N. M. van Os, J. Phys. Chem. **95,** 6361 (1991).

[64] B. Smit, K. Esselink, P. A. J. Hilbers, N. M. van Os, L. A. M. Rupert, and I. Szleifer, Langmuir **9,** 9 (1993).

[65] K. Esselink, P. A. J. Hilbers, N. M. van Os, and S. Karaborni, Colloids and Surfaces A : Physicochemical and Engineering Aspects **91,** pages 155–167 (1994).

[66] S. Karaborni, N. M. van Os, K. Esselink, and P. A. J. Hilbers, Langmuir **9,** 1175 (1993).

[67] S. Karaborni, K. Esselink, P. A. J. Hilbers, B. Smit, J. Karthauser, N. M. van Os, and R. Zana, Science **266,** 254 (1994).

[68] D. R. Rector, F. van Swol, and J. R. Henderson, Molec. Phys. **82,** 1009 (1994).

[69] B. J. Palmer and J. Liu, Langmuir **12,** 746 (1996).

[70] B. J. Palmer and J. Liu, Langmuir **12,** 6015 (1996).

[71] A. T. Bernardes, Langmuir **12,** 5763 (1996).

[72] M. Laradji, H. Guo, M. Grant, and M. J. Zuckermann, J. Phys. A: Math. Gen. **24,** L629 (1991).

[73] M. Laradji, H. Guo, M. Grant, and M. J. Zuckermann, J. Phys. : Condensed Matter **4,** 6715 (1992).

[74] T. Kawakatsu and K. Kawasaki, Physica A **169,** 690 (1990).

[75] T. Kawakatsu, K. Kawasaki, M. Furusaka, and H. Okabayashi, Journal of Physics. Condensed matter **6,** 6385 (1994).

Chapter 2

Stochastic Dynamics

2.1 Background Theory

In many physical systems we may have time scales of vastly different order. A typical example is the motion of a large molecule (e.g. conformations of a protein molecule) in a solvent medium. The different order timescales pose a serious problem to conventional simulation schemes like Monte Carlo simulations or molecular dynamics. The short timesteps needed to model the solvent behaviour (the fast motion) restrict the timescales that may be sampled, thereby limiting the information that can be obtained for the slower motion. There is thus a need for **timescale separation** [1]. This is achieved by omitting the solvent molecules and incorporating their influence on the solute by a combination of random forces and frictional terms. Put succinctly, stochastic or Brownian dynamics allows for the treatment of solvent molecules statistically rather than explicitly [2].

There is a vast collection of literature dealing with the theoretical basis for eliminating rapidly varying degrees of freedom. A brief overview of the relevant work will be given, and an attempt will be made to tie the various approaches together.

2.1.1 Generalized Langevin Equation (GLE)

The basis for removing rapidly varying degrees of freedom is given by Mori [3]. He begins by considering a column matrix $\mathbf{A} = (A_1, A_2, \ldots A_N)^T$, where A_i represents a dynamical variable of interest. $\mathbf{A}$ is a subset of all the possible dynamical variables. Each of these

variables evolves via the conjugate form of the Liouville equation [4],

$$\frac{d\mathbf{A}(t)}{dt} = i\mathcal{L}\mathbf{A}(t) \tag{2.1}$$

where $\mathcal{L}$ is the Liouville operator

$$i\mathcal{L} = \sum_{j=1}^{N}[\frac{\partial H}{\partial \mathbf{p}_j}\cdot\frac{\partial}{\partial \mathbf{r}_j} - \frac{\partial H}{\partial \mathbf{r}_j}\cdot\frac{\partial}{\partial \mathbf{p}_j}] \tag{2.2}$$

and H is the system Hamiltonian. A projection operator $\mathcal{P}$ in Hilbert space is introduced which, when operating on a vector $\mathbf{G}$, yields the component of $\mathbf{G}$ along $\mathbf{A}$ ($\mathbf{A}^*$ is the complex conjugate of $\mathbf{A}$).

$$\mathcal{P}\mathbf{G} = (\mathbf{G}, \mathbf{A}^*)\cdot(\mathbf{A}, \mathbf{A}^*)^{-1}\cdot\mathbf{A} \tag{2.3}$$

In classical systems $(\mathbf{G}, \mathbf{A}^*) =< \mathbf{G}\mathbf{A}^* >$, where the angular brackets represent an ensemble average. Substantial manipulations yield the following exact generalized equation of motion for the set of dynamical variables $\mathbf{A}(t)$.

$$\frac{d\mathbf{A}(t)}{dt} - i\omega\cdot\mathbf{A}(t) + \int_0^t \varphi(t-s)\cdot\mathbf{A}(s)ds = \mathbf{f}(t) \tag{2.4}$$

where $i\omega = (\dot{\mathbf{A}}, \mathbf{A})\cdot(\mathbf{A}, \mathbf{A})^{-1}$ is a frequency matrix determining collective oscillations of $\mathbf{A}(t)$, $\varphi(t)$ is a damping function (commonly called the memory matrix or memory kernel [1]) which can be related to the damping constant of collective motion. Furthermore $\mathbf{f}(t)$, the random force, is related to $\varphi(t)$ via the relationship

$$(\mathbf{f}(t_1), \mathbf{f}(t_2)) = \varphi(t_1 - t_2)\cdot(\mathbf{A}, \mathbf{A}^*), \tag{2.5}$$

and remains orthogonal to $\mathbf{A}(0)$ for all times.

The success of this approach hinges on the ability to model $f(t)$ stochastically and hence obtain an approximate solution to Eq. 2.1. Consider the simple case where $\mathbf{A}$ is a component of the momentum of a single particle p_{ix} in a solvent bath with lower inertial mass. Since $\varphi(t)$ decays more rapidly than $< \mathbf{A}(t)\mathbf{A}(0) >=< p_{ix}(t)p_{ix}(0) >$, i.e. the bath molecules' momentum decays more rapidly than the solute particle's momentum, $\varphi(t)$ may be approximated by a delta function and the convolution integral in Eq. 2.4 can be performed directly (this corresponds to a Markovian process, independent of past history).

Eq. 2.4 then reduces to the well known equation for Brownian motion by making use of the equipartition theory that relates the temperature to the momentum.

$$\dot{p}_{ix} = -\xi p_{ix} + f(t) \tag{2.6}$$

where

$$< f(t)f(0) >= 2mk_BT\xi\delta(t) \tag{2.7}$$

ξ and m are the frictional coefficient and mass of solute respectively, k_B is the Boltzmann constant and T the temperature. These equations were derived based on independent particles and have been extended on an *ad hoc* basis to include forces, $F(t)$, between the particles,

$$\dot{p}_{ix} = -\xi p_{ix} + F(t) + f(t) \tag{2.8}$$

A statistical mechanical basis for including solute-solute and solute-solvent forces was presented by Ciccotti and Ryckaert [5] by employing Mori's technique on the variable $\mathbf{p} - (i\mathcal{L})^{-1}\mathbf{F}(t)$. The form of the GLE is unchanged, but the random force and memory kernel introduced no longer satisfy the usual fluctuation-dissipation theorem and the resulting equations are computationally intensive to implement. The random force is also no longer orthogonal to the initial momentum. An alternative approach was adopted by Bossi *et al.* [6] in which they derived the fluctuation-dissiption relation for the *ad hoc* equation

$$\dot{\mathbf{p}}(t) = -\int_0^t \varphi(t-s)\mathbf{p}(s)ds + \mathbf{f}(t) + \mathbf{F}(t) \tag{2.9}$$

and obtained

$$< (\mathbf{p}(0))^2 > \varphi(t) =< \mathbf{f}(t) \cdot \mathbf{f}(0) > +2 < \mathbf{p}(0) \cdot \mathbf{F}(0) > \delta(t) \tag{2.10}$$

The additional term $2 < \mathbf{p}(0) \cdot \mathbf{F}(0) > \delta(t)$ was obtained and has been shown to be small in a few test cases [7, 8]. The effect of this additional term is to effect the stochastic properties of the random force required to obtain the correct temperature.

The form of the memory kernel is important in systems in which the mass of the solute is comparable to that of the solvent. Strictly speaking, the inclusion of the memory kernel requires the evaluation of the convolution integral at every timestep [1, 9] (and hence the

storage of the molecule's prior history). An alternative approach was implemented by Ciccotti and Ryckaert [10] and is related to Mori's continued fraction representation for the memory kernel [11]. The GLE (Eq. 2.4) can be recast as an n_{th} order system of linear differentiation equations (each in higher and higher orders of the dynamic variable), containing the Mori coefficients K_n, which have to be truncated at some level by approximating the random force by Gaussian white noise. This follows directly from the fact that the random forces and the normalized velocity autocorrelation function (ϕ) satisfy a modified version of the Langevin equation. The Laplace transform of the velocity autocorrelation function can be expressed as a continued fraction

$$\tilde{\phi}(s) = \cfrac{K_1}{s + \cfrac{K_2}{s + \cfrac{K_3}{s + \cdots}}} \tag{2.11}$$

The coefficients, K_n, called the damping matrices, can be related to derivatives of the velocity autocorrelation function. The explicit expressions to order 5 have been derived [12], although owing to the difficulties associated with calculating higher order derivatives of the velocity autocorrelation functions they are only accessible from MD simulations at considerable computational expense [13]. Furthermore it is found that many coefficients are required to describe the short time behaviour. The net result is that this approach is seldom used. Alternatively the form of the memory function may be assumed, e.g. exponential or a finite sum of exponentials and may be fitted to the velocity autocorrelation results obtained from MD. The Mori coefficients may then be calculated from the fitted analytical expression. This technique was used by Ciccotti and Ryckaert [14] in simulating a single Argon particle in an Argon fluid and by Toxvaerd [12, 36].

An alternative approach to provide a molecular basis for eliminating the solvent particles, also using projection operators, was presented by Mazur and Oppenheim [15] starting from the Hamiltonian equations of motion. They obtained the Langevin equation for Brownian motion by performing an expansion in powers of $\lambda = m/M$ (mass solvent/mass Brownian particles). They demonstrated that this equation is correct to order λ^2 and is valid for all times if the momentum of the heavy particle is restricted to be of order λ^{-1}. They also showed that the friction coefficient appearing in the Langevin equation is identical to the friction coefficient on a macroscopic body moving with a prescribed velocity in a viscous medium. This approach was extended to N interacting particles [16, 17]. In contrast to the

case of a single heavy particle, the *friction tensor depends on the instantaneous separation between the particles* and the fluctuation-dissipation relationship is modified. This derivation does not apply for a system that displays memory effects. However, they explicitly consider molecules of different types and introduce the concept of a potential of mean force.

The salient features of this derivation are reproduced here to introduce the concept of a potential of mean force. Consider a system of n Brownian particles with mass M and described by generalised coordinates $(\mathbf{R}^n, \mathbf{P}^n)$ and N bath molecules of mass m and coordinates $(\mathbf{r}^N, \mathbf{p}^N)$. The system Hamiltonian may be separated into a contributions from the bath particles (H_o) and Brownian particles (H_B).

$$H = H_o + H_B \tag{2.12}$$

where

$$H_B = \frac{\mathbf{P}^n \bullet \mathbf{P}^n}{2M} + V(\mathbf{R}^n) \tag{2.13}$$

and

$$H_o = \frac{\mathbf{p}^N \bullet \mathbf{p}^N}{2m} + U(\mathbf{r}^N) + \sum_{\mu=1}^{n} \phi_\mu(\mathbf{r}^N, \mathbf{R}_\mu) \tag{2.14}$$

$V(\mathbf{R}^n)$ are the short range interaction potentials between the Brownian particles while $U(\mathbf{r}^N)$ are the analogous interaction potential between bath particles. $\phi_\mu(\mathbf{r}^N, \mathbf{R}_\mu)$ describes the interaction between the Brownian molecule μ and the N bath molecules. They define a projection operator $\mathcal{P}$ by the equation :

$$\mathcal{P}A = < A > = \frac{\int A e^{-\beta H_o} d\mathbf{r}^N d\mathbf{p}^N}{Z} \tag{2.15}$$

where Z is the corresponding configurational integral

$$Z(\mathbf{R}^n) = \int e^{-\beta H_o} d\mathbf{r}^N d\mathbf{p}^N \tag{2.16}$$

Note that the projection operator essentially integrates out all degrees of freedom associated with the bath molecules by taking an ensemble average of these variables for a particular configuration of Brownian particles $(\mathbf{R}^n)$. A may represent any dynamic variable in the system. The system Hamiltonian used in the definition of the projection operator (H_o as given in Eq. 2.14) is for a system in which interactions between the Brownian particles

are excluded. The interaction between the Brownian particles and the solvent are however included in H_o.

A potential of mean force $\chi(\mathbf{R}^n)$ was defined by :

$$Z(\mathbf{R}^n) = C(N, V, \beta)e^{-\beta\chi(\mathbf{R}^n)} \tag{2.17}$$

By differentiating Eq. 2.16 and remembering that $\frac{\nabla_{\mathbf{R}_\mu} Z}{Z} = \nabla_{\mathbf{R}_\mu} \ln(Z)$ one can show that:

$$< \nabla_{\mathbf{R}_\mu} \phi_\mu >= -\frac{\nabla_{\mathbf{R}_\mu} \ln(Z)}{\beta} = \nabla_{\mathbf{R}_\mu} \chi(\mathbf{R}^n) \tag{2.18}$$

and hence the average force on the Brownian particle $< \mathbf{F}_\mu >$ can be expressed in terms of two components, one arising from Brownian-Brownian interactions and the other arising from the solvent,

$$< \mathbf{F}_\mu >= - < \nabla_{\mathbf{R}_\mu}(V + \phi_\mu) >= -\nabla_{\mathbf{R}_\mu}[V + \chi(\mathbf{R}^n)] \tag{2.19}$$

It is important to realise that the potential of mean force $\chi(\mathbf{R}^n)$ is a function of the coordinates of the N Brownian particles and an expression for this must still be obtained.

For times $t > \tau_b$, where τ_b is the longest relaxation time for the bath, it was shown that higher order terms in an expansion in λ could be ignored for all times and the following momentum Langevin equation was obtained

$$\dot{\mathbf{P}}_\nu = \mathbf{S}_\nu + \mathbf{E}_\nu - \sum_\mu \mathbf{P}_\mu \cdot \zeta_{\mu,\nu}(\mathbf{R}^n) \tag{2.20}$$

where $\mathbf{S}_\nu$ is the force acting on the Brownian particle, $\mathbf{E}_\nu$ is the fluctuating force with properties

$$< \mathbf{E}_\nu > \quad = 0 \tag{2.21}$$

$$< \mathbf{E}_\mu \mathbf{E}_\nu(t) > \quad = 2Mk_BT\zeta_{\mu,\nu}(\mathbf{R}^n)\delta(t) \tag{2.22}$$

The frictional tensors, $\zeta_{\mu,\nu}$, are implicitly time-dependent through the dependence on the coordinates of the Brownian particles. The position-dependent frictional tensors reflect the physical fact that solvent flow introduced by one molecule will have an effect through

the frictional term on the other molecules. An algorithm was developed by Ermak and McCammon [18] to solve Eq. 2.20 including hydrodynamic interactions. The long range nature of the hydrodynamic interactions makes this approach computationally unsuitable for large systems (order N^3). The inclusion of short range lubrication effects has been performed by Brady [19].

2.1.2 Fokker-Planck and related equations

The problem of Brownian motion may be recast in a totally equivalent framework, namely by deriving an equation for the full distribution function $W(\{\mathbf{r}\},\{\mathbf{u}\},t|\{\mathbf{r}_0\},\{\mathbf{u}_0\})$, which is the probability that the particles are located at a particular point in full phase space $(\{\mathbf{r}\},\{\mathbf{u}\},t)$ at time t subject to their being located at $(\{\mathbf{r}_0\},\{\mathbf{u}_0\})$ at time $t=0$. Initially this problem was presented in velocity space by Fokker and more generally by Planck. Smoluchowski presented a co-ordinate space description. Many full phase space generalizations have been presented [4, 20, 21] but this discussion will be restricted to Chandrasekhar's [21] derivation for a single Brownian particle. The full Fokker-Planck-Klein-Kramers equation which is valid for N interacting Brownian molecules including hydrodynamics is then presented without further justification.

Chandrasekhar equation

Assuming that diffusion in phase space is a Markov process (i.e. independent of past history), we would expect that we could derive $W(\mathbf{r},\mathbf{u},t+\Delta t)$ from $W(\mathbf{r},\mathbf{u},t)$ and from a knowledge of the transitional probability $\psi(\mathbf{r},\mathbf{u};\Delta\mathbf{r},\Delta\mathbf{u})$. This can be expressed by

$$W(\mathbf{r},\mathbf{u},t+\Delta t)=\int\int W(\mathbf{r}-\Delta\mathbf{r},\mathbf{u}-\Delta\mathbf{u},t)\psi(\mathbf{r}-\Delta\mathbf{r},\mathbf{u}-\Delta\mathbf{u};\Delta\mathbf{r},\Delta\mathbf{u})d(\Delta\mathbf{r})d(\Delta\mathbf{u}) \quad (2.23)$$

All terms in equation (2.23) are then expanded using Taylor series about the point $(\mathbf{r},\mathbf{u},t)$ to obtain

$$(\frac{\partial W}{\partial t}+\mathbf{u}\cdot\nabla_{\mathbf{r}}W)\Delta t+O(\Delta t^2) = -\sum_j \frac{\partial(W<\Delta u_j>)}{\partial u_j}+\frac{1}{2}\sum_j \frac{\partial^2(W<\Delta u_j^2>)}{\partial {u_j}^2} \quad (2.24)$$

$$+\sum_{i<j}\frac{\partial^2(W<\Delta u_j\Delta u_i>)}{\partial u_i\partial u_j}+\cdots \quad (2.25)$$

From a knowledge of the averages $< \Delta u_j >$, which are determined from the transition probability, equation (2.25) reduces to [4, 21]

$$\frac{\partial W}{\partial t} + \mathbf{u} \cdot \nabla_{\mathbf{r}} W + \mathbf{K} \cdot \nabla_{\mathbf{u}} W = \xi div_{\mathbf{u}}(W\mathbf{u}) + \frac{\xi k_B T}{m} \nabla^2_{\mathbf{u}} W \tag{2.26}$$

where $\mathbf{K}$ is an external force acting on the particle.

Fokker-Planck-Klein-Kramers equation

The following equation was derived for a system of N interacting particles. The effects of hydrodynamics were included through the presence of a position-dependent interparticle friction tensor ξ_{ij} [22].

$$\frac{\partial W}{\partial t} + \sum_i (m_i^{-1} \mathbf{p}_i \cdot \nabla_{\mathbf{r}_j} W + \mathbf{K}_i \cdot \nabla_{\mathbf{p}_i} W) = \sum_i \sum_j \nabla_{\mathbf{p}_i} \cdot \xi_{ij} \cdot (m_i^{-1} \mathbf{p}_i W + k_B T \nabla_{\mathbf{p}_j} W) \tag{2.27}$$

An equation of this form was also derived by Zwanzig [23] for polymeric systems.

2.1.3 Equivalence

Much work has been performed to demonstrate the equivalence of these equations. Equation (2.27) has also been derived from microscopic considerations [16, 17] and Lax [24] deals with noise in the Langevin methods and the equivalent probability description. Numerous papers [22, 25, 26] have dealt with the simplification of the Fokker-Planck-Klein-Kramers equation to yield the Smoluchowski equation (i.e. Fokker-Planck equation in co-ordinate space) and with rewriting the momentum Langevin equation (which generates the trajectories of the particles) in the form of Smoluchowski equation.

2.2 Application of Langevin Equations

The simplest form of the GLE (Eq.2.4) is to assume that the memory function is delta correlated in time, i.e. there is no memory. This approach has been used to obtain equilibrium and dynamic properties of a single n-butane and n-decane molecule and the results were compared to corresponding multiple chain MD simulations [27]. The configuration of the dihedral angle in butane was very different from the MD result and this was ascribed to

neglected solvent effects in the potential. The results for decane more closely resembled the MD results. The diffusive Langevin equation was employed by Levy *et al.* to investigate the dynamics of model alkanes. The diffusive limit occurs at high frictional coefficient and results in the neglect of the inertial term in Eq. 2.8. Solvent effects were accounted for using a potential of mean force. The dynamics of gauche-trans transitions were discussed in term of Kramers rate theory since the form of the potential energy barrier is known. A lipid chain in a membrane bilayer [28] was studied in the diffusive limit with a mean field potential to account for the membrane. A solvent-modified potential, obtained using Orstein-Zernike-like integral equations, was used in simulations of alanine-dipeptide [29]. The frictional coefficients were determined using the accessible surface area methodology as suggested by Pastor and Karplus [30]. Grest and Murat have applied SD to grafted polymer brushes [31] and dendrimer molecules [32] in solvents. The effect of solvent quality was indirectly accounted for by varying the cut-off distance of the polymer constituents. A bad solvent for the polymer would thus be represented by attractive interactions between the polymer constituent particles. See Binder [33] for more details and examples of the use of SD in polymer simulations.

SD has also been applied to n-alkane melts confined between solid surfaces [34, 35] and is used because SD, when compared to MC, has superior sampling properties. The self-diffusion of polyethylene calculated from SD was found to be dependent on the frictional coefficient and the MD result was recovered only at very small frictional values ($\xi \approx 1/7500$ fs^{-1}). These simulations examined multiple chains at liquid densities and hence the stochastic noise term is used as a means of temperature control and not as a method to account for solvent.

Memory effects have been included, particularly in the study of single component systems. Typically a single atom is simulated using the GLE and then compared to a full MD simulation. For example, Ciccotti and Ryckaert [5] used the continued fraction methodology to account for memory effects in simulations of an argon particle in an argon fluid. Toxvaerd calculated the coefficients in the Mori expansion of the velocity autocorrelation function from MD [13] and solved the GLE with a Gaussian memory function [36] in 2D. A nonamer in a LJ solvent was also simulated using Gaussian memory [8] and structural and dynamic properties determined. The dynamic properties where found to be represented more faithfully using memory, however the structural properties appeared not to be

influenced.

Ermak and McCammon incorporated hydrodynamic interactions [18] and have evaluated the influence of the Oseen [37] and Rotne-Prager [38] diffusion tensors on the behaviour of rigid rod dimers and trimers in the diffusive limit. Extenstions have included the incorporation of rotational effects [39, 40].

A important application of SD and BD simulations has been the description of large biological macromolecules. For example the macromolecular diffusion of a mixture of uniformly charged spheres, representing ribosome, protein and tRNA at their physiological concentrations was perfomed [41]. The system was chosen to replicate macromolecular diffusion in the cytoplasm of the bacterium *Escherichia coli.* Brownian dynamics, where the inertial terms are neglected, have been employed to determine the bending and twisting dynamics of short linear DNA chains [42].

In summary, a firm theoretical basis exists for projecting out the rapidly varying solvent contributions and incorporating their effects through a stochastic noise term and a modified interaction potential. The vast majority of work done, however, use simplified version of the generalised Langevin equation for computational reasons. We have followed a similar approach in trying to simulate surfactant self-assembly using SD with a delta correlated memory kernel. Chapter 3 describes the alogorithm employed and in Chapter 4 equilibrium properties of the model amphiphile, A_2B_2, are presented.

Bibliography

[1] M. P. Allen and D. J. Tildesley, *Computer Simulations of Liquids*, (Oxford Science Publications, Oxford Press, 1992).

[2] J. W. Rudisill and P. T. Cummings, Journal of Non–Newtonian Fluid Mechanics **41,** 275 (1992).

[3] H. Mori, Progress of Theoretical Physics **33,** 423 (1965).

[4] D. A. McQuarie, *Statistical Mechanics*, (HarperCollins, 1976).

[5] G. Ciccotti and J-P. Ryckaert, J. Statis. Phys. **26,** 73 (1981).

[6] G. Bossis, B. Quentrec, and J. P. Boon, Molecular Physics **45,** 191 (1982).

[7] W. F. van Gunsteren and H. J. C. Berendsen, Molecular Physics **47,** 721 (1982).

[8] S. Toxvaerd, J. Chem. Phys. **86,** 3667 (1986).

[9] M. Berkowitz, J. D. Morgan, and J. A. McCammon, J. Chem. Phys. **78,** 3256 (1983).

[10] G. Ciccotti and J.-P Ryckaert, Molecular Physics **40,** 141 (1980).

[11] H. Mori, Progress of Theoretical Physics **34,** 399 (1965).

[12] L. L. Lee, Physica **100A,** 205 (1980).

[13] S. Toxvaerd, J. Chem. Phys. **81,** 5131 (1984).

[14] G. Ciccotti and J.-P Ryckaert, Molecular Physics **46,** 875 (1982).

[15] P. Mazur and I. Oppenheim, Physica **50,** 241 (1970).

[16] J. M. Deutch and I. Oppenheim, J. Chem. Phys. **54,** 3547 (1971).

[17] J. Albers, J. M. Deutch, and Irwin Oppenheim, The Journal of Chemical Physics **54,** 3541 (1971).

[18] D. L. Ermak and J. A McCammon, The Journal of Chemical Physics **69,** 1352 (1978).

[19] J. F. Brady, Ann. Rev. Fluid Mech. **20,** 111 (1988).

[20] H. A. Kramers, Physica **7,** 285 (1940).

[21] S Chandrasekhar, Review of Modern Physics **15,** 21 (1943).

[22] G. Wilemski, Journal of Statistical Physics **14,** 153 (1976).

[23] R. W Zwanzig, Advances in Chemical Physics **15,** 325 (1969).

[24] M. Lax, Review of Modern Physics **38,** 541 (1966).

[25] W Hess and R. Klein, Physica **94A,** 71 (1978).

[26] R. J. A. Tough, P. N. Pusey, H. N. W. Lekkerkerker, and C. van den Broeck, Molecular Physics **59,** 595 (1986).

[27] W. F. van Gunsteren, H. J. C. Berendsen, and J. A. C. Rullmann, Molec. Phys. **44,** 69 (1981).

[28] R. W. Pastor, R. M. Venable, and M. Karplus, J. Chem. Phys. **89,** 1112 (1988).

[29] P. E. Smith, B. M. Pettitt, and M. Karplus, J. Phys. Chem. **97,** 6907 (1993).

[30] R. W. Pastor and M. Karplus, J. Phys. Chem. **92,** 2636 (1988).

[31] G. S. Grest and M. Murat, Macromolecules **26,** 3108 (1993).

[32] M. Murat and G. S. Grest, Macromolecules **29,** 1278 (1996).

[33] K. Binder, *Monte Carlo and Molecular Dynamics Simulations in Polymer Science*, (Oxford University Press, New York, 1995).

[34] T. Matsuda, G. D. Smith, R. G. Winkler, , and D. Y. Yoon, Macromoleules **28,** 165 (1995).

[35] R. G. Winkler, T. Matsuda, and D. Y. Yoon, J. Chem. Phys. **98,** 729 (1993).

[36] S. Toxvaerd, J. Chem. Phys. **82,** 5658 (1985).

[37] H. Yamakawa, The Journal of Chemical Physics **53,** 436 (1970).

[38] J. Rotne and S. Prager, The Journal of Chemical Physics **50,** 4831 (1969).

[39] M. H. Peters and R. Ying, J. Chem. Phys. **98,** 6492 (1993).

[40] E. Dickinson, S. A. Allison, and J. A. McCammon, J. Chem. Soc., Faraday Trans. 2 **81,** 591 (1985).

[41] D. J. Bicout and M. J. Filed, J. Phys. Chem. **100,** 2489 (1996).

[42] S. Allison, R. Austin, and M. Hogan, J. Chem. Phys. **90,** 3843 (1989).

Chapter 3

Stochastic Dynamics Simulation Code

3.1 Equation of motion

A third order integration algorithm for stochastic dynamics (SD) simulations was implemented based on the work of van Gunsteren and Berendsen [1, 2]. The equation of motion for each particle i to be integrated is :

$$m_i\dot{\mathbf{v}}_i(t) = -m_i\xi_i\mathbf{v}_i(t) + \mathbf{F}_i(\{\mathbf{x}_i(t)\}) + \mathbf{R}_i(t) \tag{3.1}$$

where m_i is the mass of particle i and $\mathbf{x}_i$, $\mathbf{v}_i$, $\mathbf{F}_i$ and ξ_i represent the position, velocity, force, and frictional (damping) coefficient acting on particle i respectively. This represents the simplest form of the GLE and assumes that the stochastic force contains no correlations in space or time; it is sometimes referred to as Brownian Dynamics (especially in the diffusive limit). The force, $\mathbf{F}_i$, is the explicit force between the N particles in the system (hence the dependence on the coordinate set $\{\mathbf{x}_i(t)\}$) and may include bond-length, bond-angle and solvent mediated potentials in order to represent real systems more accurately.

The stochastic force $\mathbf{R}_i$ is assumed to be stationary (magnitude time invariant) , Markovian (independent of past history), Gaussian with zero mean, and to have no correlation with prior velocities nor with the systematic force. These requirements dictate that $\mathbf{R}_i$ must satisfy the conditions

$$< \mathbf{R}_i(t) >= 0 \tag{3.2}$$

$$< R_{i\alpha}(t)R_{j\beta}(t') >= 2k_BT\xi_i m_i \delta_{i,j}\delta_{\alpha,\beta}\delta(t-t') \tag{3.3}$$

The indices α, β denote the Cartesian coordinate directions (x,y,z) while i, j denote particle labels.

The stochastic noise term acts as a heat bath to compensate for the energy sink due to viscous drag. The stationary solution is the Boltzmann distribution and hence these simulations produce canonical time averages (NVT ensemble). The dynamical properties are changed depending on their relaxation rate by the presence of the heat bath. To generate the correct gas phase MD dynamical behavior, $\frac{1}{\xi}$ must be larger than the relaxation time of the property of interest. On this time scale, however, the canonical ensemble is no longer simulated. On longer timescales, the dynamics are purely diffusive (Rouse-like dynamics). Equilibrium results are independent of the choice of the friction coefficient ξ and correspond to a gas phase constant temperature MD simulation with the same force field ($\mathbf{F}_i(\{\mathbf{x}_i(t)\})$). The utility of this approach is that the effect of the solvent on the dynamics should be realistic at long times.

Solution of the linear, inhomogeneous first order differential equation (Eq. 3.1) and integration over the noise term, yield the following discretized equations for the particle trajectories :

$$\begin{aligned}\mathbf{x}(t_n+\Delta t) = \; & \mathbf{x}(t_n)[1+e^{-\xi\Delta t}] - \mathbf{x}(t_n-\Delta t)e^{-\xi\Delta t} + \\ & m^{-1}\mathbf{F}(t_n)(\Delta t)^2(\xi\Delta t)^{-1}[1-e^{-\xi\Delta t}] + \\ & m^{-1}\dot{\mathbf{F}}(t_n)(\Delta t)^3(\xi\Delta t)^{-2}\left(\tfrac{1}{2}\xi\Delta t[1+e^{-\xi\Delta t}] - [1-e^{-\xi\Delta t}]\right) + \\ & \mathbf{X}_n(\Delta t) + e^{-\xi\Delta t}\mathbf{X}_n(-\Delta t) + O[(\Delta t)^4]\end{aligned} \tag{3.4}$$

where $\mathbf{X}_n(\Delta t) = (m\xi)^{-1}\int_{t_n}^{t_n+\Delta t}[1-e^{-\xi(t_n+\Delta t-t)}]\mathbf{R}(t)dt$. It should be noted that $\mathbf{X}_n(-\Delta t)$ is correlated with $\mathbf{X}_{n-1}(\Delta t)$ since they correspond to different integrals over the same time interval of $\mathbf{R}(t)$. Therefore, $\mathbf{X}_n(-\Delta t)$ and $\mathbf{X}_{n-1}(\Delta t)$ obey a bivariate Gaussian distribution [1].

As $\xi \to 0$, this equation simplifies to the MD Verlet algorithm [3]. As in the Verlet algorithm, the velocity does not appear explicitly in Eq. 3.4, but an expression for $\mathbf{v}(t_n)$

may be derived

$$\begin{aligned}\mathbf{v}(t_n) = \; & \{[\mathbf{x}(t_n + \Delta t) - \mathbf{x}(t_n - \Delta t)] + m^{-1}\mathbf{F}(t_n)(\Delta t)^2(\xi\Delta t)^{-2}G(\xi\Delta t) - \\ & m^{-1}\dot{\mathbf{F}}(t_n)(\Delta t)^3(\xi\Delta t)^{-3}G(\xi\Delta t) + [\mathbf{X}_n(-\Delta t) - \mathbf{X}_n(\Delta t)]\}H(\xi\Delta t)/\Delta t\end{aligned} \tag{3.5}$$

where $H(\xi\Delta t) = \xi\Delta t/[e^{+\xi\Delta t} - e^{-\xi\Delta t}]$ and $G(\xi\Delta t) = [e^{+\xi\Delta t} - 2\xi\Delta t - e^{-\xi\Delta t}]$.

It can be shown, by a Taylor series expansion of the exponential terms in $\xi\Delta t$, that the term containing the derivative of the force $\dot{\mathbf{F}}$, is of order $(\Delta t)^4$, and therefore is of the same order as the truncation error. It was therefore neglected in the algorithm that we employed.

An important feature of this algorithm is that the integration timestep is not restricted by ξ, since the stochastic force has been integrated over the interval Δt. Hence, the size of timestep (Δt) is only determined by the rate of change in the systematic force, i.e. on the interatomic potential. For a detailed description, showing the derivation of these equations and implementation, the reader is referred to van Gunsteren and Berendsen [1, 2].

3.2 Representation of Amphiphiles

The amphiphilic molecules are represented by either a coarse grained bead-rod or a bead-spring model. Physically, each bead may be thought of as being equivalent to a Kuhn length (order 10 methylene groups) on a polymer chain [4]. The bond connectivity is specified in the variable, *ilink*. Each bead is labelled (*itype*) to identify its amphiphilic nature. A typical amphiphile of form A_2B_2 would thus be characterised by the program variables

nbonds	3
ilink	1 2 2 3 3 4
itype	0 0 1 1

and describes three bonds connecting particles 1 and 2, 2 and 3, and 3 and 4 respectively. Particles 1 and 2 are of type 0 (hydrophobic), while particles 3 and 4 are of type 1 (hydrophilic). This completes the description of a single molecule. This method of describing a molecule can deal with branched surfactant molecules and mixed surfactant systems.

In the bead-rod model, the length of bond k between particles i and j, is rigidly constrained and is forced to satisfy the requirement

$$\sigma_k = \mathbf{x}_{ij}^2 - b_{ij}^2 = 0 \tag{3.6}$$

at all times, where $\mathbf{x}_{ij}$ is the vector from particle j to particle i in a molecule and b_{ij} is the desired bond-length. The force acting on particle i is subdivided into the contribution from the potential energy, V, and that associated with constraining the bond lengths

$$\mathbf{F}_i = -\nabla_i V(\{\mathbf{x}_i(t)\}) - \sum_{k=1}^{l} \lambda_k \nabla_i \sigma_k \tag{3.7}$$

where λ_k is the Lagrangian multiplier associated with bond k, and $\nabla_i = \frac{\partial}{\partial \mathbf{x}_i}$. At every timestep, the unknown set of Lagrangian multipliers needs to be solved for, such that the constraints given by Eq. 3.6 are satisfied. This process is performed iteratively using the SHAKE algorithm [5] with a tolerance of 10^{-5}.

In the bead-spring model, a harmonic potential is introduced along the bond direction

$$V_{ij}(bond) = \frac{1}{2} k(|\mathbf{x}_{ij}| - b_{ij})^2 \tag{3.8}$$

where the force constant, k is chosen so that 95 % of all bonds are within 2 % of the required bond-length. This large value of k ensures that we are operating in the overdamped regime. A practically rigid bond between neighboring units results.

The rigid bond and bead-spring formalism are not equivalent on a statistical mechanical basis [6]. In the rigid bond model, the conjugate momenta to the constrained degrees of freedom are set equal to zero and this gives rise to a correction factor in the partition function (related to the determinant of the metric tensor) as first indicated by Fixman [7]. This correction factor can be taken into account by including a compensating potential energy term of the form

$$V' = kT \ln\{g^{\alpha}(a)\}^{\frac{1}{2}} \tag{3.9}$$

where $\{g^{\alpha}(a)\}^{\frac{1}{2}}$ is the determinant of the metric tensor and a is the set of unconstrained variables. If bond length and bond angle constraints are employed, the influence of the correction term is significant and should be included [8], however if only bond length constraints are employed, as in our work, this correction may be safely ignored [9].

Bond angle and torsional potentials are not employed in this work, but their implementation is straightforward.

3.3 Program Structure

The program structure is shown schematically in Figure 3-1 and is very similar in structure to any MD algorithm [3, 10], except in the specific form of the equation of motion. At every timestep, the force between all particles is calculated in the subroutine EVAL. Subsequently,the calculated forces are used to determine the new particle positions and velocities in the subroutine TIMESTEP according to Eq. 3.4 and Eq. 3.5. If rigid bonds are employed, the unconstrained position and velocities are shaken. The physical properties of the system can then be calculated. This sequence of steps is repeated for each timestep. Periodically the neighbour and linked lists are updated (whenever mod(kb,10) = 0, kb = timestep). Periodic boundary conditions and Newton's second law of motion are used throughout. The majority of the program was written in FORTRAN 77 (modified from the Haile code [10]), the only exception being subroutines that required recursion, which were written in ANSI C for the sake of portability.

3.3.1 Neighbour and Linked Lists

Two techniques are employed to make the algorithm more efficient. The first is the implementation of the Verlet neighbour list [11]. The neighbour list contains all atom pairs within a prescribed distance r_{list} and is typically generated every 10 or 20 timesteps. The distance r_{list} is chosen to be larger than the potential cut-off distance employed (r_c), so that the neighbour list also contains particles that lie in a spherical shell of thickness $r_{list} - r_c$ outside the potential cut-off distance. This approach ensures that particles which may diffuse into the interaction sphere, before the neighbour list is updated, are correctly accounted for. This reduces the force calculation from an N_p^2 operation to an $N_p \times N_n$ operation, where N_p is the number of particles in the system and N_n is the average number of neighbours per particle. The generation of the neighbour list is still an N_p^2 operation but it is only performed every 10-20 timesteps.

For very large systems, the generation of the neighbour list may be improved by implementing a cell structure and linked list [3]. The simulation domain (cubic in our case) is subdivided in smaller cubes, called cells, with minimum length equal to r_{list}. For each cell, a linked list is generated containing all particles that reside in the spatial domain of that cell (order N_p calculation). The neighbour list of all particles in a cell can then be

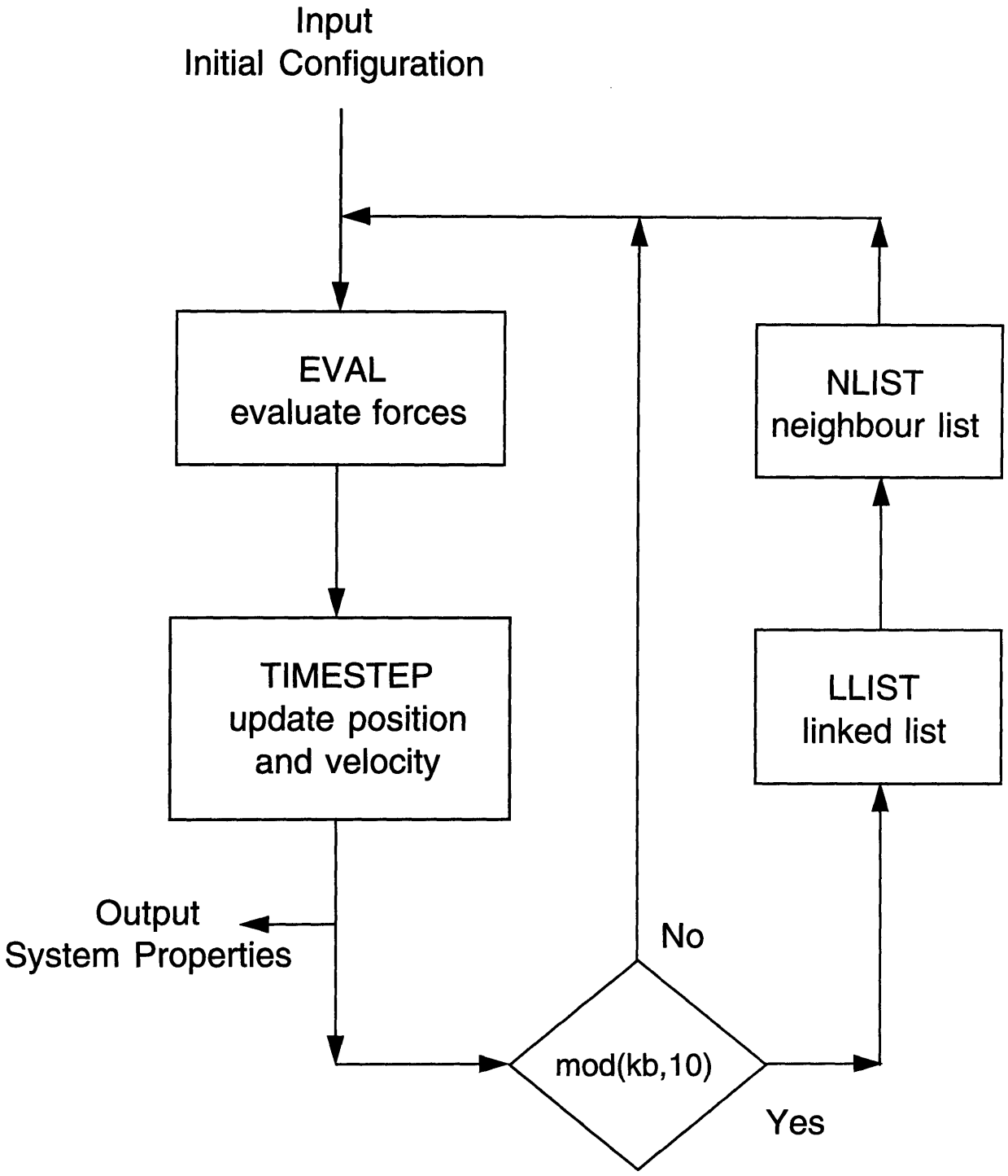

Figure 3-1: Stochastic Dynamics program schematic

generated by looping over the particles in that cell and the neighbouring 13 cells (employing Newton's second law of motion). Hence the generation of the neighbour list is now a $(13+1) \times (N_p/N_{cell}) \times N_p$ calculation, N_{cell} is the number of cells, and hence (N_p/N_{cell}) represents the average number of particles per cell. This technique is very useful when the simulation domain is very large in comparison to the potential cut-off distance. The neighbour list, *nlist*, is only uni-directional, i.e. if particle i sees particle j then particle j will not see particle i. This is a direct consequence of employing Newton's second law of motion and in the absence of cell linked lists is normally generated by requiring $i < j$. If, however, cells are employed in the generation of the neighbour lists, the requirement $i < j$ is employed only if both particles forming the pair reside in the same cell. For pairs spanning cell boundaries, looping over the 13 neighbouring cells ensures the uni-directional nature of *nlist*. This uni-drectional nature poses problems in identifying clusters as will be discussed in section 3.4

3.3.2 Noise Term

The noise term is sampled from a bivariate Gaussian distribution [1], by sampling first from one variable's distribution and subsequently sampling the conditional distribution for the other variable, given the value obtained for the first variable. To implement this, we need to sample Gaussian distributions of zero mean and different widths. This is achieved by employing the Box-Muller method [12] which comprises two steps :

1. Generate uniform random variates ψ_1 and ψ_2 on the interval (0 1). This is performed using the routine RAN1 [12], which employs three congruential generators and has essentially an infinite period.

2. Transform the uniform deviates (ψ) into Gaussian deviates (ζ) with zero mean and unit variance.

$$\zeta_1 = -2(\ln \psi_1)^{\frac{1}{2}} \cos(2\pi\psi_2), \quad \zeta_2 = -2(\ln \psi_1)^{\frac{1}{2}} \sin(2\pi\psi_2)$$

3.4 Identifying Aggregates

In order to identify and characterise aggregate structures that are formed in the course of the simulation, a definition of an aggregate is required.

A molecule is defined as being part of an aggregate if any of its hydrophobic constituents ($itype = 0$) are within a prescribed distance of another molecule's hydrophobic constituents. These molecules are said to be associated. This distance, $r_{cluster}$, was taken to be 1.5 σ, where σ is the characteristic length scale in the interatomic potential. The definition is in line with that used by Smit *et al.* [13] and the results are not sensitive to the exact value of $r_{cluster}$. The identification of associated molecules was implemented in EVAL where we determine all interparticle distances, and the result is stored in the variable *mlist*. A pointer, *mpoint*(i), is used to identify the location of particle i's associates within *mlist*. At this stage we have a uni-directional (due to Newton's second law) list of particles and their associates. The challenge lies in converting this information in an efficient manner into a list of numbered aggregates with unique constituents. A recursive procedure is used

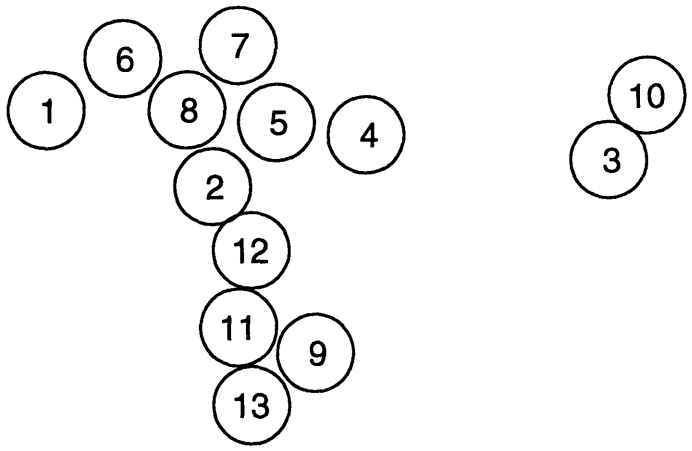

Figure 3-2: Schematic of two hypothetical clusters with aggregation number 2 and 11

to identify the aggregates, given the information stored in *mlist*, and to assign each cluster a unique identifer. This procedure is described briefly for the cluster grouping shown in Figure 3-2. The elements of *mpoint* and *mlist* are given in Table 3.1. Particle 1 has only one associate, namely particle 6, while particle 12, for example, has associates 2 and 11. Notice that the list is uni-directional in that particle 12 has particle 2 as an associate and hence particle 2 does not see particle 12. Also important is that this uni-directional property is determined by the subdivision of the simulation domain into cells and not by the requirement that $i < j$. Subroutine FIND is responsible for the cluster identification and proceeds by looping over the particles i. For example, for $i = 1$, FIND identifies 6 as

Table 3.1: Elements of arrays *mpoint* and *mlist* corresponding to cluster configuration shown in Figure 3-2.

i	mpoint(i)	mlist(mpoint(i)) ... mlist(mpoint(i+1)-1)
1	1	6
2	2	5, 8
3	4	10
4	5	5
5	6	7, 8
6	8	8
7	9	-
8	9	7
9	10	11, 13
10	12	-
11	12	13
12	13	2, 11
13	15	-

belonging to the same cluster as 1, then checks the associates of 6 which is found to be 8, which in turn is associated with particle 7 (recursive part). At this stage there are no more associates that are accessible from information of particle 1,6,8 or 7 and hence the grouping (1,6,8,7) is identified as a cluster and assigned the label 1. Similarly, $i = 2$ has associates 8 and 5, of which 8 already has a cluster label associated with it (namely 1), while 5 has associates 7 and 8 which already have been identified as belonging to cluster 1. Hence the group (1,6,8,7,5,2) are now all part of cluster 1, and we proceed to $i = 3$ which leads us to the group (3,10) which is assigned the cluster label 2. This procedure is repeated for each i which has not been assigned a cluster number. The difficulty associated with a uni-directional list is demonstrated by particle $i = 9$ that has particles 11 and 13 associated with it. Particle 11 has the associate 13, while particle 13 has no associates. Hence the grouping (9,11,13) will be labelled as cluster 3. Only on reaching $i = 12$ does one discover that particle 2 (in cluster 1) and particle 11 (which is in cluster 3) reside in the same cluster through the common link of particle 12. All particles in cluster 3 have then to be reassigned to cluster 1.

Once the clusters have been identified, cluster specific information can be determined, such as the radial distribution function through clusters with a certain aggregation number, average aggregation numbers, etc. Such physical properties will be defined where they are employed and will not discussed any further at this stage.

3.5 Summary

A third order integration algorithm is employed to solve Eq. 3.1. In the limit of a small frictional coefficient, the algorithm corresponds to the well known Verlet algorithm used in MD simulations. The program structure is similar to that used for MD and incorporates the well known optimization tools of neighbour list and the division of the simulation space into cells. The amphiphile molecules are represented as a string of beads. A clustering algorithm was developed to identify clusters. Chains are designated as belonging to a cluster if at least one of the hydrophobic beads is within a prescribed distance of a hydrophobic bead on they other chain.

Bibliography

[1] W. F. van Gunsteren and H. J. C. Berendsen, Molec. Phys. **34,** 1311 (1977).

[2] W. F. van Gunsteren and H. J. C. Berendsen, Molec. Phys. **45,** 637 (1982).

[3] M. P. Allen and D. J. Tildesley, *Computer Simulations of Liquids*, (Oxford Science Publications, Oxford Press, 1992).

[4] K. Binder, *Monte Carlo and Molecular Dynamics Simulations in Polymer Science*, (Oxford University Press, New York, 1995).

[5] J.-P. Ryckaert, G. Ciccotti, and H. J. C. Berendsen, J. Comp. Phys. **23,** 327 (1977).

[6] N. Gō and H. A. Scheraga, Macromolecules **9,** 535 (1976).

[7] M. Fixman, J. Chem. Phys. **69,** 1527 (1978).

[8] M. R. Pear and J. H. Weiner, J. Chem. Phys. **71,** 212 (1979).

[9] W. F. van Gunsteren, Molec. Physics **40,** 1015 (1980).

[10] J. M. Haile, *Molecular Dynamics Simulations : Elementary Methods*, (John Wiley & Sons, INC, New York, 1992).

[11] L. Verlet, Physical Review **159,** 98 (1967).

[12] William H. Press, Brian P. Flanner, Saul A. Teukolsky, and William T. Vetterling, *Numerical Recipes (Fortran Version)*, (Cambridge University Press, 1990).

[13] B. Smit, P. A. J. Hilbers, K. Esselink, L. A. M. Rupert, and N. M. van Os, J. Phys. Chem. **95,** 6361 (1991).

Chapter 4

Stochastic Dynamics Simulations of Self-Assembly

4.1 Introduction

The self-assembly of short amphiphilic molecules of type A_2B_2 (A = hydrophilic, B = hydrophobic) is investigated using Stochastic Dynamics simulations with a scalar frictional coefficient. The algorithm employed is as described in Chapter 3.

The surfactant molecules are represented by a coarse-grained bead-rod model. Bond lengths were constrained iteratively using the SHAKE algorithm [1, 2] with $tol = 10^{-5}$. Bond angle constraints were not included, so the simulations represent flexible chains. Unshifted Lennard-Jones (LJ) interactions were employed between non-bonded beads, the nature of which could be varied by changing the cut-off distance r_c.

$$V(r) = \begin{cases} 4\epsilon\left[\left(\frac{\sigma}{r}\right)^{12} - \left(\frac{\sigma}{r}\right)^{6}\right] & r \leq r_c \\ 0 & r > r_c \end{cases} \tag{4.1}$$

where r is the separation distance and ϵ and σ are the well depth and size parameter, respectively, in the LJ potential. The bond-length was chosen to coincide with the minimum in the LJ potential ($2^{\frac{1}{6}}\sigma$).

Short diblock amphiphiles of type A_2B_2, where A and B are the hydrophilic and hydrophobic blocks respectively, were simulated. The B-B interactions were LJ attractive with a conventional cut-off distance of $r_c = 2.5\sigma$ while A-B and A-A interactions were purely

repulsive ($r_c = 2^{\frac{1}{6}}\sigma$). All beads were taken to have equal mass (m) and frictional coefficient (ξ).

Initially the surfactant chains were arranged on a fcc lattice. The surfactant concentration is given as a bead number density ($[S] = N_s N_b / V_{\rm sys}$, N_s is the number of surfactant molecules, N_b is the number of beads per surfactant molecule = 4, and $V_{\rm sys}$ is the simulation volume) which is directly proportional to volume fraction. Temperature is expressed in reduced units ($T_r = k_B T/\epsilon$). A reduced timestep ($t_r = t/\sigma\sqrt{(m/\epsilon)}$) of length $\Delta t_r = 0.005$ is used. The reduced frictional coefficient is given by $\xi_r = \xi\sigma\sqrt{(m/\epsilon)}$. Most simulations were performed at two system sizes (108 and 256 surfactants). No effect of system size was noted. At high number density ($[S] \geq 0.10$) 864 surfactants were used in the simulations. The simulations were run on a HP 735/125MHz workstation which took $2. \times 10^{-4}$ cpu seconds/timestep/molecule at $[S] = 0.12$. Typically 5 - 15 million timesteps were performed per simulation depending on system size.

Surfactant chains were designated as belonging to an aggregate, as discussed in Chapter 3, if any tail beads (B beads) of the surfactants were within a certain distance of each other ($r_{clust} = 1.5\sigma$) [3].

4.2 Simulation Results and Discussion

Each simulation trajectory was divided into two sections once equilibrium was judged to have been established. Equilibrium properties with error bounds were then calculated for these two sections by further subdivision into 5 parts. This procedure enabled us to determine if any drift in calculated values was evident from the first half of the simulation to the second half. Typically, the drift was well within the error bounds of the calculated values. For clarity, only the maximum error bar ($\pm$ standard deviation) is shown on the figures.

The choice of frictional coefficient, ξ, is determined by two conflicting requirements. At large ξ, the molecular diffusivity is low and therefore equilibration and sampling of configuration space is excruciatingly slow. For small ξ, the molecular diffusivity is high. Larger fluctuations in temperature, however, occur and we no longer strictly follow the canonical ensemble. Also at low ξ an additional term ($2 < \mathbf{v}(0) \cdot \mathbf{F}(0) > \delta(t)$) in the fluctuation dissipation relationship [4] becomes more significant. The effect of the additional

Table 4.1: Contribution of correction to fluctuation dissipation relationship as given by Eq. 2.10

ξ_r	$2 < \mathbf{v}(0) \cdot \mathbf{F}(0) > /\xi_r T_r$	$< T >$
0.1	0.0066	0.6022
1.0	0.0028	0.6018
10.0	0.0019	0.6008

term was evaluated by performing short runs ($t_r = 100$, $[S] = 0.12$, $T_r = 0.60$) in which the quantity $< \mathbf{v}(0) \cdot \mathbf{F}(0) >$ was evaluated and compared to the temperature contribution as shown in Table 4.1. Also shown is the calculated temperature $< T >$. The additional terms contribution is less than 1 % and may this be neglected.

4.2.1 Equilibrium Properties

The onset of micellisation is traditionally depicted by plotting the free (non-associated) surfactant concentration $[F]$ as a function of the total surfactant concentration $[S]$. Above a certain total surfactant concentration, called the critical micelle concentration (cmc), $[F]$ levels off. Figure 4-1 shows this behaviour at three temperatures. The cmc increases with increasing temperature as would be expected for a system with an enthalpic driving force for micellisation. At higher concentrations, a decline in free surfactant concentration is observed. Most existing theories [5, 6, 7, 8] suggest that the free surfactant concentration should remain constant or increase slightly above the cmc. An explanation for this deviation from ideal behavior is provided in the next section, 4.2.2.

The number averaged (N_n) and weight averaged (N_w) aggregation numbers are defined by

$$N_n = \frac{\sum_{s=1}^{\infty} s\rho_s}{\sum_{s=1}^{\infty} \rho_s} = \frac{N_s/\mathrm{V}_{sys}}{\sum_{s=1}^{\infty} \rho_s} \tag{4.2}$$

and

$$N_w = \frac{\sum_{s=1}^{\infty} s^2\rho_s}{\sum_{s=1}^{\infty} s\rho_s} \tag{4.3}$$

where ρ_s is the number concentration of aggregates of size s. These expressions include

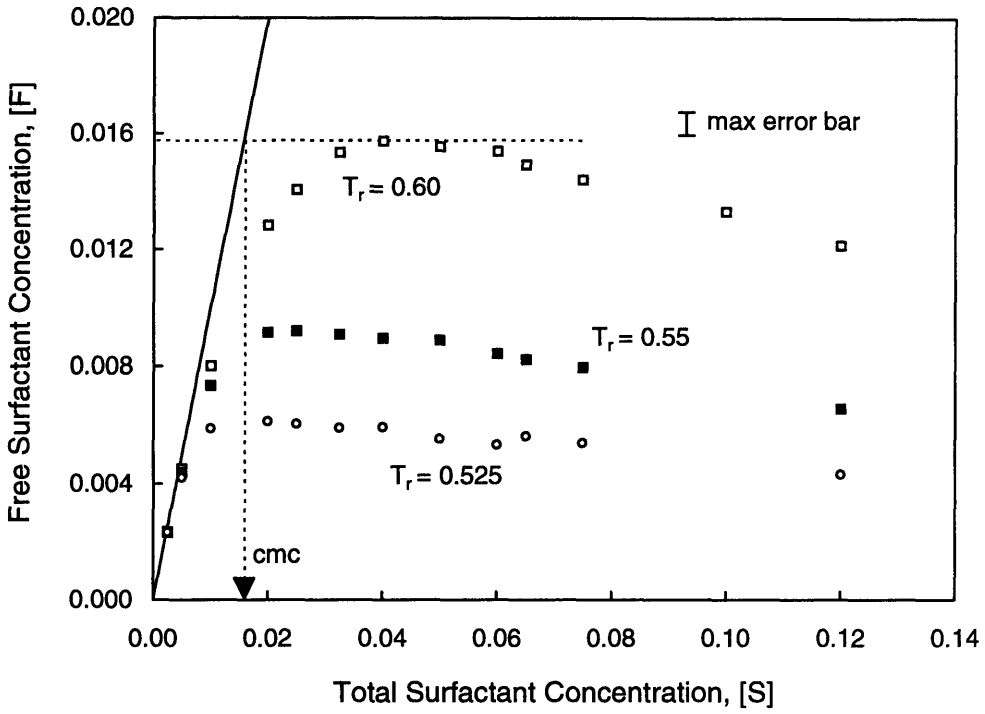

Figure 4-1: Variation of free surfactant concentration with total surfactant concentration indicating the onset of micellization and the definition of cmc.

the free surfactant in their definitions (as indicated by the summation from $s = 1$). An alternative definition that may be employed excludes free surfactants and is referenced as $N_w(ex)$ and $N_n(ex)$, the ratio of which is referred to as the polydispersity index [8]. Figure 4-2 shows a plot of the the number averaged and weight averaged aggregation numbers as a function of total surfactant concentration $[S]$. As the concentration increases above the cmc, the micelles formed grow in size. The polydispersity therefore varies from 1 below the cmc (essentially all surfactants are in monomers or dimers) to approximately 2 at higher concentrations.

By labelling a chain in an aggregate and then following the size of the aggregate in which the chain resides, one can observe how the chain samples aggregates of different sizes. This chain is referred to as a tracer chain. A tracer autocorrelation function [9] was used to estimate the correlation times within the system and hence to obtain a qualitative idea of the simulation times required to sample the equilibrium state of the system, where

$$A(\tau) = \frac{< N(t+\tau)N(t) > - < N(t) >^2}{< N^2(t) > - < N(t) >^2} \tag{4.4}$$

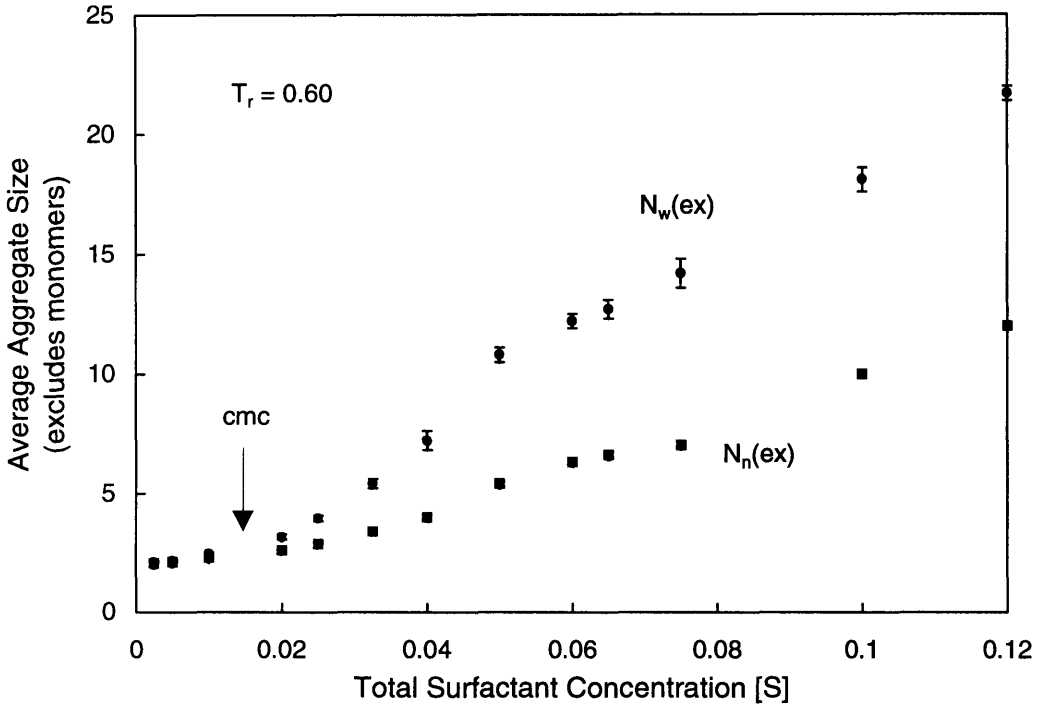

Figure 4-2: Increase in average micelle size with total surfactant concentrations ($[S]$) at $T_r = 0.60$

and $N(t)$ is the aggregate size in which the tracer chain resides at time t. The angular brackets indicate an ensemble average over all molecules taken successively as tracer chains, in addition to averaging over multiple time origins t. For $\tau = 0$, $A(\tau) = 1$ (perfectly correlated) while as $N(t+\tau)$ becomes uncorrelated with $N(t)$, $A(\tau) \to 0$. The tracer autocorrelation function provides an indication of how long it takes a tracer chain to sample all aggregate sizes. A correlation time (τ_c) was defined as the time required for $A(\tau)$ to reach a value of e^{-1}. At $[S] = 0.02$, before micelles form, $\tau_c = 5$ (Figure 4-3, $\xi_r = 0.1$). The short correlation time is indicative of the labile nature of the pre-micellar aggregates. Above the cmc, at $[S] = 0.065$ the correlation time is of the order $\tau_c = 125$, decreasing as the micelle concentration increases ($\tau_c = 80$, [S]=0.12). This decrease in τ_c is quantitatively consistent with the decrease in diffusional length between micelles due to the higher concentration. These results were checked and found to be independent of system size. They are, however, a function of ξ_r since this determines the diffusive time scale for the free surfactants. Typically, simulations times exceeded the tracer correlation time by a factor of 300 to 600.

An important consideration when simulating micelle formation is that the system should

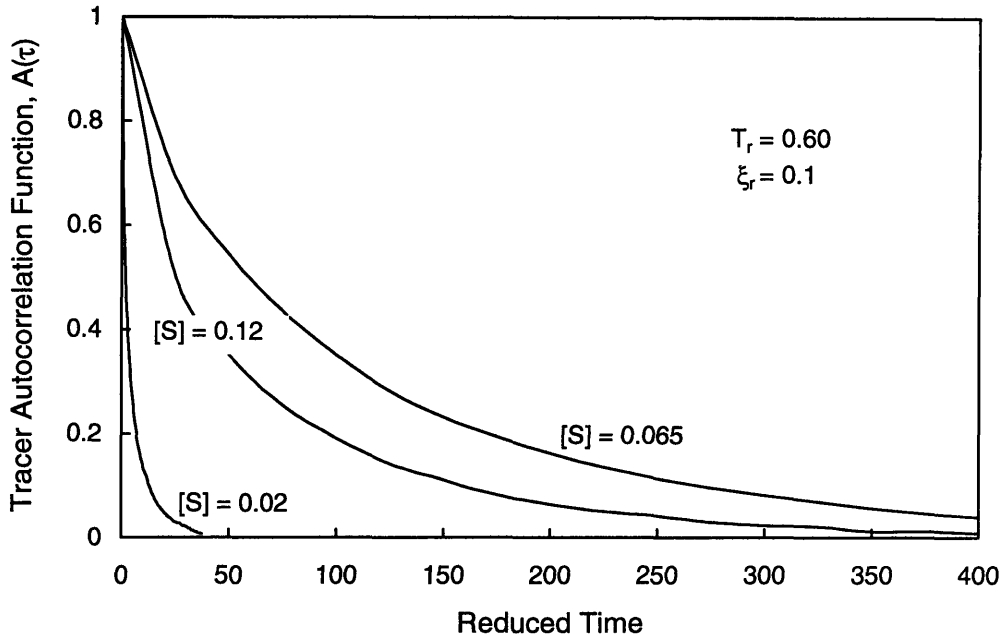

Figure 4-3: Tracer autocorrelation function ($A(\tau)$) for different total surfactant concentrations ($[S]$) at $T_r = 0.60, \xi_r = 0.1$.

not undergo macroscopic phase separation (e.g. into water and surfactant rich phases respectively). In our work, the invariance of the micelle size distribution as a function of time provided an indication that we were dealing with a homogeneous phase. In Figure 4-4 the running average of the weight averaged aggregation number is shown. Initially $N_w(ex)$ changes rapidly as micelles begin to form. Once the system has reached equilibrium, $N_w(ex)$ levels off and remains constant for the rest of the simulation. A time or system size dependence of this data would be indicative of phase separation. Furthermore, Larson [10, 11] and Mackie *et al.* [12] have performed Monte Carlo lattice simulation of A_2B_2 surfactants at $\chi = zN_b\Delta w/kT = 16$ (z = lattice coordination number = 26, N_b = surfactant chain length = 4, $\Delta w = \epsilon_{AB} - \frac{1}{2}(\epsilon_{BB} + \epsilon_{AA})$) and determined the phase behaviour. The ternary phase behavior (oil - B , water - A, surfactant - A_2B_2) at $\chi = 16$ showed two and three phase regions. In a system without an oil phase, however, no phase boundary is evident [12]. At $\chi = 16$, no micelle formation was observed by Larson [11]. Direct comparison with our work is difficult since we are dealing with an off-lattice simulation and continuous interaction potentials. However, selecting a coordination number of 11 (which corresponds to the first coordination shell), and converting our reduced temperature to that of Larson (in

their notation $\epsilon_{ow} = \epsilon_{ww} = 0$ and $\epsilon_{oo} = -1$), we get $\chi \approx 35$. Our temperature is therefore considerably lower (factor of 2) than that used by Larson and hence it is not surprising that micelles do in fact form.

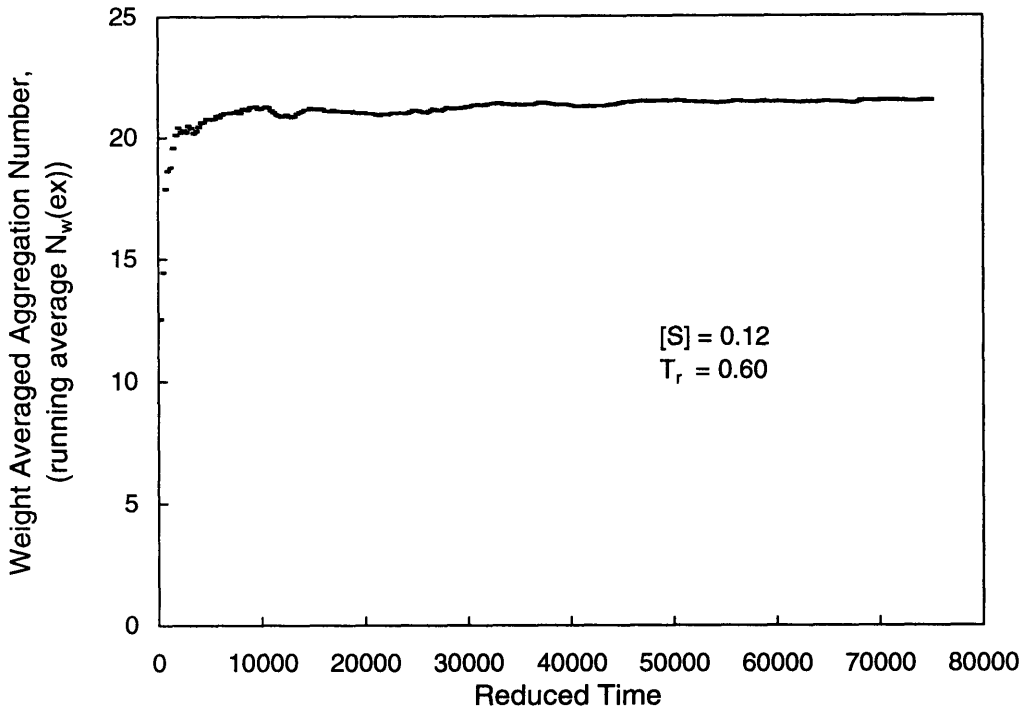

Figure 4-4: Equilibration of the weight averaged aggregation number

Figure 4-5a shows the simulated size distribution at three concentrations for a reduced temperature of $T_r = 0.60$. For $[S] = 0.02$ no micelles form because this concentration is below the cmc. As the concentration increases, a well developed maximum appears associated with the formation of spherical micelles. A shoulder in the size distribution at $s \approx 40$ is visible for $[S] = 0.12$ which is associated with a transition to rod-like micelles at higher concentrations (this is confirmed by a transition in the observed hard sphere radius of the system, which is discussed later). Similarly Figure 4-5b shows the effect of the reduced temperature on the micelle size distribution for $[S] = 0.12$. At lower temperatures the shoulder in the distribution has been reduced as spherical micelles are more strongly favored.

The observed shoulder is not an artifact of the simulation system size. This is demonstrated in Figure 4-6a where we present the size distribution at $T_r = 0.60$, $[S] = 0.60$ for system sizes 108 and 864 molecules respectively. The data points for the two systems are

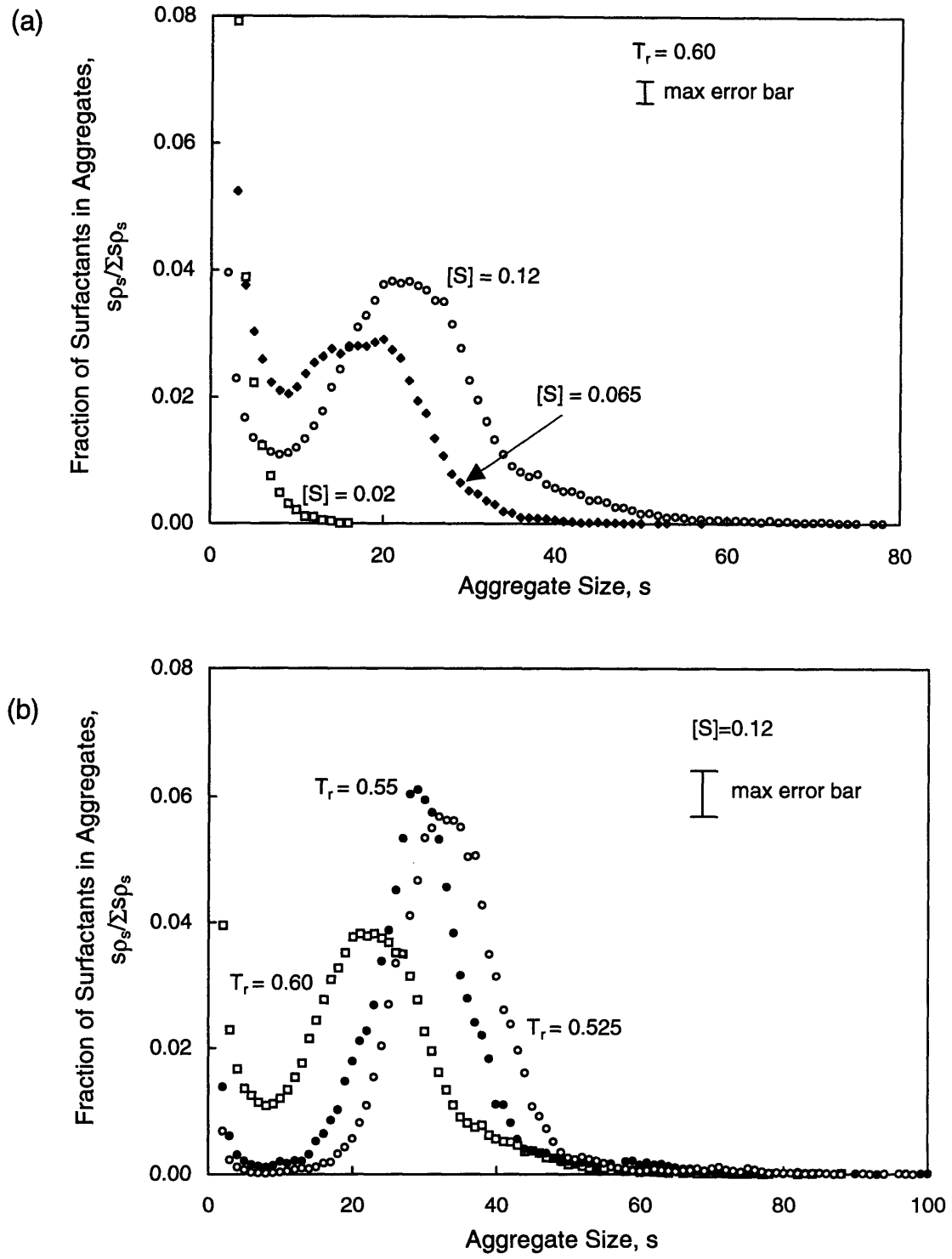

Figure 4-5: Effect of (a) $[S]$ at $T_r = 0.60$ and (b) T_r at $[S] = 0.12$ on micelle size distribution. ρ_s is the number density of aggregates with aggregation number s.

statistically indistinguishable and both display an asymmetric, long tail for high aggregation numbers. It is reassuring that starting from a totally different initial configuration the same equilibrium size distribution is obtained. Further indication of the independence of our results on system size is shown in Figure 4-6b, where the tracer autocorrelation function is shown for two system sizes, namely $N_s = 108$ and 256. The small deviation that is observed at long time ($t_r > 300$) is a consequence of the error associated with calculating the tracer autocorrelation function. The duration of the simulation for $N_s = 108$ was $t_r = 50000$, while that for $N_s = 256$ was only $t_r = 15000$, which is too short to probe a correlation function with time constant $\tau_c = 200$. The error at long times is expected to be around 3.5 % for the larger system and less than 1 % for $N_s = 108$ ($std \approx (2\tau_c/(N_s t_{run}))^{0.5}$ [13]). The correlation time ($\tau_c = 200$) is, as expected, considerably longer at the lower temperature ($T_r = 0.55$) compared to those presented in Figure 4-3.

An approximate idea of the shape of the aggregates can be obtained from the principal moments of inertia for each aggregate. This is achieved by calculating the ordered set (max $\rightarrow$ min) of eigenvalues $(\lambda_1, \lambda_2, \lambda_3)$ of the moment of inertia matrix $\mathbf{T}$. A component $T_{\alpha,\beta}$ in the moment of inertia of an aggregate of size s is given by

$$T_{\alpha,\beta} = \frac{\sum_{r=1}^{s}\sum_{i=1}^{N_b}(x_\alpha(r,i) - x_\alpha(cm))(x_\beta(r,i) - x_\beta(cm))}{sN_b} \tag{4.5}$$

where α and β represent any of the Cartesian coordinates; and the summations are over the molecules in the aggregate (r) and the individual particles (i) within each molecule. $\mathbf{x}(cm)$ is the micelle centre of mass. A characteristic length may be defined as $l_i = \sqrt{\lambda_i}$ for $i = 1, 2, 3$. A measure of the aggregate asphericity may then be obtained by monitoring $< l_1 > / < l_2 >$ and $< l_1 > / < l_3 >$ as functions of aggregate size as shown in Figure 4-7a. The micelles with aggregation numbers 10 - 35 appear to be almost spherical with aspect ratios of between 1.2 - 1.8. The aspect ratios for essentially spherical micelles are greater than unity because this technique of characterizing the micelle shape will always select the largest and shortest dimensions at a particular instant in time. Fluctuations in micelle shape, whether due to thermal motion or monomer insertion, are therefore accentuated and will not be averaged out. For low values of s, say $10 < s < 20$, cylindrical micelles are virtually forbidden on geometric grounds; so fluctuations in micelle shape must be entirely

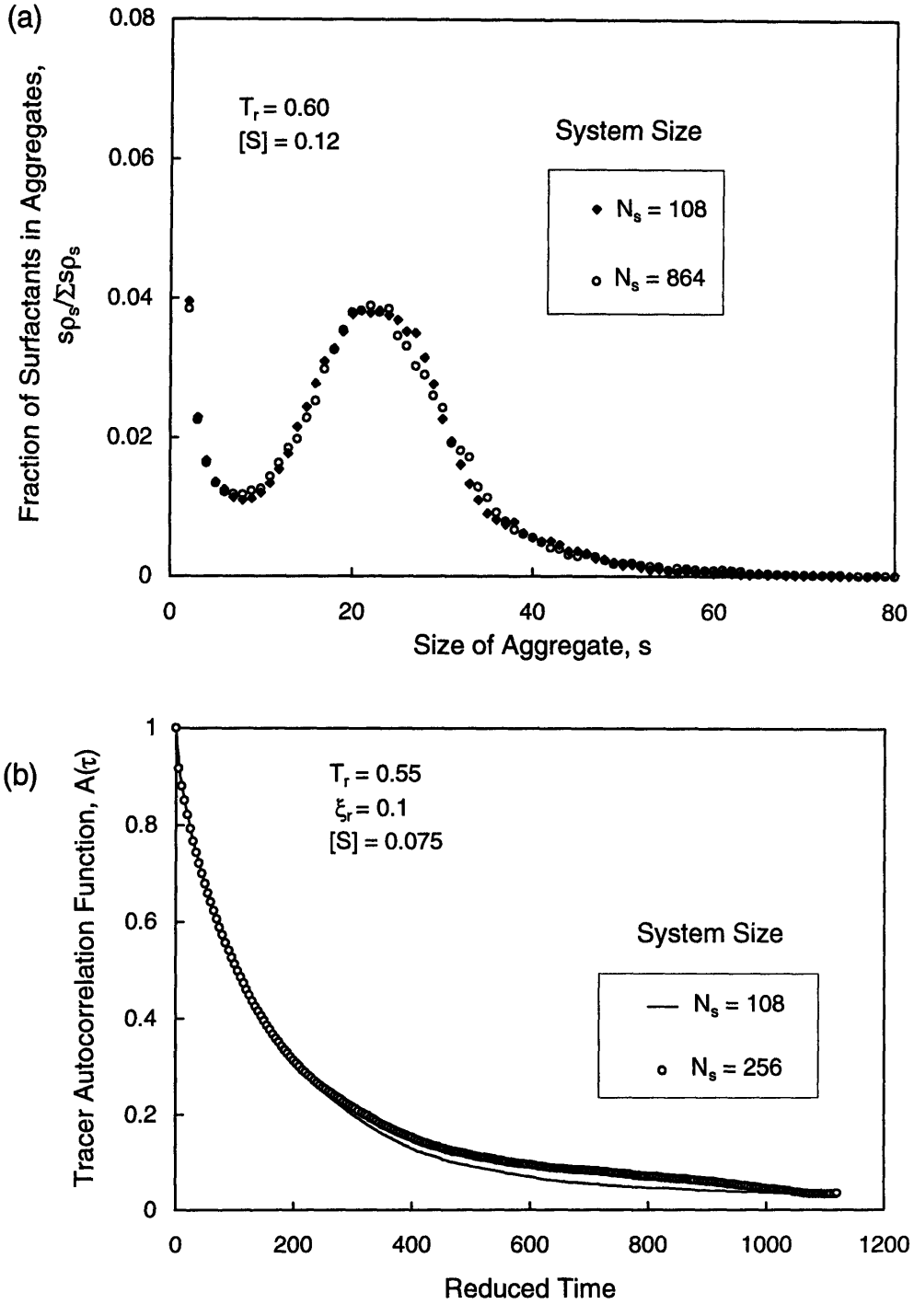

Figure 4-6: Effect of system size on (a) micelle size distribution at $[S] = 0.12$, $T_r = 0.60$ and (b) on the tracer autocorrelation function at $T_r = 0.55$, $[S] = 0.075$

responsible for asphericity in this range. Micelles with aggregation numbers outside the 10 - 35 range are highly aspherical, but are limited to aspect ratios of less than 4. At large aggregation numbers, poor sampling is evident since these micelles occur very infrequently.

Figure 4-7b shows the spherically averaged radial distribution function through a micelle with aggregation number of 30. The micelle is found to be composed of a dense hydrophobic core (with number density ≈ 0.78) surrounded by a less well defined corona of the hydrophilic headgroups. The corona region is considerably hydrated (≈ 55 % solvent). Had the micelle been rod-like, long tails in the head and tail group distributions would have been expected. In this work, such tails were found to occur only for aggregation numbers > 40.

4.2.2 Effect of Excluded Volume on Free Surfactant Concentration

At surfactant concentrations well above the cmc there is a drop in [F] (Figure 4-1), which has also been observed in simulations by Adriani *et al.* [14] and Desplat and Care [15]. Experimental evidence also exists for this decrease [16] which is not predicted by traditional theories [5, 6, 7, 8] for micelle formation. As noted by Adriani *et al.* [14], an exception is the Leibler *et al.* theory [17] which can predict a decrease in $[F]$ since the entropy of mixing of the free surfactant molecules is based on the solvent volume and not on the solution volume. Leibler's theory suggests that excluded volume effects introduce non-ideal behavior at high $[S]$ and that the accessible volume is considerably reduced from the total solution volume. Desplat and Care [15] introduced an activity coefficient (γ) to account for these non-idealities, postulating $\ln(\gamma)$ to be proportional to the total amphiphile concentration, but independent of the aggregate size or shape.

An alternative approach is employed in this work in which the activity coefficient is calculated on the basis of a virial expansion [18]. The advantage of this approach is that the physical significance of the activity coefficient and its dependence on aggregate size becomes clear. By equating the chemical potential of a free surfactant molecule to that of a surfactant molecule in an aggregate of size s, accounting for the translation entropy using an ideal gas model, and incorporating deviations from the ideal gas model into an activity

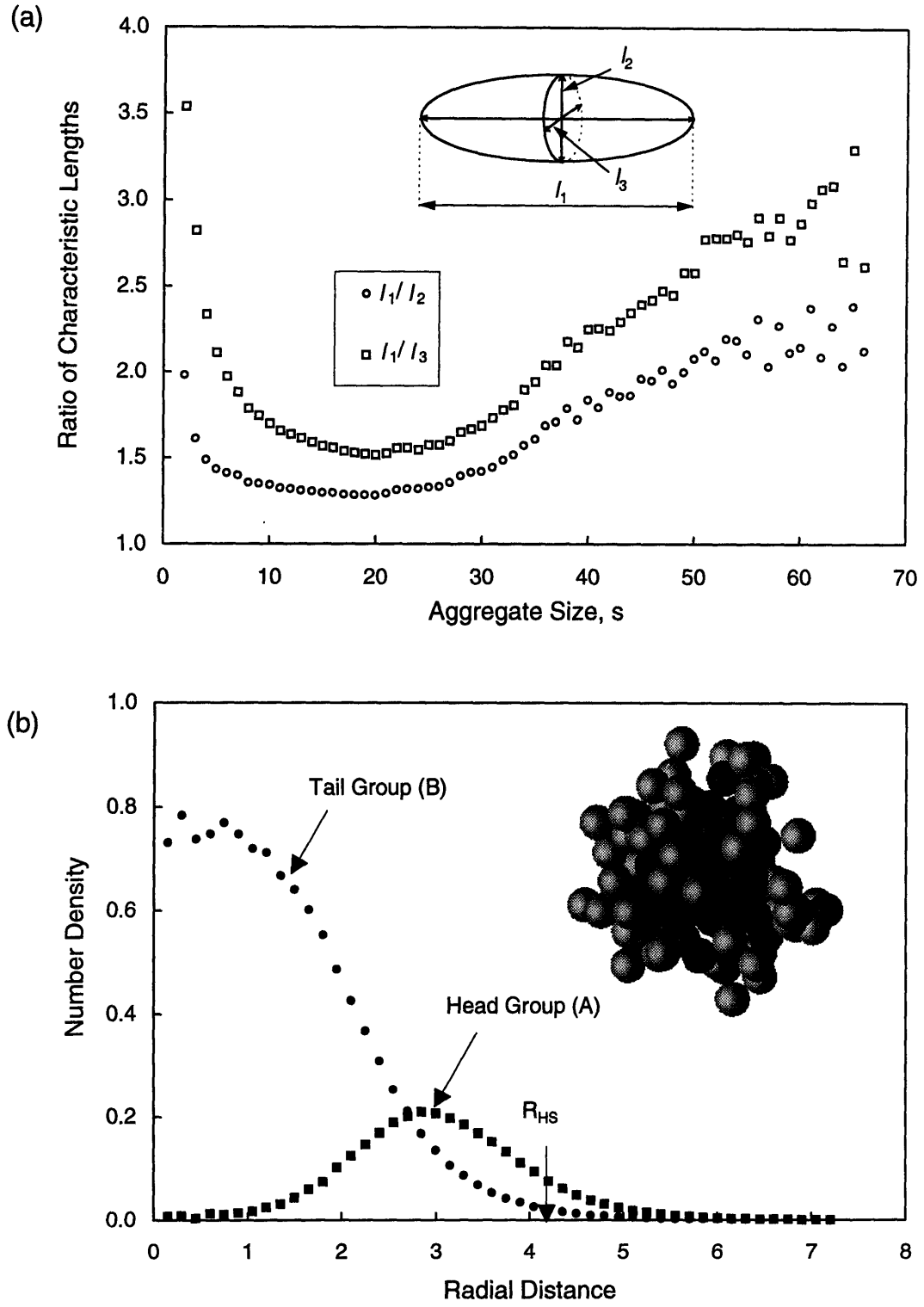

Figure 4-7: (a) Ratio of characteristic lengths as a function of aggregate size (T_r = 0.60, $[S] = 0.12$), (b) Spherically averaged radial distribution function through micelle with aggregation number s = 30. Inset : Snapshot of micelle (s=30), dark beads represent tail groups.

coefficient, one can obtain for the aggregate size distribution [19, 20]

$$\rho_s = \rho_1^s \frac{\gamma_1^s}{\gamma_s} exp\left(\frac{-s(\mu_s^o - \mu_1^o)}{kT}\right) \tag{4.6}$$

where ρ_s and γ_s are the number density and activity coefficient, respectively of an aggregate of size s and μ_s^o is the chemical potential of a single surfactant molecule in an aggregate of size s in the dilute reference state (T, P, $\sum_s \rho_s \rightarrow 0$). If only the excluded volume effects between micelles are considered and if only the second virial term is retained in a virial expansion, the activity coefficient can be shown to be [18, 19] :

$$\ln(\gamma_s) = -\sum_r \beta_1(s,r)\rho_r \tag{4.7}$$

where $-\beta_1(s,r)$ is the volume excluded to aggregates of size s due to the presence of aggregates of size r and is related to an interaction potential ($u_{s,r}$) between aggregates of size s and r by:

$$-\beta_1(s,r) = -\frac{1}{V}\int \left[exp(-\frac{u_{s,r}}{kT}) - 1\right] d\mathbf{q}_r d\mathbf{q}_s \tag{4.8}$$

where $\mathbf{q}_r$ and $\mathbf{q}_s$ are the coordinate vectors of aggregate r and s respectively.

As $\sum_r \rho_r \rightarrow 0$, $\gamma_s \rightarrow 1$, and the non-interacting result is recovered. This approach is entirely analogous to that used in incorporating excluded volume effects to describe real fluids, which yields the very successful van der Waals equation of state.

It is our goal to calculate the activity coefficients from simulation data using Eq. 4.7 at a particular concentration ($[S] = 0.12$) and then to extract the reference state chemical potentials (μ_s^o) from the simulated size distribution using Eq. 4.6. The μ_s^o are independent of concentration, and hence we should be in a position to predict both the size distributions and $[F]$ for any $[S]$ using the data calculated at $[S] = 0.12$. The ability to predict properties at other concentrations would strongly suggest that excluded volume effects are in fact responsible for the observed deviations. Desplat and Care [15], in contrast, used simulation information over the entire concentration range to extract the activity coefficient. In order to calculate the activity coefficient by using Eq. 4.7, the size distribution (ρ_s) and structure of aggregates are required. The size distribution for $[S] = 0.12$, $T_r = 0.60$ is shown in Figure 4-5a.

If it is assumed that the aggregates are spherical in shape, a hard sphere radius may be

defined as the radius that includes 90 % of all beads within an aggregate. This information may be obtained from the radial distribution profile (Figure 4-7b). For spherical micelles, $R_s \propto s^{\frac{1}{3}}$, where the proportionality constant may be directly obtained from simulation data. Figure 4-8a shows a plot of the the effective hard sphere radius versus $s^{\frac{1}{3}}$, where the transition from spherical to cylindrical micelles manifests itself as a sharp change in the slope of the curve. For aggregation numbers less than 35, the aggregates are almost spherical as discussed earlier. Above 35, the aggregates are cylindrical in shape. These cylindrical micelles are ill defined and comprise two spherical micelles which are in close contact. Therefore the slope in Figure 4-8a more than doubles as one enters the cylindrical region. Figure 4-8b shows the bead distribution projected onto the major principal axis for an aggregate of size 41. Only beads within a distance of 0.75σ from the major principal axis are included in this distribution. Close to the center of the aggregate, a marked decrease in the hydrophobic chain density is observed at the point of contact between the two aggregates. Also evident is the presence of A beads near the center of the aggregate. Sampling statistics are poor since these aggregates occur infrequently. By requiring 90 % of the beads to be within R_{HS}, the aspherical nature of the aggregate is emphasized. Hence an alternative definition of an effective hard sphere radius was employed based on the radius at which the total spherically-averaged bead number density equals 0.12 (equal to [S]). The latter approach has the advantage that no transition in R_{HS} is observed (Figure 4-8a) since the bead contribution is weighted by r^{-2}, where r is distance from the center of mass. The volume occupied by a surfactant is slightly larger for higher aggregation numbers, as reflected in the negative intercept of 0.1 in Figure 4-8a.

To simplify the analysis, the excluded volume of the cylindrical micelles is assumed to be equivalent to a hypothetical spherical micelle of the same aggregation number, obtained by extrapolating the results for the spherical micelles to higher aggregation numbers. The excluded volume of the cylindrical micelles is thus underestimated, but as they are few in number their contribution is small, and the error associated with this assumption is not significant. Similarly the free surfactant effective hard sphere radius was calculated by extrapolation to an aggregation number of 1.

For interaction between hard spheres, the excluded volume may be obtained from Eq. 4.8 as

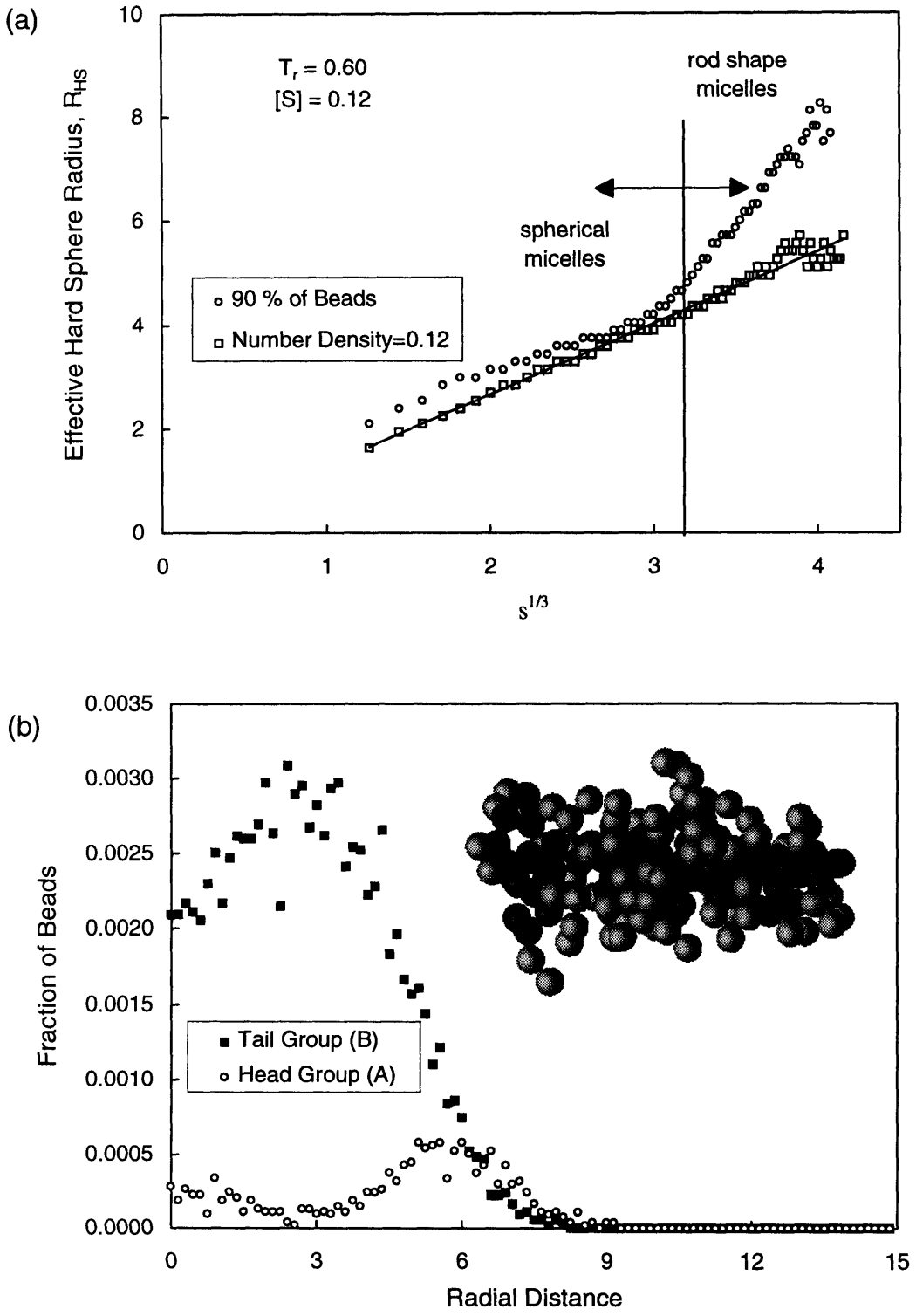

Figure 4-8: (a) Variation of R_{HS} with aggregation number ($T_r = 0.60, [S] = 0.12$), (b) Bead distribution projected onto the major principal axis for micelle with s = 41. Inset : Snapshot of micelle (s=41) showing rather loose and elongated structure.

$$-\beta_1(s,r) = \frac{4\pi}{3}(R_r + R_s)^3 \tag{4.9}$$

R_r and R_s are the hard sphere radii of aggregates of size r and s respectively, as depicted in Figure 4-8a. By using the size distribution (ρ_s) and hard sphere radius of micelles (R_s) generated from the computer simulations we calculated the activity coefficients (γ_s) using Eq. 4.7. Using Eq. 4.6, one can extract from the simulated size distribution the difference in chemical potential per molecule $(\mu_s^o - \mu_1^o)/kT$ as reported in Figure 4-9. The chemical potential difference is, as noted by Desplat and Care [15], a monotonically decreasing function in s, although in our work the decline is less pronounced. Direct comparison is difficult since they employ an amphiphile of form AB_3 and include attractive head-solvent interactions.

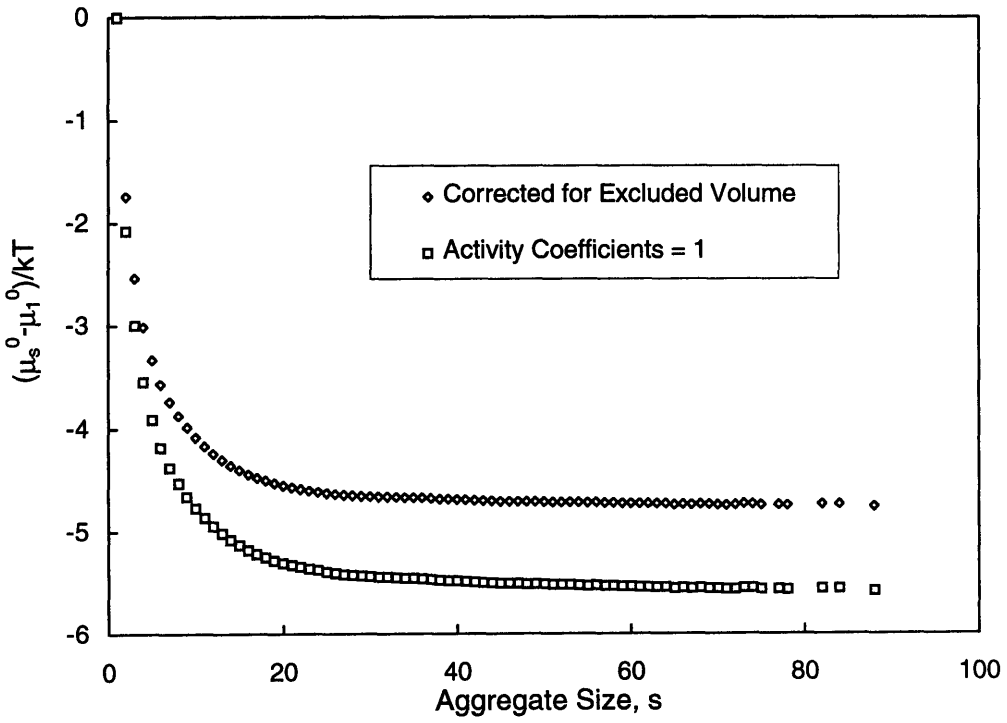

Figure 4-9: Difference in chemical potential per surfactant molecule in a micelle of size s and a free surfactant molecule,$(\mu_s^o - \mu_1^o)/kT$, at $T_r = 0.60, [S] = 0.12$.

It should be noted that incorporation of excluded volume effects serves to lower the absolute magnitude of the extracted reference state chemical potential difference, from which it can be concluded that the observed excluded volume effects favor the formation

of larger aggregates. The ratio of the volume excluded to a free monomer due to the presence of 30 free surfactants to that excluded to a monomer by an aggregate of size 30 is approximately:

$$\left.\frac{30(1+1)^3}{(1+s^{+\frac{1}{3}})^3}\right|_{s=30} \sim 3.5$$

Larger aggregates are therefore favored since they serve to reduce the total excluded volume, but this is at the expense of considerable translational entropy.

The excluded volume contribution to the chemical potential difference is

$$\ln(\gamma_1) - \frac{\ln(\gamma_s)}{s}$$

For large s, the excluded volume contribution is predominantly determined by the first term. However, for intermediate values of s, which correspond to the observed micelle size, the contribution from the γ_s term is significant. It is therefore imperative that the size dependency of γ_s be taken into account correctly.

To quantify the size of the virial term, it is instructive to compare the contributions of the excluded volume effect and of the translational entropy to the Gibbs free energy of an aggregate of size s. The ratio is simply

$$\eta(s) = |\frac{\ln(\gamma_s)}{\ln(\rho_s)}| \times 100\% \tag{4.10}$$

and is shown in Figure 4-10a. For small aggregate sizes, the excluded volume term contributes less than 10 %, increasing to around 30 % for $s > 60$. Higher order virial terms are expected to play a role for large aggregates. However, since these aggregates occur so infrequently this correction was not incorporated.

Figure 4-10b shows the fractional contribution of the excluded volume terms to $\ln(\gamma_s)$ for $s = 1$ and $s = 25$. The fractional contribution, $\mathcal{F}(s,r)$, is defined as

$$\mathcal{F}(s,r) = \frac{\beta_1(s,r)\rho_r}{\sum_i \beta_1(s,i)\rho_i} \tag{4.11}$$

The free surfactants (r=1), contribute significantly to the activity coefficients. For s=1, $\mathcal{F}(1,1) \approx 0.25$ due to the high number density of free surfactants. As is evident from Figure 4-10b, the free surfactant contribution becomes more significant at larger s ($\mathcal{F}(25,1) \approx$

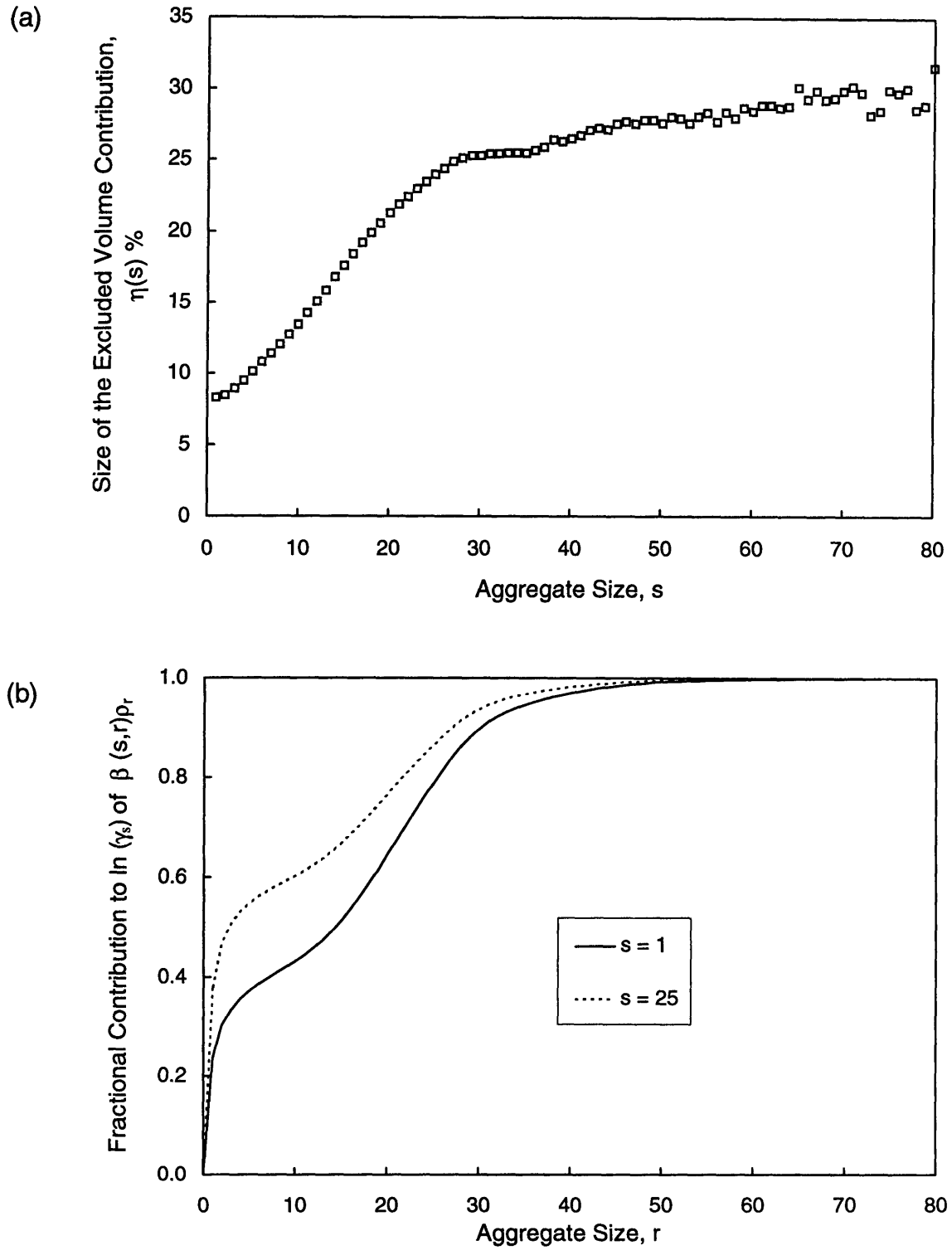

Figure 4-10: (a) Contribution of virial term to translational component of Gibbs free energy as a function of aggregate size, (b) Fractional contribution of aggregates of size r to the total excluded volume for $s = 1$ and $s = 25$ as defined by Eq. 4.11

0.4). Pre-micelles (aggregation numbers 5 - 15) contribute significantly less than the free surfactants despite their large volumes owing to their low number density as indicated by the shoulder in Figure 4-10b. Aggregates with $r > 40$ contribute less than 5 % towards $\ln(\gamma_s)$ and thus the error introduced by assuming that the larger aggregates are spherical should be minimal.

Since values of $(\mu_s^o - \mu_1^o)/kT$ are based on an infinitely dilute reference state, they are applicable at other concentrations. We are thus in a position to predict both the size distributions and [F] for any [S] using the data calculated at [S]=0.12. This involves solving the set of equations (Eq. 4.6) for ρ_r subject to the requirement that $\sum_r r\rho_r = [S]/N_b$. Shown in Figure 4-11a is a comparison of the simulated data to those predicted using Eq. 4.6, where the agreement is seen to be excellent over the entire concentration range. Excluded volume effects thus appear to be responsible for the reduction in $[F]$ with increasing total surfactant concentration. The activity coefficient may be included in the definition of a new concentration variable $[F]^* = \gamma_1[F]$ which behaves in line with traditional theories. Physically $[F]^*$ is the free surfactant concentration based on the accessible volume. Figure 4-11b shows the predicted size distributions. For [S]=0.12 the agreement is exact since we have extracted all our information at this concentration. The predictions at [S]=0.02 and [S]=0.065 correspond closely to the simulated data, and therefore support the interpretation in terms of excluded volume.

The standard state chemical potential difference, $(\mu_s^o - \mu_1^o)/kT$, and the excluded volume terms, $\beta_1(r,s)$, are expected to be functions of temperature. Extrapolation from the information obtained at $T_r = 0.60$ to other temperatures requires knowledge of this functional dependence on T and therefore has not been performed. The approach described in this chapter, has, however, been employed equally successfully at the other temperatures.

4.3 Conclusion

Stochastic Dynamics simulations have been employed to investigate the self-assembly of model amphiphiles A_2B_2. The effect of temperature and surfactant concentration on the micelle size distribution was obtained. The micelle shape was quantified using the eigenvalues of the moment of inertia matrix and the spherically averaged radial distribution function. A drop in free surfactant concentration observed at high total surfactant concen-

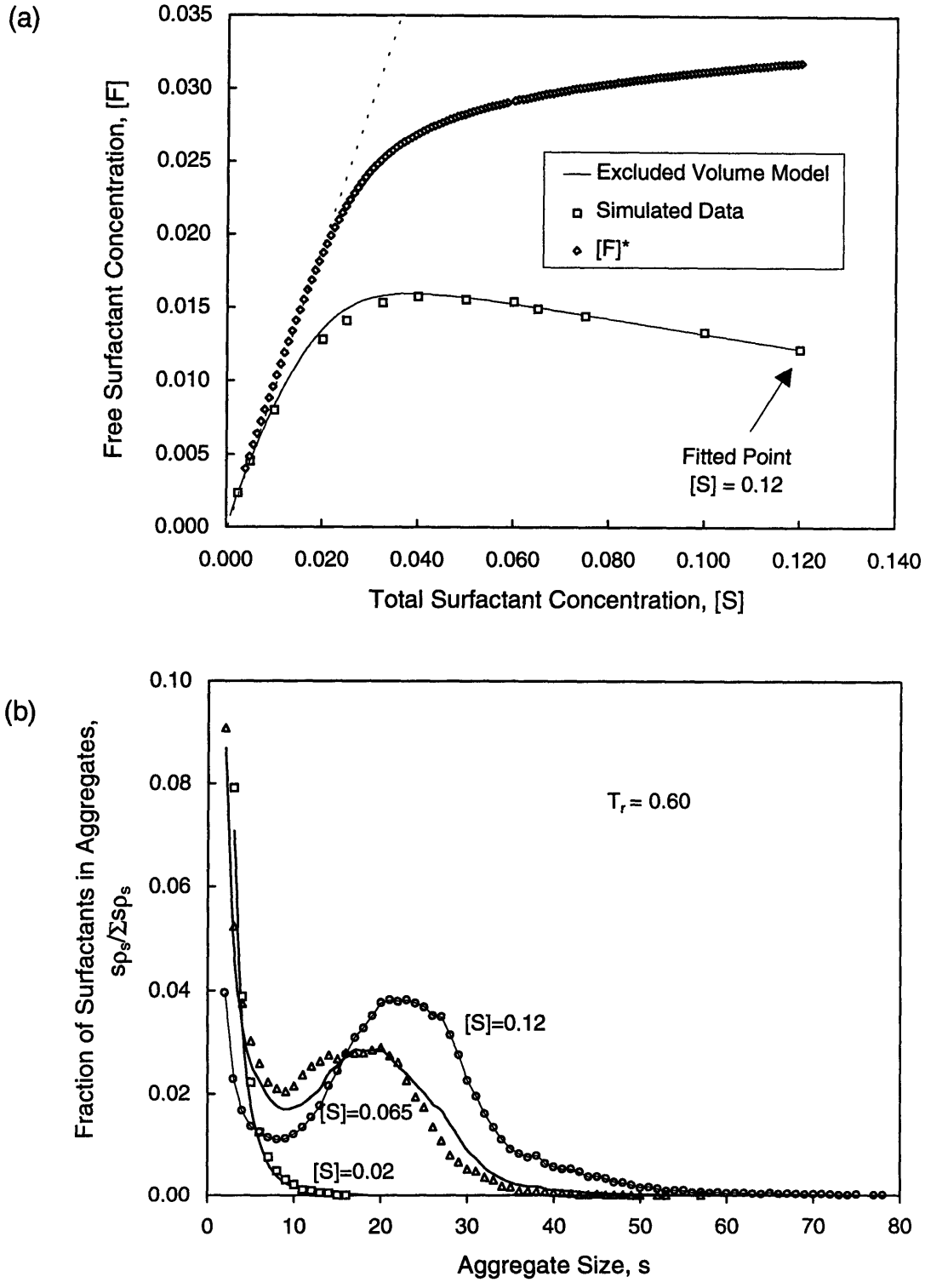

Figure 4-11: Comparison of theoretical predictions to simulation data (a) Free surfactant concentration ([F]) as a function of total surfactant concentration ([S]) (b) Size distributions at different total surfactant concentration ([S]).

tration was attributed to excluded volume effects and taken into account using a second virial coefficient. In contrast to the approach of Desplat and Care [15], the dependency of the activity coefficient,γ_s, on aggregate size was also taken into account, and shown to be important for intermediate aggregation numbers. Excellent agreement was obtained between the simulated results and the predictions based on the excluded volume approach over the entire concentration range. We have demonstrated that Stochastic Dynamics simulations provide a computationally efficient means of investigating the self-assembly process of small model amphiphiles.

Chapter 5 will be directed towards understanding the dynamics of self-assembly in this model system (A_2B_2) and Chapter 6 deals with incorporating the effect of solvent structure through a potential of mean force.

Bibliography

[1] J.-P. Ryckaert, G. Ciccotti, and H. J. C. Berendsen, J. Comp. Phys. **23,** 327 (1977).

[2] W. F. van Gunsteren and H. J. C. Berendsen, In *NATO Advance Science Institute Series. The Physics of Superionic Conductors and Electrode Materials*, edited by J. W. Perram, (Plenum Press, New York, 1980), p. 221.

[3] B. Smit, P. A. J. Hilbers, K. Esselink, L. A. M. Rupert, and N. M. van Os, J. Phys. Chem. **95,** 6361 (1991).

[4] G. Bossis, B. Quentrec, and J. P. Boon, Molecular Physics **45,** 191 (1982).

[5] C. Tanford, *The Hydrophobic Effect*, (Wiley, New York, 1980).

[6] J. Israelachvili, *Intermolecular and Surface Forces*, (Academic Press, London, 1991).

[7] R. E. Goldstein, J. Chem. Phys. **84,** 3367 (1986).

[8] R. J. Hunter, *Foundations of Colloid Science Vol. 1*, (Oxford Science Publications, 1991).

[9] T. Haliloğlu and W. L. Mattice, Chem. Eng. Sci. **49,** 2851 (1994).

[10] R. G. Larson, J. Chem. Phys. **89,** 1642 (1988).

[11] R. G. Larson, J. Chem. Phys. **96,** 7904 (1992).

[12] A. D. Mackie, K. Onur, and A. Z. Panagiotopolous, J. Chem. Phys. **104,** 3718 (1996).

[13] M. P. Allen and D. J. Tildesley, *Computer Simulations of Liquids*, (Oxford Science Publications, Oxford Press, 1992).

[14] P. Adriani, Y. Wang, and W. L. Mattice, J. Chem. Phys. **100,** 7718 (1994).

[15] J.-C. Desplat and C. M. Care, Molec. Phys. **87,** 441 (1996).

[16] I. Johnson, G. Olofsson, and B. Jönsson, J. Chem. Soc., Faraday Trans. 1 **83,** 3331 (1987).

[17] L. Leibler, H. Orland, and J. C. Wheeler, J. Chem. Phys. **79,** 3550 (1983).

[18] L. Onsager, Ann. N.Y. Acad. Sci. **51,** 627 (1949).

[19] A. Ben-Shaul and W. M. Gelbart, J. Phys. Chem. **86,** 316 (1982).

[20] H. Wennerström and B. Lindman, Physics Reports **52,** 1 (1979).

Chapter 5

Dynamics of Self-Assembled Surfactant Systems

5.1 Introduction

In Chapter 4 we demonstrated the ability to determine the equilibrium properties of a model amphiphile system of type A_2B_2 using stochastic dynamics simulations. In this chapter we wish to look at the dynamic processes involved in micellar systems, in particular the exit and entry rates of surfactants into micelles and the response of the system to a temperature perturbation.

Temperature, pressure, and concentration jump experiments have long been employed by experimentalists to elucidate the dynamic phenomena in micelle solutions [1]. A perturbation is introduced, and the response of the system is monitored, typically using light scattering or absorbance. The general consensus is that there are two relaxation processes - a fast step associated with the exchange of surfactants between the bulk and micellar phases (nano-microsecond time range), and a second slower process associated with the break-up (dissolution) or formation of new micelles (micro-milliseconds). In ionic systems, an extremely fast process is sometimes observed and is ascribed to the rearrangement of counterions [2, 3]. The theoretical basis for understanding the kinetics of micellar equilibria was provided by Aniansson and Wall [4] (AW) and extensions have been provided by Kahlweit [5] to include the prediction of the observed amplitudes. Excellent agreement is found between the experimental results and theoretical fits [1, 6]. The effect of micelle

coalescence/fission in non-ionic surfactant systems (or at high salt concentrations in ionic systems), originally neglected by AW, has been addressed by Kahlweit [7]. An estimate of the exit rate kinetics from diblock copolymer micelles based on Kramers [8] rate theory was developed by Halperin and Alexander [9]. They also demonstrated that the AW mechanisms would be dominant for such micelles by calculating the barrier free energies for micelle coalescence and fission. Notably, micelle coalescence is energetically unfavourable owing to steric interactions between the corona chains. Steric hindrance is less pronounced for short chains. Scaling theory, which is valid only for long chains, is employed to calculate the free energy of the micelle making, direct comparison to our results for short chains difficult and at best approximate.

The use of molecular level simulations to investigate the dynamics of self-assembly has been limited owing to the complexity of the problem. Haliloğlu and Mattice [10] defined a number of correlation functions to demonstrate that the dynamics for the interchange of chains could be probed in Monte Carlo (MC) simulations. By tagging chains in a specific aggregate they calculated correlation times for chain extraction, chain addition, and chain redistribution in micelles formed by the diblock copolymer $A_{10}B_{10}$. The exit rate was found to be independent of concentration while the entry rates were decomposed into contributions from micelle-micelle coalescence and individual monomer insertion. An analogous approach is employed in this work to extract dynamic information. In addition we also probe the effect of temperature on the observed rate and extract information about the size of the energy barrier for chain extraction from a micelle. More importantly, we relate the observed rate constants to those in the AW mechanism and thereby predict the response of the system to perturbations.

Stochastic dynamics (SD) simulations have been used to investigate the dynamics associated with the gauche-trans dihedral transitions in butane, decane and heptane [11, 12]. The results were compared to theoretical descriptions of rate processes (e.g. transition state theory [13], Kramers rate theory [8] and modifications thereof) and to molecular dynamics simulations (MD) of the system including the solvent. The Langevin equation has also been employed along a reaction coordinate in an attempt to determine reaction rates. Recent examples include n-butane isomerization [14] and a particle in a cubic potential [15]. The common feature in past work was that the form of the energy barrier was known, and hence the theoretical approaches could be evaluated by direct comparison to the simulation data.

In contrast, no *a priori* knowledge is available about the energy barriers in the micellar system.

The calculation of the frictional coefficient for atoms in polymer chains was addressed by Pastor and Karplus [16]. A methodology based on the accessible surface area exposed by the components of the polymer chain was used to estimate the component's frictional coefficient. The success of this approach was evaluated by comparing the calculated rotational and translational diffusivity to experimental data. Brownian dynamics, in which the inertial terms are neglected, have been employed to determine the bending and twisting dynamics of short linear DNA chains [17]. SD has also been used to investigate dynamic behaviour in n-nonane [18] and 1-decanol [19].

The simulation algorithm is as described in Chapter 3 and the equilibrium properties at three reduced temperatures were determined in Chapter 4. The work falls into two categories. Firstly we attempt to determine the exit and entry rate constants associated with surfactant insertion and extraction and then we investigate the response of the system to a perturbation in temperature.

5.2 Micellar Dynamics

The exchange of monomers between the bulk solution and micelles may be represented by the reaction

$$A_1 + A_{i-1} \underset{k_i^-}{\overset{k_i^+}{\rightleftharpoons}} A_i \tag{5.1}$$

where A_i denotes aggregates with aggregation number i and k_i^+,k_i^- are the association and dissociation rate constants, respectively. The monomer is represented by A_1 in this notation and the concentration of aggregates of size i is $[A_i]$ (equivalent to ρ_i used in Chapter 4). The rate constants are expected to be a function of the aggregate size i.

In Chapter 4 we demonstrated that the standard state free energy difference, $(\mu_i^o - \mu_1^o)/kT$, was constant for $i > 20$. Therefore $\mu_i^o \approx \mu_{i-1}^o$ = constant for $i > 20$. The equilibrium constant may be related to the free energy of formation and by neglecting non-idealities to the micelle concentrations.

$$K_{eq,i} = \frac{k_i^+}{k_i^-} = \frac{[A_i]}{[A_1][A_{i-1}]} \approx e^{-(\mu_i^o - \mu_1^o)/kT} \tag{5.2}$$

The final term is a direct result of the constancy of μ_i^o, i.e. $i\mu_i^o - (i-1)\mu_{i-1}^o - \mu_1^o \approx \mu_i^o - \mu_1^o$. Therefore, for values of $i > 20$, the equilibrium constant $K_{eq,i}$ may be considered to be nearly independent of i. Aniansson and Wall [4], in their theory dealing with kinetics of self-assembly, extended these arguments to infer the invariance of k_i^- in the micelle region. The improbability of both k_i^- and k_i^+ varying significantly and in a compensating manner to ensure the constancy of $K_{eq,i}$ was used to infer the relative constancy of k_i^-. This was done in order to solve the flux equations analytically for the short time behavior.

An alternative representation of micelle equilibria to that shown in Eq. 5.1 is

$$iA_1 \underset{\kappa_i^-}{\overset{\kappa_i^+}{\rightleftharpoons}} A_i \tag{5.3}$$

and the resulting equilibrium constant can be related to $K_{eq,i}$ via

$$\kappa_{eq,i} = \frac{[A_i]}{[A_1]^i} = \prod_2^i K_{eq,i} = e^{-i(\mu_i^o - \mu_1^o)/kT} \tag{5.4}$$

Therefore, even small variations in $K_{eq,i}$ can result in the observed size distribution, since the size distribution results from a product $\prod_2^i K_{eq,i}$.

Two approaches were adopted in an attempt to determine the association (k_i^+) and dissociation (k_i^-) rate constants directly from simulation data. The first involved tagging surfactant molecules in aggregates and then monitoring how long it takes for them to re-distribute among aggregates and the free surfactant pool. The second approach involved calculating the free energy profile for the extraction of a surfactant chain from an aggregate and using Kramers' rate theory and transition state theory to calculate the exit rate.

5.2.1 Exit and Redistribution Rates

The average exit rate constant was determined by tagging all surfactants in aggregates at $t = 0$. The system was then monitored as a function of time. If a surfactant chain left an aggregate (i.e. was no longer within the cut-off distance used to define the aggregate) the chain was detagged. A function $C(t)$ was defined as

$$C(t) = < \frac{N(t)}{N(0)} > \tag{5.5}$$

where $N(t)$ is the number of chains still tagged at time t. The angular brackets indicate an average over multiple time origins. Note that surfactants in all aggregates are initially tagged. The contribution of aggregates in the size range $5 - 20$ is expected to be small, since the number density of these aggregates is very low. Smaller aggregates ($n < 5$) may contribute to the short time behaviour of $C(t)$ and this will manifest itself as an initial rapid decline.

The function $N(t)$ is expected to behave as a first order process, since once a surfactant is detagged it will remain detagged for the remainder of the simulation and therefore a tagged surfactant cannot re-enter a micelle

$$\frac{dN(t)}{dt} = -K^{-}N(t) \tag{5.6}$$

which yields and exponential form for $C(t)$

$$C(t) = e^{-K^{-}t} \tag{5.7}$$

It is important to realise that the exit rate defined above, K^{-}, is related non-trivially to the dissociation rate, k_i^{-}, defined in Eq. 5.1.

Figure 5-1 shows the function $C(t)$ at four temperatures at a total surfactant concentration of [S]=0.12. At the lowest temperature, the exit rate is slow and less than 20 % of the initially tagged surfactants have left the micelle phase after $t = 500$. The exponential behaviour of $C(t)$ is evident at higher temperatures and from the linear nature of the plots of $\ln C(t)$ versus time in Figure 5-2. The small deviation from the exponential behaviour at short times may be ascribed to the contributions of small labile aggregates that form and break-up easily, as was confirmed by tagging aggregates in a particular size range (e.g. aggregation numbers from 25 to 35) and then calculating $C(t)$. The long time tails of $\ln C(t)$ calculated on the aggregate subset $\{i\} = \{25, 35\}$ were found to be parallel to those calculated on the entire aggregate interval $\{2, \infty\}$.

The effect of varying the frictional coefficient (at T_r=0.60) on the correlation function is shown in Figure 5-3 and is found to be marked at high values (e.g. change from $\xi_r = 1$ to $\xi_r = 10$). In contrast, only a small change is observed when changing from $\xi_r = 1$ to $\xi_r = 0.1$. An analogous set of results at T_r=0.55 is shown in Figure 5-4.

The exit rate constant K^{-} was extracted at each temperature and found to obey an

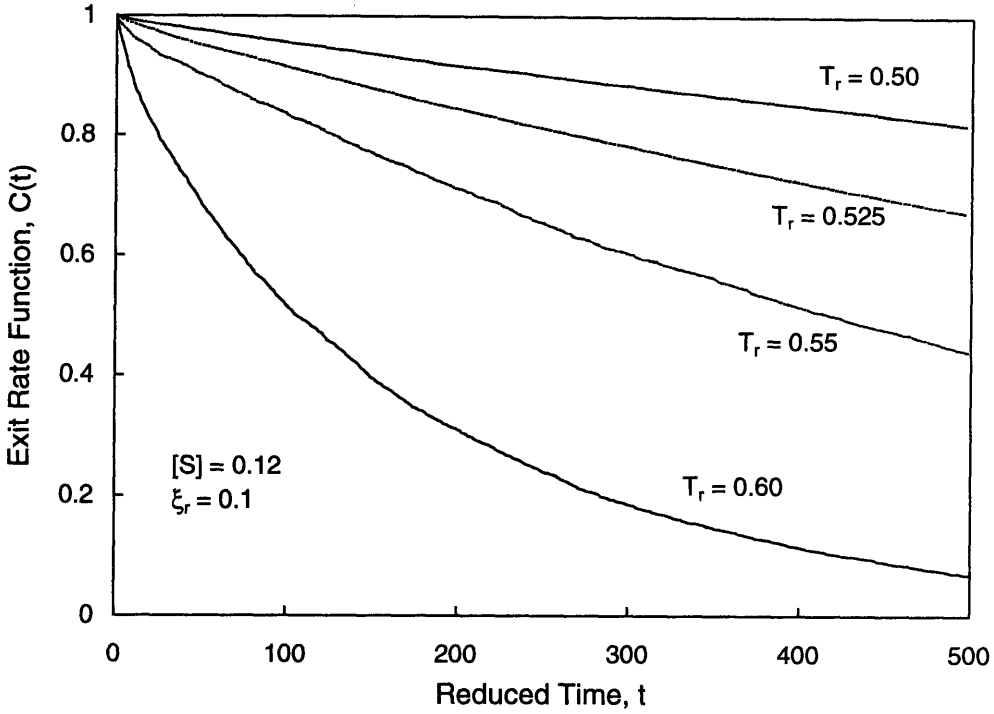

Figure 5-1: Effect of temperature on the rate at which tagged chains leave the micelle phase.

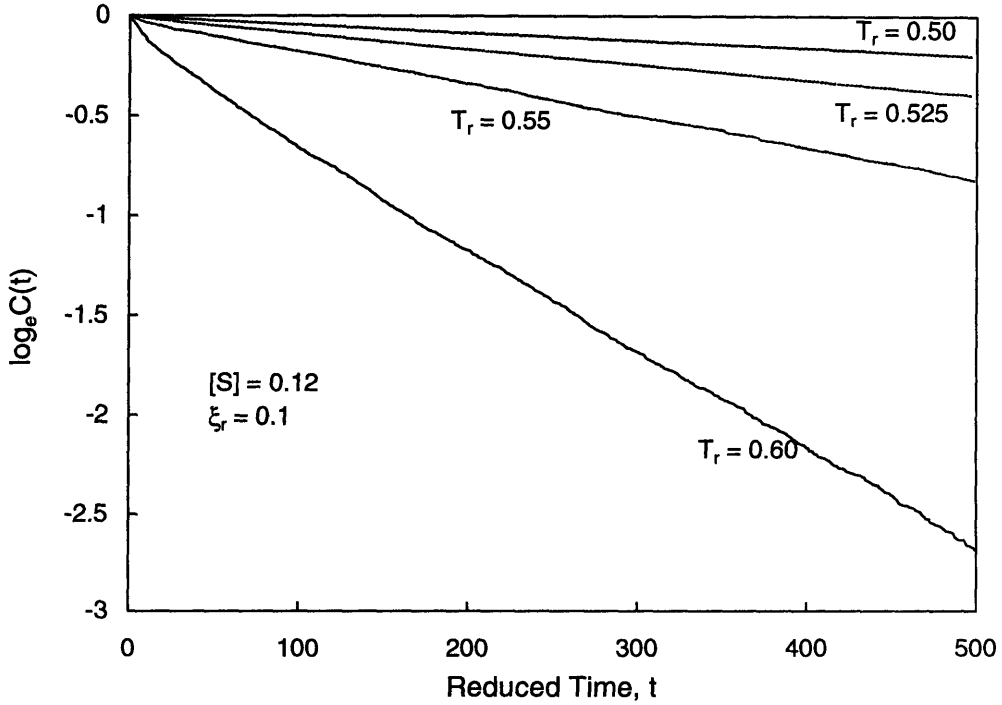

Figure 5-2: The exponential behaviour of $C(t)$ is clearly evident from the linear nature of the plots of $\ln C(t)$ versus reduced time (t). The exit rates K^- at different temperatures were extracted from these plots.

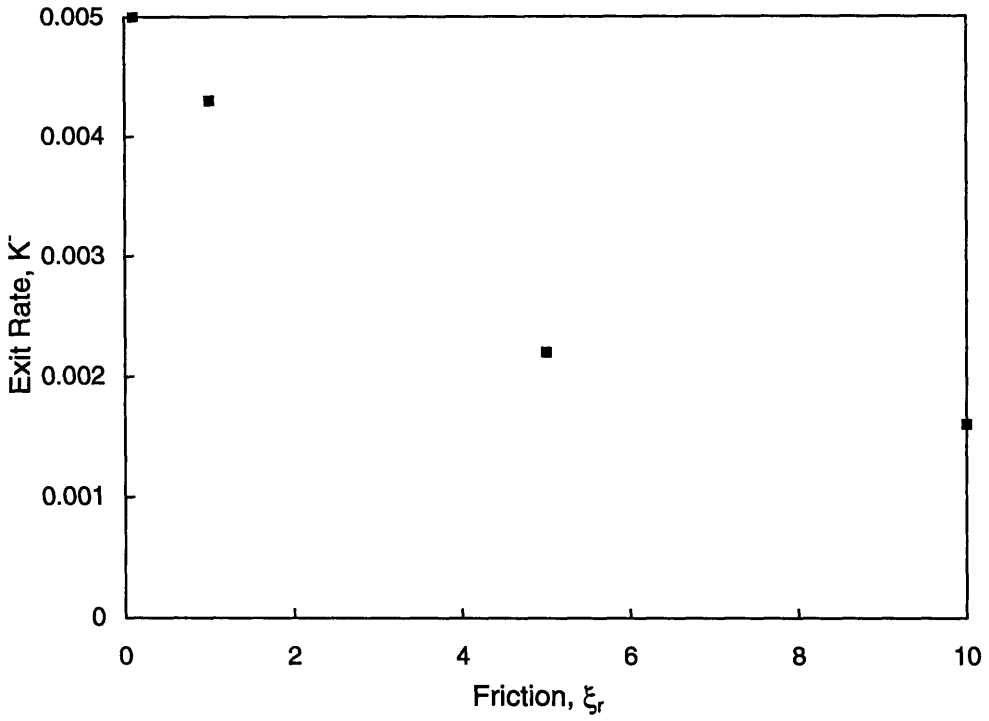

Figure 5-3: Variation of exit rate as a function of the frictional coefficient ξ_r at T_r=0.60, [S]=0.12

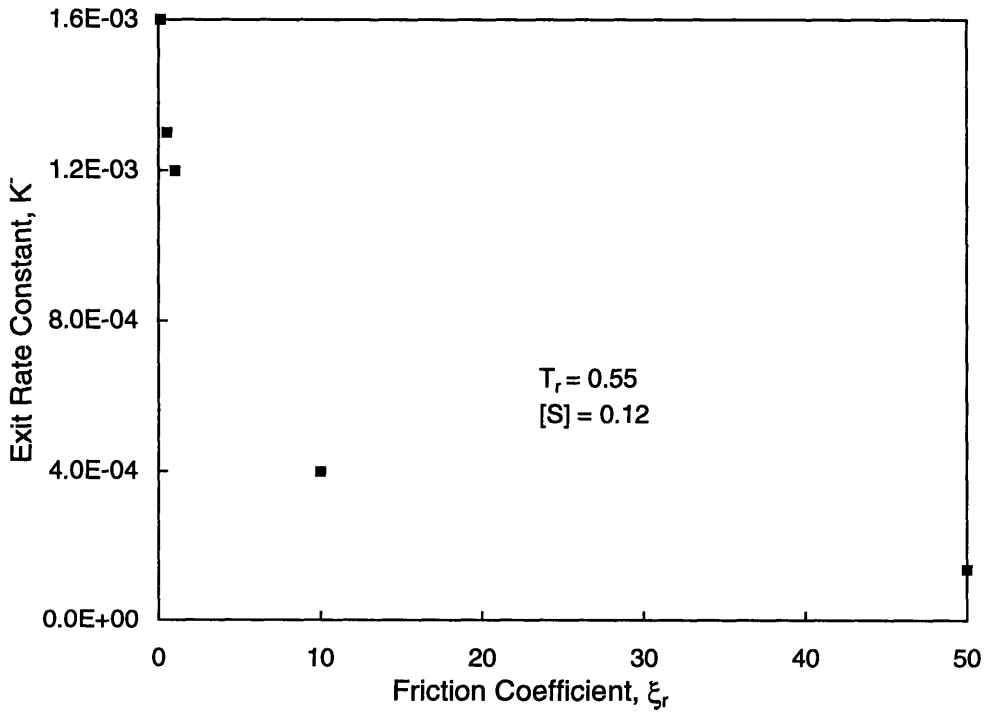

Figure 5-4: Variation of exit rate as a function of the frictional coefficient ξ_r at T_r=0.55, [S]=0.12

Arrhenius expression

$$K^- = K_o^- e^{-E^*/kT} \tag{5.8}$$

with an activation barrier energy of E^*, as shown by the linear plots in Figure 5-5. The assumption that E^* is independent of temperature is based on the premise that the activation energy is far larger than the thermal energy (i.e. a high barrier). The fact that the extracted free energy difference ($(\mu_i^o - \mu_1^o)$ obtained in Chapter 4 is order 5 kT and is only weakly temperature dependent provides further support for this assumption. From the slope and intercept on Figure 5-5, we obtained $E^* = 7.6$ and $K_o = 1800$ for $\xi_r = 0.1$. The activation energy should be independent of the choice of ξ_r. Figure 5-5 includes an Arrhenius plot for $\xi_r = 10$, yielding an activation energy of 8.1 (6 % deviation from result at $\xi_r = 0.1$). The pre-exponential term does depend on ξ_r. Insufficient data exist for analysing the functional dependence of the pre-exponential factor on ξ_r.

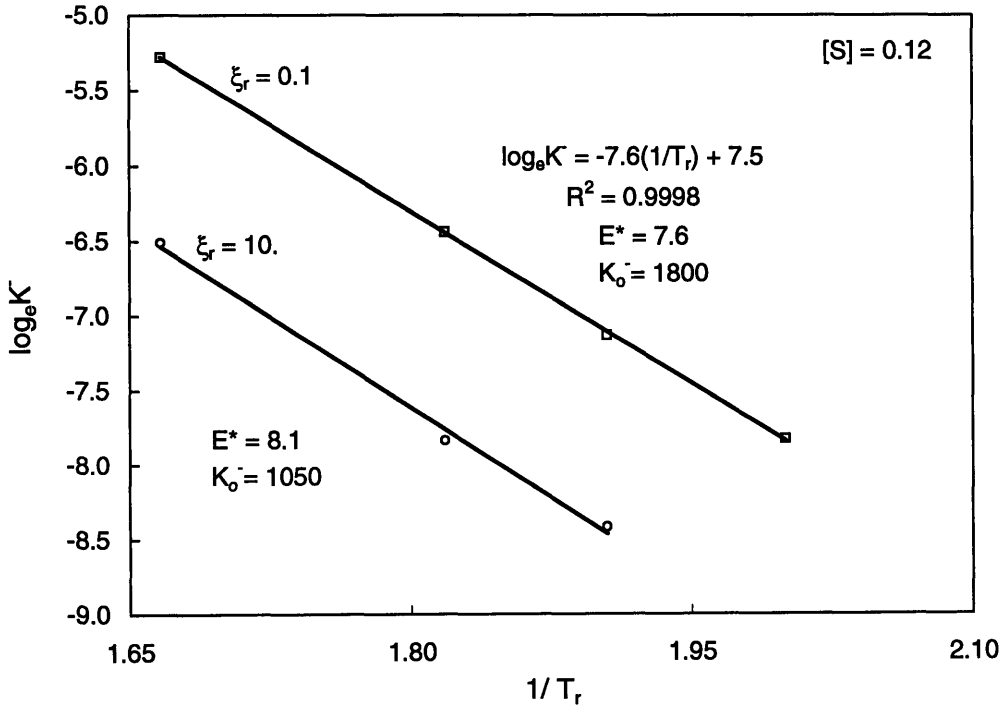

Figure 5-5: Arrhenius plot of the exit rate K^-. The activation energy, E^*, is found to be independent of ξ_r as expected.

The dynamics associated with the redistribution of surfactants among aggregates may also be used to extract exit and entry rate constants. Towards this end, all surfactants in aggregates are permanently tagged at $t = 0$. The number of tagged surfactants that still

reside in aggregates, $N(t)$, is then monitored as a function of time and is expected to obey the rate equation

$$\frac{dN(t)}{dt} = -K^{-}N(t) + K^{+}[N(0) - N(t)] \tag{5.9}$$

As before, we assume that the rate constants are nearly independent of the aggregate size i or alternatively we are content in obtaining an average value of the rate constant. The second term on the right of Eq. 5.9 reflects the fact that tagged surfactants can re-enter the micelles. Clearly the rate constant K^{+} must include the number density of aggregates. The solution of Eq. 5.9 yields

$$R(t) =< \frac{N(t)}{N(0)} >= \frac{1 + \beta e^{-\alpha t}}{1 + \beta} \tag{5.10}$$

where $\beta = K^{-}/K^{+}$ and $\alpha = K^{+} + K^{-}$. Figure 5-6 shows a two parameter fit (α, β) to the redistribution curve from which the rate constants in Table 5.1 were determined. Excellent agreement is obtained for the the exit rates constant K^{-} using these two tagging techniques and this provides some confidence in the obtained K^{+} values. However, as is evident in Figure 5-6, at long times, definite correlations in the data are evident which may be related to variations in the number density of micelles which vary during the course of the simulation.

Table 5.1: Summary of extracted rate constants as a function of temperature for $\xi_r = 0.1$ and [S] = 0.12

T_r	Exit Kinetics, C(t)	Redistribution Kinetics, R(t)	
	K^{-}	K^{-}	K^{+}
0.500	0.0004	0.0004	0.0184
0.525	0.0008	0.0008	0.0213
0.550	0.0016	0.0016	0.0295
0.600	0.0051	0.0055	0.0487

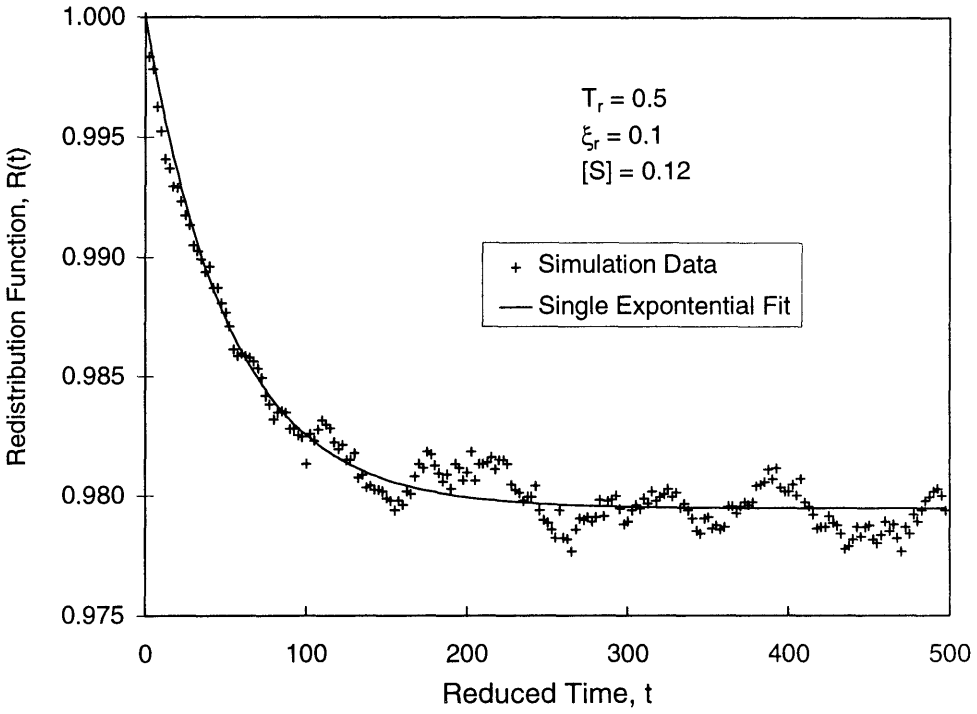

Figure 5-6: Redistribution of tagged surfactants among aggregates showing two parameter fit of Eq. 5.10

5.2.2 Free Energy of Chain Extraction

The free energy profile associated with the extraction of a surfactant chain from a micelle was determined. A typical micelle, aggregation number 38, was taken from an equilibrated system ($T_r = 0.50$, [S]=0.12) and used as an initial configuration for small scale SD simulations, at the same total surfactant concentration. The micelle was in dynamic equilibrium and was observed to lose and gain monomers throughout the simulation, maintaining an average aggregation number of 37.

A surfactant chain associated with the micelle was chosen at random and the first hydrophobic bead was constrained to lie a distance λ_i from the center of mass of the micelle. The free energy difference (ΔA_i), associated with a perturbation $\Delta\lambda$, was then calculated via the perturbation relation derived by Zwanzig [20] for a canonical ensemble

$$\Delta A_i = -\mathrm{kT} \ln < e^{-\Delta U_i/\mathrm{kT}} >_{\lambda_i} \tag{5.11}$$

The angular brackets denote an ensemble average over the unperturbed system, but with the constraint λ_i imposed. ΔU_i is the potential energy difference between the perturbed state $U(\lambda_i + \Delta\lambda)$ and its unperturbed value $U(\lambda_i)$. By repeating the calculation over a range of λ_i values a free energy profile may be obtained. At each value of λ_i we implement two perturbations $\pm\Delta\lambda$, and therefore from N distinct values of λ_i we get $2N$ free energy differences. The value $\Delta\lambda$ is chosen so that $\lambda_{i+1} - \Delta\lambda$ coincides with $\lambda_i + \Delta\lambda$. Therefore, by starting at the furthest separation distance (λ_0) and moving towards the center of the micelle, the free energy difference (with respect to a free surfactant chain) at a distance $r_k = \lambda_0 - k * \Delta\lambda$ from the micelle center is

$$\Delta A(r_k) = \sum_{j=0}^{k} \Delta A_j \tag{5.12}$$

An error estimate is obtained for each ΔA_i by subdividing the simulation data into five blocks (n) and determining ΔA_i for each block. The average $\overline{\Delta A_i}$ and standard deviation (σ_i) are therefore accessible [21].

$$\sigma_i^2(\overline{\Delta A_i}) = \frac{\sum_{j=1}^{n} (\Delta A_i(j) - \overline{\Delta A_i})^2}{n(n-1)} \tag{5.13}$$

where $\Delta A_i(j)$ is the estimate of ΔA_i taken from the j^{th} simulation block. Since $\Delta A(r_k)$ results from a summation over $\overline{\Delta A_i}$'s, the error propagates as we approach the center of the micelle. Assuming that the errors may be regarded as being independent, the standard deviation at a particular value of k is $\sigma_k = \sqrt{(\sum_{i=1}^{k} \sigma_i^2)}$. An alternative procedure would be to calculate an average standard deviation and then an error estimate in $\Delta A(r_k)$ is $\sigma^2(\Delta A(r_k)) = k\sigma_{avg}^2$. The obtained free energy profile at T_r =0.50 is shown in Figure 5-7(a) and a radial distribution profile through the micelle is shown in Figure 5-7(b).

The implementation of the constraint λ_i may affect the shape and micelle structure. If deformation does occur this will be manifested in a variation of $U(\lambda_i)$ and a correction must be made to ΔA_i to account for the free energy associated with micelle deformation. This was not found to be the case for reasonable values of λ_i as is indicated by the invariance of the system potential energy with λ_i as shown in Figure 5-8. The average energy for the system without any constraints was found to be -1.67 ± 0.02. If, however, a surfactant molecule was constrained so that the hydrophilic groups lay within the core of the micelle, deformation was evident.

The free energy profile for the extraction of a chain from a micelle of size 29 at $T_r = 0.55$ is shown in Figure 5-9. At the higher temperature, the micelle is far more labile and the micelle center of mass is constantly changing due to the loss and gain of monomers. This poses a particular problem in trying to constrain a surfactant to be a prescribed distance from the micelle center of mass, especially when for example a dimer leaves the micelle. If the imposed constraint failed to converge, a repeat run would be performed and the results averaged. Typically 6 runs were performed per data point from which an error estimate could be made. Two distinct differences are evident on comparing the free energy profile in Figure 5-9 to that for a micelle of size 37 at $T_r = 0.50$ shown in Figure 5-7(a); (1) the free energy at large radial distances drops off more rapidly for the smaller micelle and (2) the minimum in the free energy profile is almost 1 kT higher for the smaller micelle at the higher temperature.

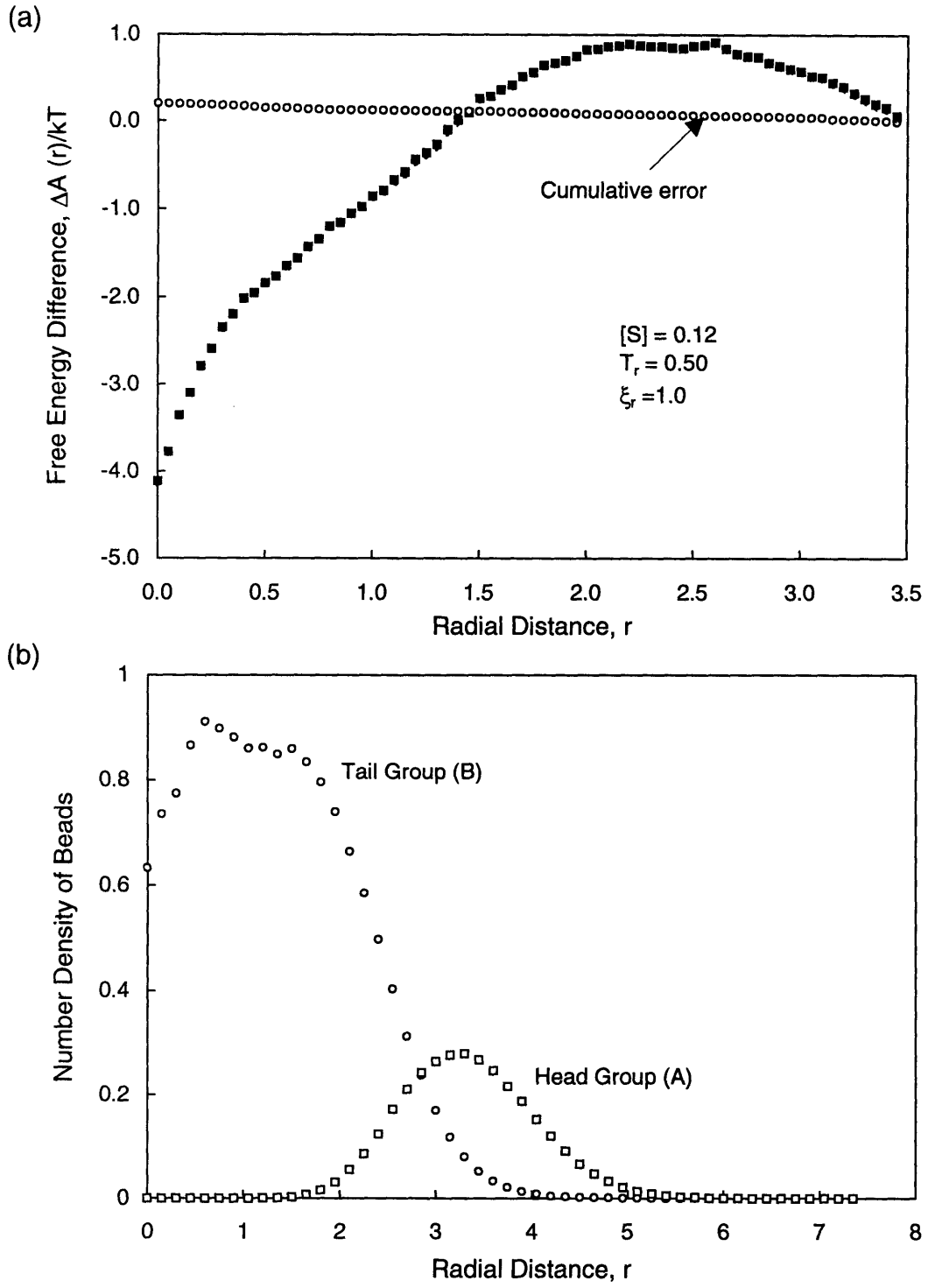

Figure 5-7: (a) Free energy profile through micelle of size 37 and cumulative error, as represented by the standard deviation, for each value of r. (b) Radial distribution profile through micelle of size 37.

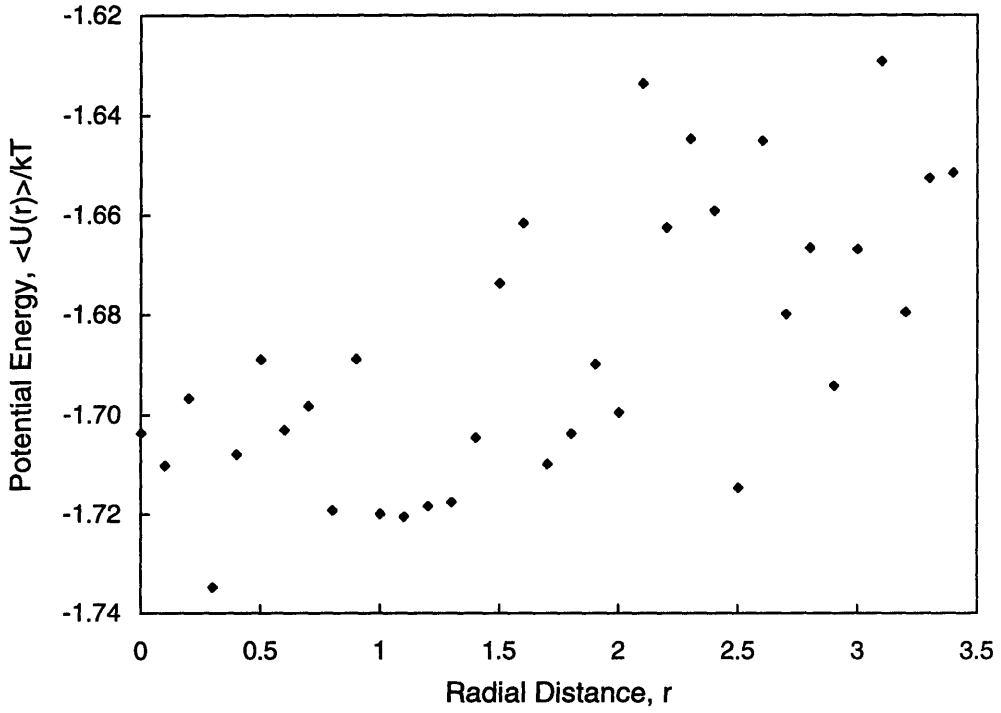

Figure 5-8: System potential energy $< U >$ as a function of λ_i. No significant trend can be observed, providing evidence that the constraint does not significantly affect the micelle structure.

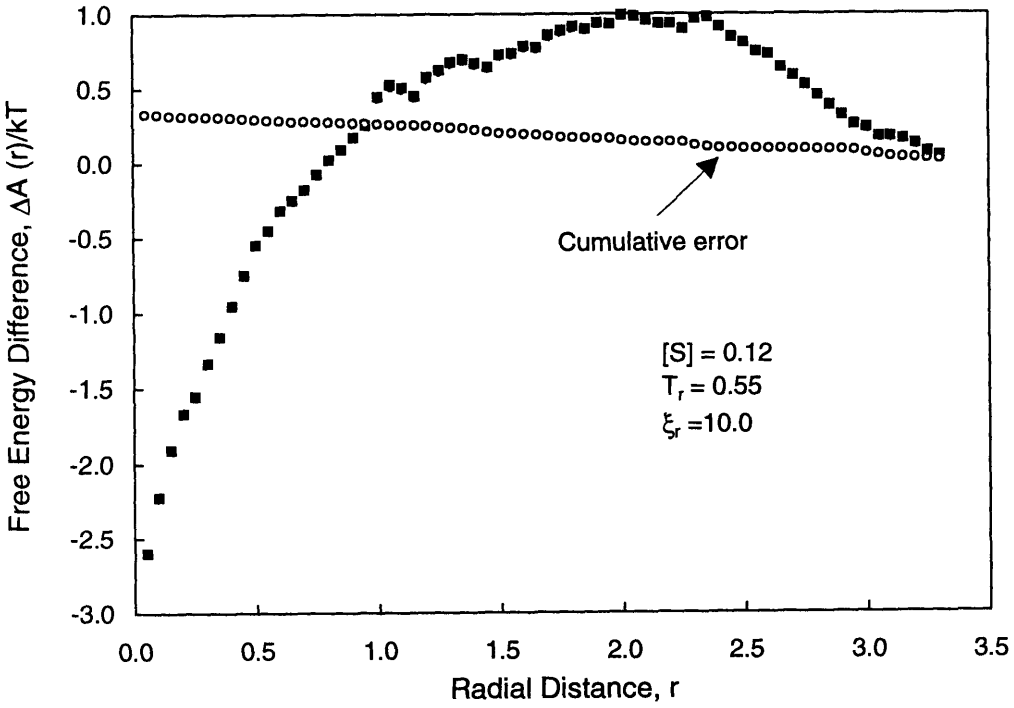

Figure 5-9: Free energy profile through a micelle of size 29 at $T_r = 0.55$. The cumulative error, as represented by the standard deviation, is shown for each value of the separation distance r.

5.2.3 Temperature Jump

Temperature jump computer "experiments" were performed to elucidate the dynamics involved in forming micelles. An initial equilibrated configuration (at T_o) was subjected to a rapid temperature change to a final temperature (T_f), and the response of the system was monitored as a function of time. In order to reduce the fluctuations in the instantaneous values calculated, the results were averaged over a number of independent starting configurations. Typically 10 - 30 runs were required to produce reasonable statistics.

The Aniansson-Wall (AW) mechanism is consistent with a number density of the aggregates which falls into three regions as depicted in Figure 5-10. Region I contains monomers and small aggregates (dimers, trimers etc.). Region III contains a distribution of micelles (assumed Gaussian by AW). The regions I and III are separated by a depleted zone (region II) where very few micelles are present. The fast process (monomer insertion/removal) is associated with reactions involving the species in sections I and III, while the slow process (micelle formation/dissolution) is governed by the low concentration of pre-micelles within the region II. The starting configuration at $T_r = 0.55$ fulfills these requirements and was

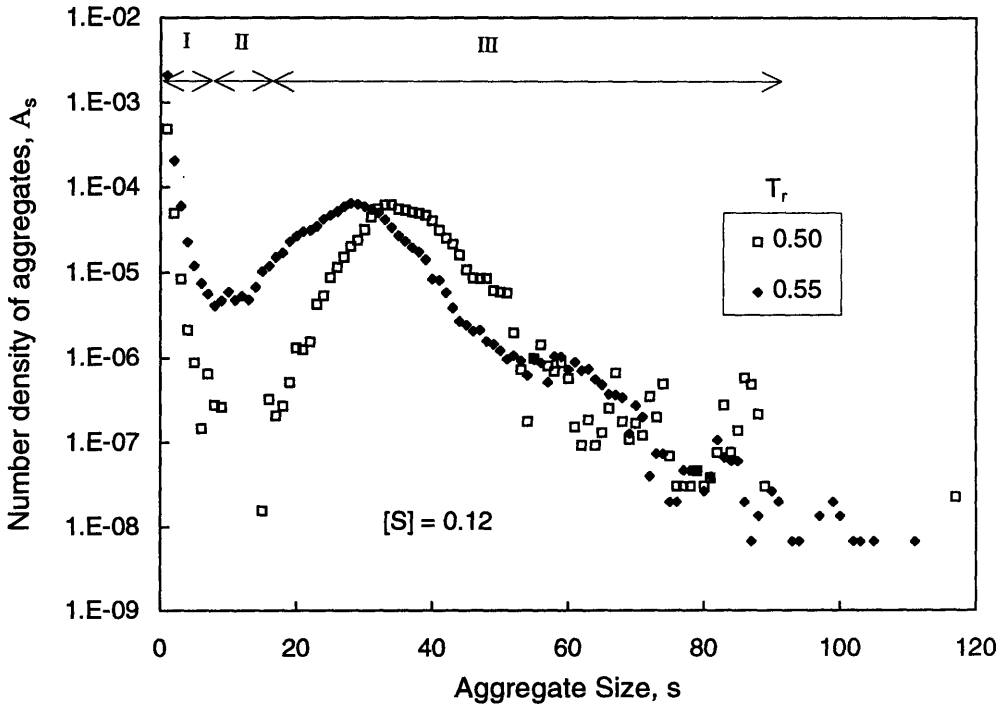

Figure 5-10: Size distribution of aggregates at initial and final temperature used in the temperature jump simulations.

perturbed to a temperature $T_r = 0.50$. The equilibrium properties corresponding to the starting and end points of the temperature jump have been calculated and are presented in Figure 5-11(a) and (b). The free surfactant concentration, [F] decreases with decreasing temperature. A decrease in temperature favours the formation of larger aggregates as reflected in the increased number and weight average aggregation numbers (excluding monomers), $N_n(ex)$ and $N_w(ex)$ in Figure 5-11(b). These results are consistent with an enthalpically driven micellization process. The system size was 864 surfactants at a total surfactant concentration of [S] = 0.12. The system was initially quenched to its new temperature by performing a short run (order 1000 timesteps) at high frictional coefficient. A production run at $\xi_r = 0.1$ was then performed. At low values of the frictional coefficient, the system responds only slowly to the imposed temperature change and the dynamics will be obscured by the dynamics of the temperature jump, therefore the necessity of an initial quenching run. The instantaneous values of the free surfactant concentration, [F], are presented in Figure 5-12. The system starts at its equilibrium value at $T_r = 0.55$ at t=0, decreasing rapidly to its final value as indicated by the dashed line. The free surfactant behavior appears to be well described by a single exponential decay. The evolution of the average aggregate size (N_n) is shown in Figure 5-13 and clearly it has not reached its equilibrium value even after t=1400. A very slow upward drift is still evident at long times. In addition, five long runs were performed to t = 3800 to ensure that we did in fact continue to approach the desired final equilibrium state. These data are far more noisy and are differentiated by the solid square markers. The effect of the friction coefficient was evaluated by repeating the temperature jump at $\xi = 0.43$ and $\xi = 4.3$, corresponding to a 40 fold variation in the friction coefficient. The results were in qualitative agreement with those obtained at $\xi_r = 0.1$, except that far longer runs were required. The long runs made it impractical to average over many initial configurations.

Two further temperature jump runs, as depicted by the direction of the arrows labelled (2) and (3) in Figure 5-11, were performed. Run (2) comprised a temperature increase from T_r=0.55 to T_r=0.60 and run (3) the equivalent temperature decrease, i.e. the reverse of run (2). These results are presented in the discussion where we compared the simulation results to the results predicted using the Aniansson-Wall series of flux equations.

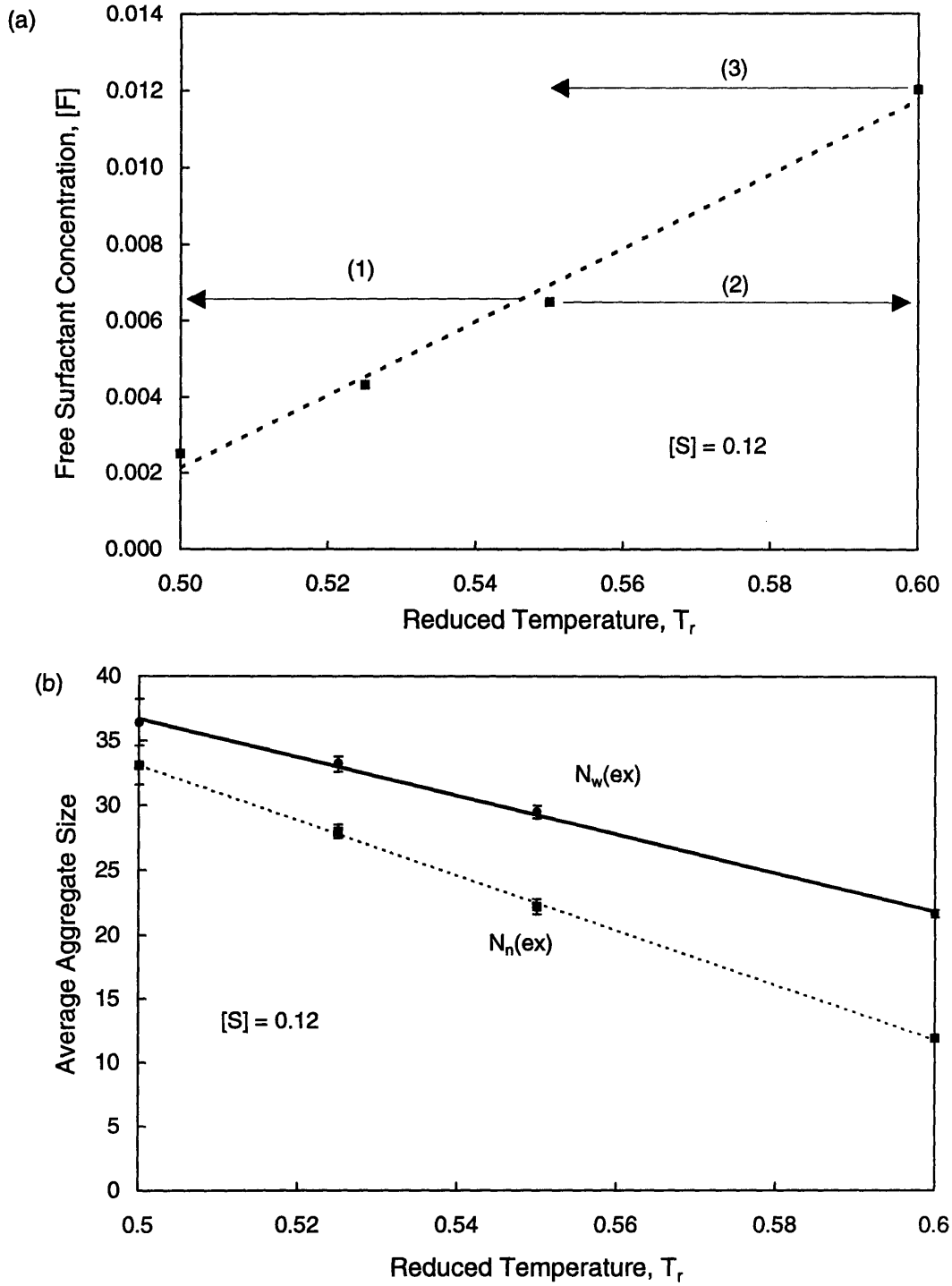

Figure 5-11: Equilibrium properties as a function of temperature at $[S] = 0.12$ (a) Free surfactant concentration [F]. The arrows depict the direction and magnitude of the temperature jump "experiments". (b) Number (N_n) and weight averaged (N_w) aggregation number. Error bars indicate $\pm$ std. dev. and are largest at the lowest temperature, $T_r = 0.50$, amounting to $\pm$ 5%.

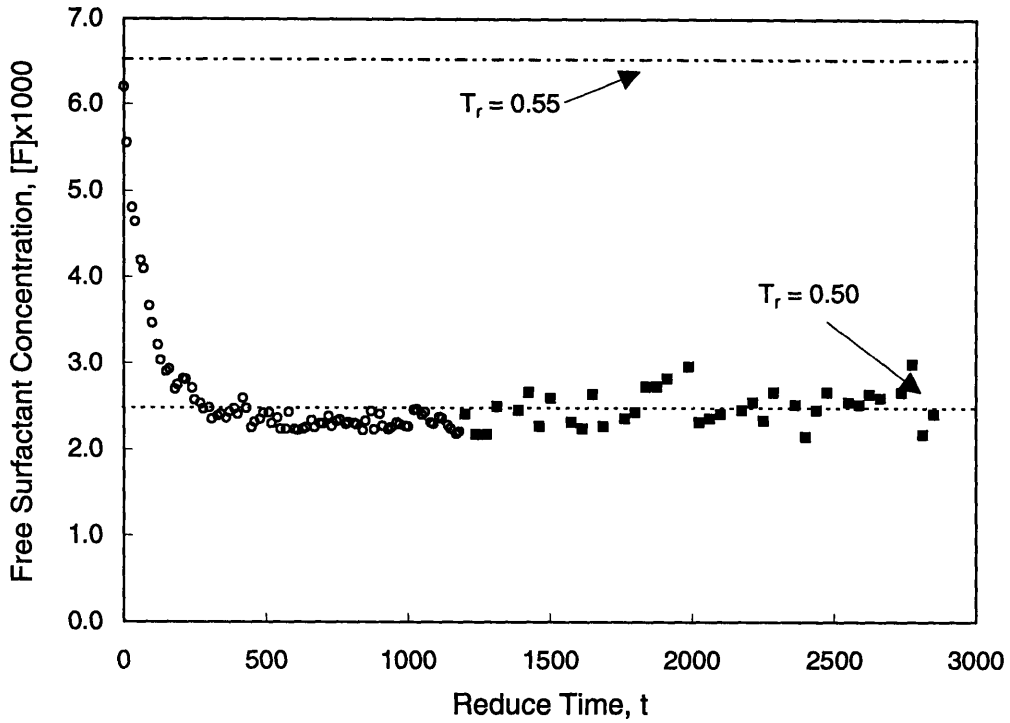

Figure 5-12: Variation in [F] following a temperature jump. Dotted line represents expected final equilibrium value at $T_r = 0.50$ while dot-dashed line represents initial configuration at $T_r = 0.55$.

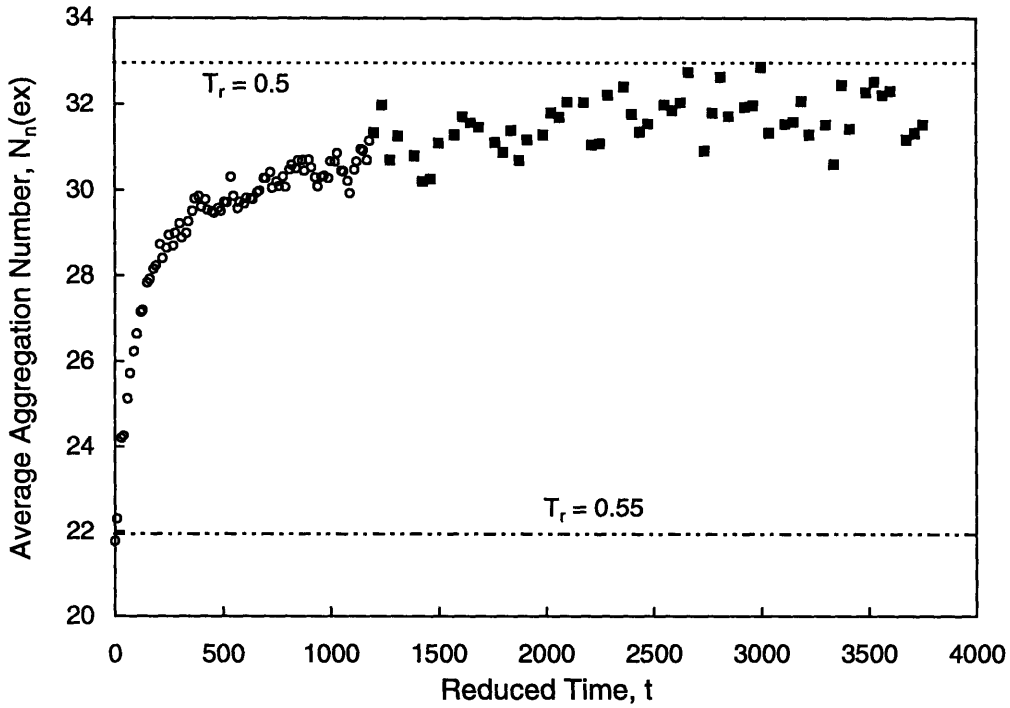

Figure 5-13: Instantaneous values of the average aggregation number of the system as a function of time, after an initial quench in temperature from $T_r = 0.55 \rightarrow 0.50$.

5.3 Discussion

5.3.1 Tagging Runs

For a simple double well potential, Zhou [22] has shown that for barrier heights greater than 3 kT, the dynamics of barrier crossings can be described by a chemical rate equation, and associated with this an exponential decay of the correlation function, for all values of the friction coefficient. This is confirmed in our work, where the barrier height (order 10-15 kT) is sufficiently large that $C(t)$ is always exponential in form.

The rate constants extracted from exit and redistribution of tagged surfactants, K^- and K^+, need to be related to those of micelle association and dissociation introduced in Eq. 5.1. This is achieved by considering aggregates of size i that contain j tagged surfactants, which are represented as $A_{i,j}$. The following reactions are possible :

$$A_{1,0} + A_{i,j} \underset{k^-_{i+1}}{\overset{k^+_{i+1}}{\rightleftharpoons}} A_{i+1,j} \tag{5.14}$$

$$A_{1,1} + A_{i-1,j-1} \overset{k^-_i}{\leftarrow} A_{i,j} \tag{5.15}$$

$$A_{1,0} + A_{i-1,j} \underset{k^-_i}{\overset{k^+_i}{\rightleftharpoons}} A_{i,j} \tag{5.16}$$

$$A_{1,1} + A_{i,j} \overset{k^-_{i+1}}{\leftarrow} A_{i+1,j+1} \tag{5.17}$$

Eq. 5.15 and Eq. 5.17 represent the expulsion of tagged surfactants which cannot re-enter the micelles and correspond to the first set of tagging runs where the tagged surfactants where detagged once they had left the aggregates. Eq. 5.14 and Eq. 5.16 are equivalent except for a shift in index i, similarly Eqs. 5.15 and 5.17 have both the indices shifted. The rate of accumulation of $[A_{i,j}]$ can then be expressed as :

$$\begin{aligned}
\frac{d[A_{i,j}]}{dt} &= (1 - \frac{j}{i+1})k^-_{i+1}[A_{i+1,j}] - k^+_{i+1}[A_{1,0}][A_{i,j}] \\
&- (\frac{j}{i})k^-_i[A_{i,j}] \\
&+ k^+_i[A_{1,0}][A_{i-1,j}] - (1 - \frac{j}{i})k^-_i[A_{i,j}] \\
&+ (\frac{j+1}{i+1})k^-_{i+1}[A_{i+1,j+1}]
\end{aligned} \tag{5.18}$$

The number concentration of tagged surfactants which are in aggregates at time t, $N(t)$, is

then simply given by

$$N(t) = \sum_{i=2}^{\infty} \sum_{j=0}^{i} j[A_{i,j}] \tag{5.19}$$

and evolves via

$$\frac{dN}{dt} = -\frac{k_2^-}{2} N_2 - \sum_{i=2}^{\infty} \frac{k_i^-}{i} N_i \tag{5.20}$$

where N_i is the concentration of tagged surfactants in aggregates of size i i.e. $N_i = \sum_{j=0}^{i} j[A_{i,j}]$. The additional term involving N_2 reflects the fact that when a dimer breaks up two free surfactants result. If the additional N_2 contribution is neglected, a comparison of Eq. 5.6 to Eq. 5.20 yields the following relationship

$$K^- N(t) \equiv K^- \sum_{i=2}^{\infty} N_i = \sum_{i=2}^{\infty} \frac{k_i^-}{i} N_i \tag{5.21}$$

The simulation results suggest that K^- is constant and time invariant and that Eq. 5.6 is a satisfactory description of the process. Therefore, in order for the two descriptions of $N(t)$ to be consistent we must conclude that $K^- = k_i^-/i$. This result is in agreement with our findings that the barrier energy associated with the expulsion of a chain is far larger than the thermal energy i.e. we are dealing with a large energy barrier. Therefore, the individual surfactants in a micelle all have equivalent energy in comparison to the barrier height and the probability of a micelle of size i losing a surfactant is given by $i\times$ {the probability of a single chain being expelled} i.e. the dissociation rate $k_i^- = iK^-$. This result is in agreement with the expression derived by Aniansson *et al.* [6] from the Smoluchowski equation for the dissociation constant

$$k_i^- = i \frac{D_m}{l_b l_o} e^{-\epsilon/kT} \tag{5.22}$$

where ϵ is the activation energy, D_m is the diffusion constant over the barrier, and l_b, l_o are related to the width of the barrier kT below its maximum. Obviously these arguments hold only for well defined micelles and cannot be extended into the pre-micelle region.

The redistribution runs can similarly be described by a set of reactions in which tagged surfactants are allowed to re-enter micelles. This yields the following expression for the time evolution of $N(t)$

$$\frac{dN}{dt} = -\frac{k_2^-}{2} N_2 - \sum_{i=2}^{\infty} \frac{k_i^-}{i} N_i + (N(0) - N) \left(k_2^+ (N(0) - N) + \sum_{i=2}^{\infty} k_i^+ [A_{i-1}] \right)$$

$$\approx \quad -\sum_{i=2}^{\infty} \frac{k_i^-}{i} N_i + (N(0) - N) \sum_{i=2}^{\infty} k_i^+ [A_{i-1}] \tag{5.23}$$

The two additional terms in comparison to Eq. 5.20 account for the re-entry of tagged surfactants into the micelle phase. Once again the term involving k_2^+ accounts for two tagged surfactants giving rise to dimers. The approximation made in the last part of Eq. 5.23 is justified since most surfactants are in the micelle phase and hence the terms involving the summations over the micelles will dominate the observed redistribution kinetics. Once again, by comparison to Eq. 5.9 we may infer

$$K^+ = \sum_{i=1}^{\infty} k_{i+1}^+ [A_i] \tag{5.24}$$

In the simulation, the variation of the concentration of aggregates, $[A_i]$, will therefore affect the extracted entry rate K^+. This is in part responsible for the observed correlations at long time shown in Figure 5-6. The expression for K^+ may be recast using the definition of $K_{eq,i}$ (Eq. 5.2) and the obtained approximation for $k_i^- = iK^-$ yielding

$$K^+ \approx K_{eq} K^- \left(\sum_{i=1}^{\infty} i[A_i] + \sum_{i=1}^{\infty} [A_i] \right) \tag{5.25}$$

where the constancy of K_{eq} in the micellar region, which was discussed earlier, is invoked. Therefore, from a knowledge of the equilibrium constant K_{eq} (extracted from the size distribution data and shown in Figure 5-17(b)) an estimate for K^+/K^- may be made, e.g. at $T_r = 0.60$, $K_{eq} \approx 250$ and the total surfactant concentration is 0.03, yielding an estimate $K^+/K^- = 7.5$ which is consistent with the result 8.8 obtained from the tagging runs shown in Table 5.1.

The exit rate K^- was found to depend strongly on the frictional coefficient, ξ_r (Table 5.1). An attempt was made to rationalize these results by relating the observed exit rate to the diffusion coefficient of a surfactant in the micelle phase. The required diffusion coefficients were estimated by calculating the mean squared displacement of the center of mass of the surfactant molecules. Two surfactant diffusivities were calculated, namely that of the unassociated (free) surfactant (D_f) and secondly that of the surfactant in the micelle phase (D_m, neglecting the micelle diffuisvity). A representative plot of the mean squared displacement as a function of time is shown in Figure 5-14(a). The slope of the linear

regression to these plots (at long times) yields the diffusivity via

$$D_\alpha = \frac{< |\mathbf{r}_{cm}(t) - \mathbf{r}_{cm}(0)|^2 >_\alpha}{6t} \tag{5.26}$$

where $\mathbf{r}_{cm}$ represents the center of mass of a surfactant chain and the angular brackets indicate an ensemble average over all surfactant chains in the phase α, either free monomers or the micelle phase. The diffusivity of the free surfactant, at infinite dilution, should be directly related to the frictional coefficient, ξ_r, since

$$D_f = \frac{T_r}{N_b \xi_r} \tag{5.27}$$

where $N_b = 4$ is the number of beads per surfactant chain. This result is confirmed by the calculated infinite dilution diffusivities as shown by the dotted line in Figure 5-14(b). The magnitude of D_m is however an order of magnitude lower and corresponds to the hindered diffusion of the surfactant molecules in the micelle phase due to interactions and collisions with the other surfactant molecules. Similarly the measured diffusivity of the free surfactant molecules, D_f, corresponds closely to the theoretically predicted infinite dilution diffusivities at high values of the friction coefficient. However, at small values of ξ_r, the measured diffusivity is one third of that expected at infinite dilution. At large ξ_r, the observed diffusivities are determined by the ξ_r. At small ξ_r, the motion of the beads is ballistic and the diffusivity is determined by collisions with other molecules and hence provides an indication of the mean free path that the molecule experiences. Figure 5-15 shows a plot of the exit rate constant K^- as a function of the surfactant diffusivity in the micelle, D_m. At small values of D_m the rate constant increases linearly. This is in qualitative agreement with Eq. 5.22 derived by Aniansson *et al.* [6] The measured diffusivity depends on the timescale of observation. If for example, the root mean squared displacement (rms) of a surfactant molecule in a micelle is calculated, three distinct regions are evident. At short times, the behaviour is determined by the frictional coefficient ξ_r. At intermediate times the hindered diffusion within the micelle is important. If we calculate the rms for a sufficiently long period of time, we eventually reach a third linear region, characteristic of micelle diffusion.

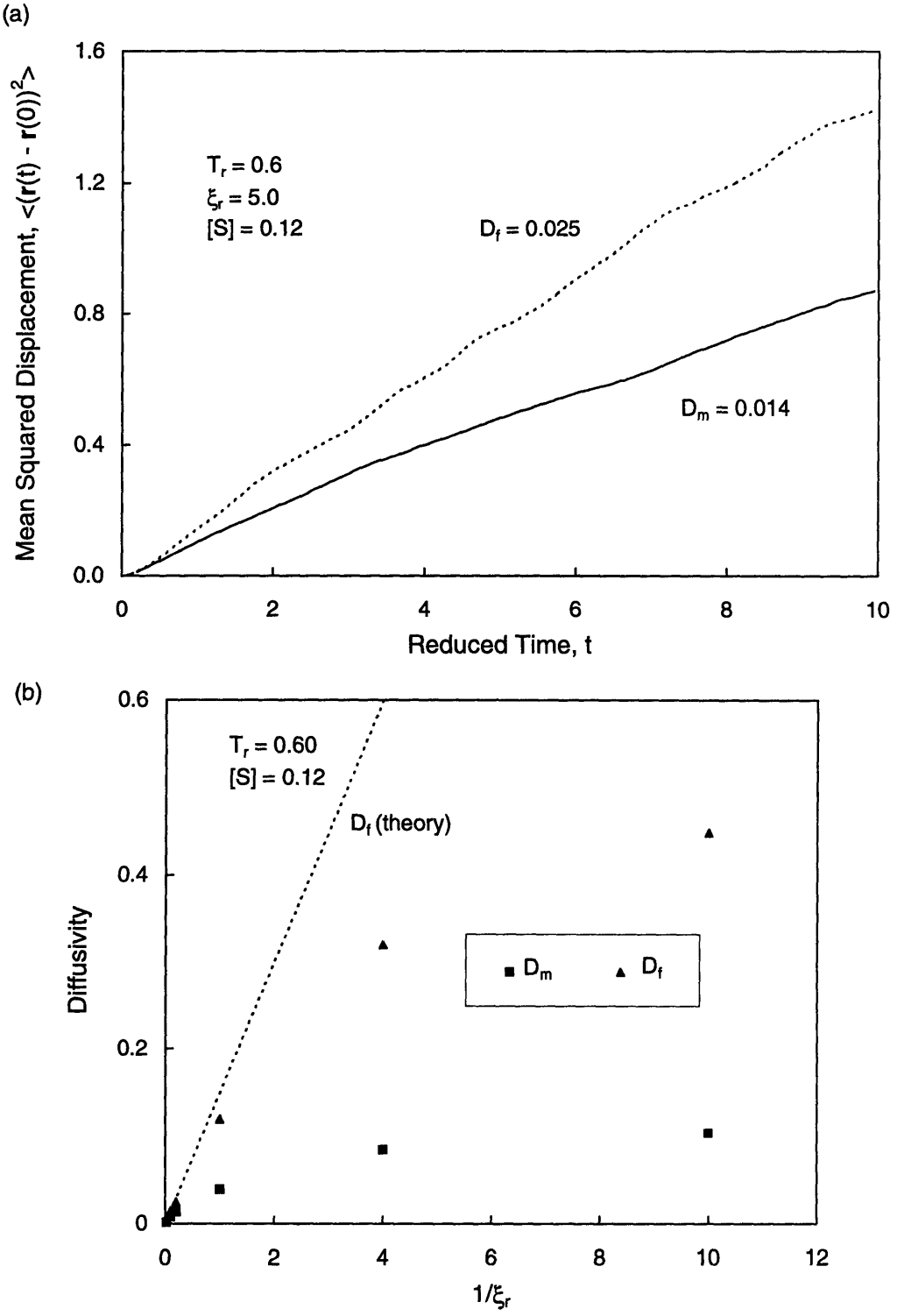

Figure 5-14: (a) Mean squared displacement of surfactant center of mass for free and associated surfactants yielding the diffusivity D_f and D_m respectively from Eq. 5.26 and (b) effect of the frictional coefficient, ξ_r, on D_f and D_m. The dotted line represent the theoretical result which corresponds to a system at infinite dilution.

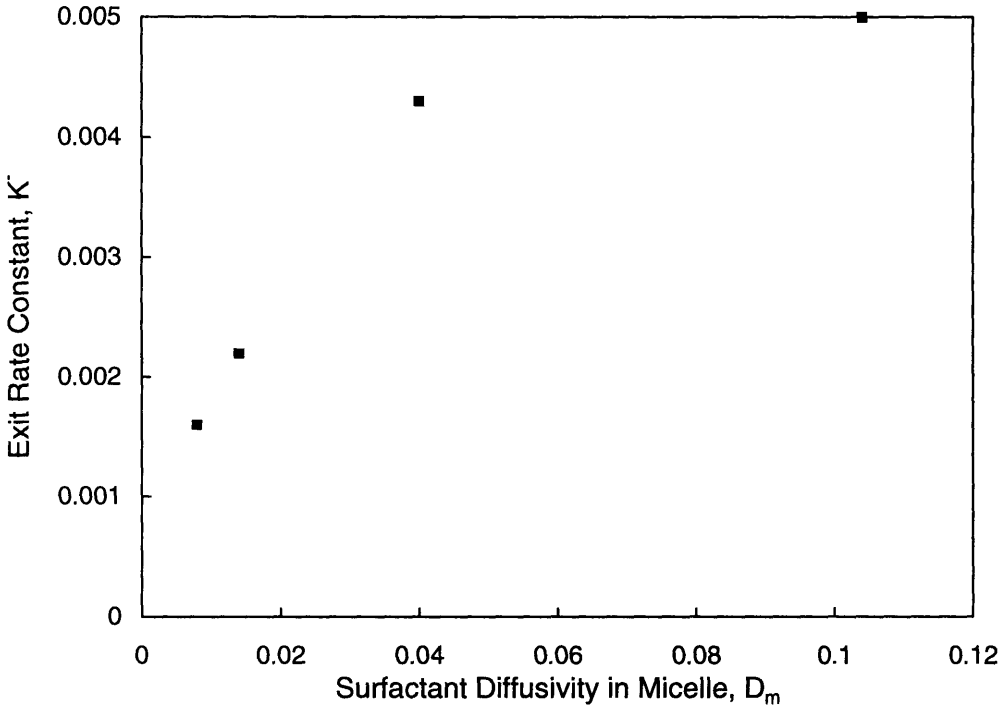

Figure 5-15: Variation of the surfactant exit rate (K^{-}) with the measured surfactant diffusivity in a micelle (D_m).

5.3.2 Chain Extraction

The height of the free energy barrier for chain extraction was found to be order 5 kT for a micelle of size 37 at T_r=0.50 and 3.6 kT for a micelle of size 29 at T_r=0.55. The free energy barrier is sufficiently large compared to the thermal energy that the assumption invoked in the last section of a large barrier is valid. The observed maximum in free energy coincides with the incorporation of the first bead into the hydrophobic domain (Figure 5-7).

In comparison to the activation energy obtained from the Arrhenius plot of the exit rate, the free energy barrier is roughly 50 % lower than the energy barrier. The difference may be ascribed to the negative entropic contribution do to the packing of the chains within the micelle.

The association rate (k^+) is expected to be diffusion controlled, due to the small free energy barrier associated with insertion of a monomer into a micelle (order 1 kT). This is in agreement with the results of Aniansson *et al.* [6].

Since the relevant driving force in our system is the Helmholtz free energy, we are now in a position to determine the surfactant exit rate using rate theory. In particular, the analytical solution of the probability distribution in phase space (the Fokker-Planck equation) for non-interacting Brownian particles in a potential well has been solved by Kramers [8, 23] over the entire range of frictional coefficients to yield

$$K^- = \frac{\omega}{2\pi\omega'}\left(\sqrt{(\frac{\xi^2}{4} + (2\pi\omega')^2)} - \frac{\xi}{2}\right) e^{-F^*/kT} \tag{5.28}$$

where, ω and ω' represent the frequency of the well and the peak of the free energy barrier of height F^* respectively, which may be obtained from the shape of the free energy profile. ξ is the frictional coefficient of the Brownian particle (in our case the actual diffusion coefficient of the monomer in the micelle, which as discussed previously depends on the timescale of observation). In the limit of low friction, the transition state theory rate constant is recovered. From the free energy profile at $T_r = 0.55$, we obtain F^*/kT=3.6, $\omega/\omega' \approx 2$ and ($2\pi\omega' \approx 1$). The predicted exit rate as a function of ξ is shown in Figure 5-16 and is in qualitative agreement to the results obtained from tagging runs shown in Figure 5-4. Clearly, the shift in the abscissa is consistent with the fact that the friction coefficient in Figure 5-16 corresponds to that of the monomer in the micelle.

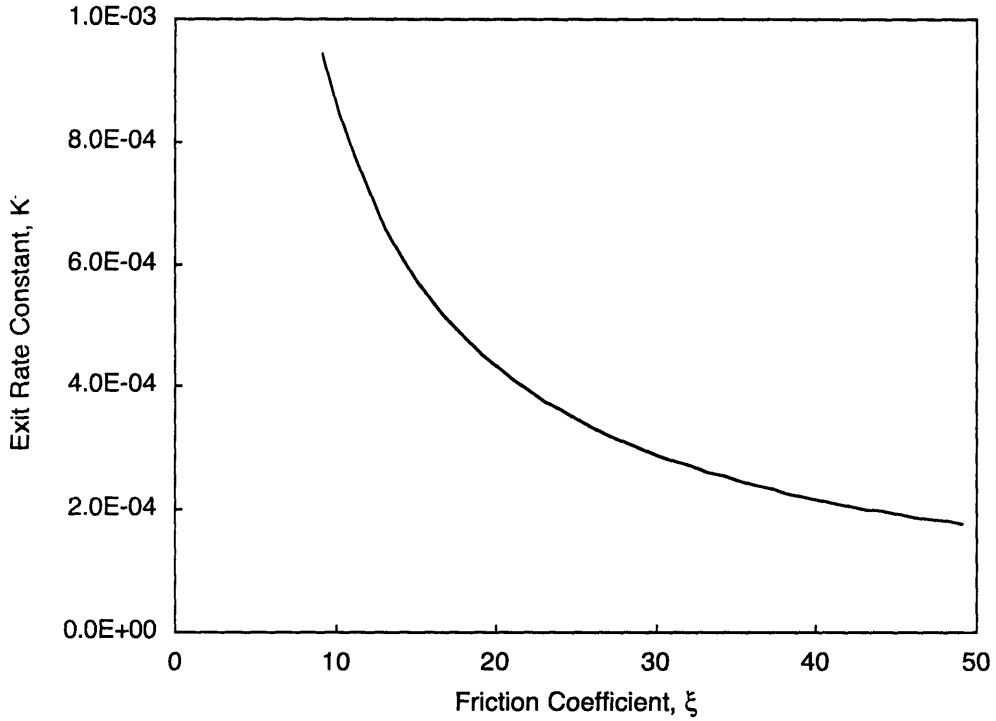

Figure 5-16: Variation of the surfactant exit rate (K^-) with friction coefficient (of monomer in micelle) as predicted using Kramers' rate theory and the free energy profile for chain extraction at $T_r = 0.55$

5.3.3 Temperature Jump

The ability to calculate the dissociation constant k_i^- in the previous section, provides the necessary information to evaluate the predicted response of the system to a perturbation using the flux equations derived by Aniansson and Wall [4]. The deviation from the equilibrium at some instant of time t, $\zeta_i(t)$, is defined as

$$\zeta_i(t) = \frac{[A_i(t)] - [A_i^{eq}]}{[A_i^{eq}]} \tag{5.29}$$

and evolves via the flux equation

$$[A_i^{eq}]\frac{d\zeta_i}{dt} = J_i - J_{i+1} \text{ for } i \geq 2 \tag{5.30}$$

where $J_i = -k_i^-[A_i^{eq}]\{\zeta_i - \zeta_{i-1} - \zeta_1(1 + \zeta_{i-1})\}$ is the flux of aggregates to i from $i-1$. Therefore, provided that the initial deviation from equilibrium ($\zeta_i(0)$), the final equilibrium concentration of all species ($[A_i^{eq}]$), and the dissociation rate k_i^- are known, the set of equations Eq. 5.30 may be integrated numerically in time. The monomer concentration is obtained from the mass balance constraint. We are therefore in a position to evaluate the proposed mechanism of Aniansson and Wall by direct comparison to the the temperature jump experiments described earlier.

In the previous section we evaluated the dissociation rate k_i^- from simulation data. We found that $k_i^- = iK^-$ and concluded that this is a reasonable approximation for i in the micellar region. At low aggregation numbers one would expect the dissociation constant to increase, a reflection of the labile nature of the small pre-micellar aggregates. In the pre-micellar region it is reasonable to assume that the association rate is diffusion controlled, i.e. $k_i^+ \approx$ constant and hence from a knowledge of the equilibrium constant $K_{eq,i}$, we may extract the dissociation rate. The obtained dissociation rate and measured equilibrium constant are shown in Figure 5-17(a) and (b) respectively. At low temperature ($T_r = 0.55$ and $T_r = 0.50$) the simulated data is noisy, particularly in the depleted zone where very few micelles exist and hence very long runs are required to obtained reasonable statistics. Over the range, $i = 1 \rightarrow 15$, a linear dependence of K_{eq} was assumed as shown in Figure 5-17(b). A matching condition at $i = 15$ was imposed in order to evaluate the association constant and hence extract the dissociation constant shown in Figure 5-17(a).

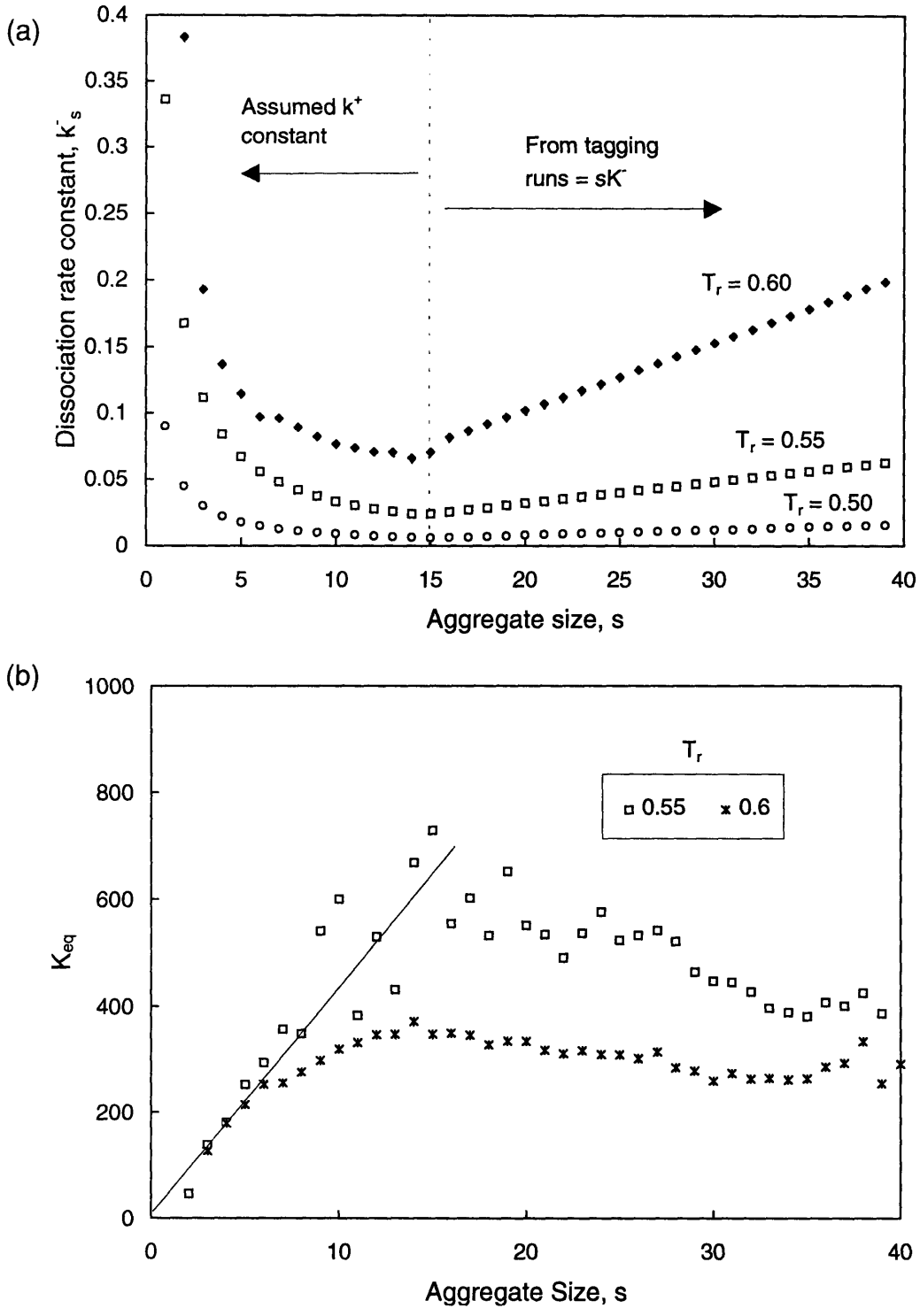

Figure 5-17: (a) Estimated dissociation rate (k_s^-) used in the solution of the Aniansson-Wall flux equations at [S]=0.12 (b) Equilibrium constant, $K_{eq,s}$, as a function of aggregation number.

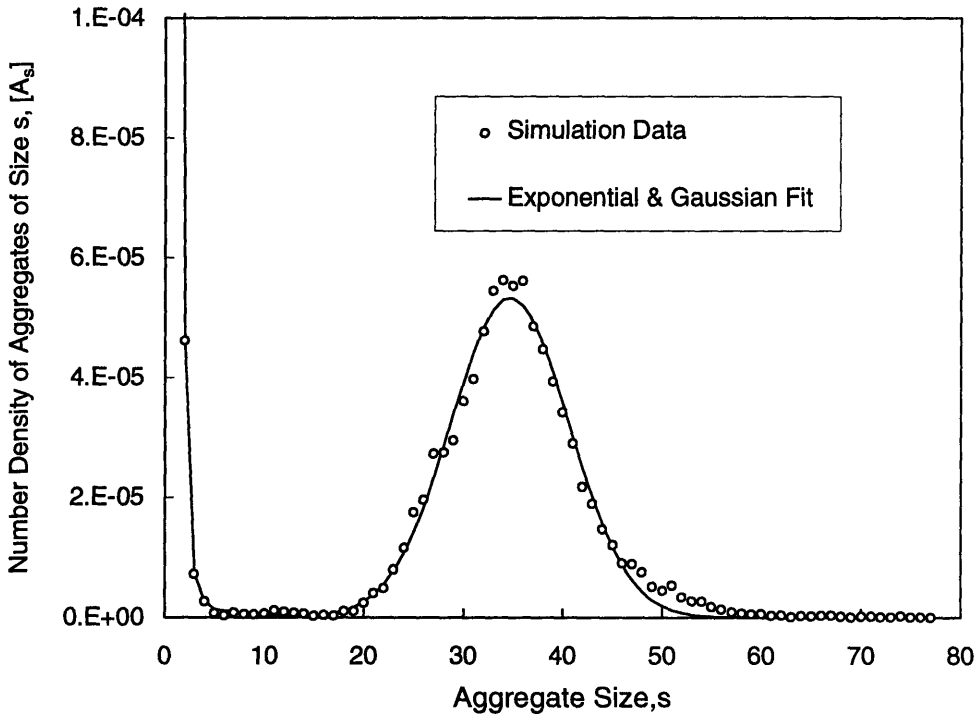

Figure 5-18: Example of fit to the number density distribution at $T_r = 0.50, [S] = 0.12$. The fitted function was used in the evaluation of the AW theory.

For $T_r = 0.50$, size distribution simulation data were fitted using a Gaussian in the micelle region (region III) and a single exponential in region I (oligomers). A fitted function was required for the AW theory, to smooth the statistical error associated with the simulation data in the depleted zone (region II). The quality of fit is shown in Figure 5-18 for the final equilibrium size distribution, $[A_i^{eq}]$. A comparison between the simulated temperature jump results and those obtained from the Aniansson-Wall theory is shown in Figure 5-19. The time evolution of the free surfactant concentration is found to be in excellent agreement. In fact, the Aniansson Wall theory suggests that the free surfactant concentration dips below its final equilibrium value (returning to its equilibrium value only after t=50 000). A similar result was found from the simulation data (Figure 5-19(a)) except that the timescale associated with the second process was far more rapid in the simulations. This is clearly shown in the transient behavior of the average aggregation number N_n (ex) (definition excludes monomers) shown in Figure 5-19(b). The agreement between AW theory and the simulated data is good at short times but deviates considerably after t=1000. The AW

theory predicts a far slower second relaxation process (10 fold slower). The first fast process, associated with monomer insertion, is well described by the AW theory and suggests that the independently extracted rate constants for $i > 20$ are in fact correct. The second slow process, associated with the formation and dissolution of micelles, is not well described. The slow process is determined by the concentration and rate constants in the depleted zone (region II). Micelle - micelle coalescence, which is not accounted for in the AW theory, is observed in the simulation and may account for some of the observed deviation. The approximations made however in determining the rate constants for $i < 20$ are believed to be the dominant reason for any discrepancy.

Two further temperature jump computer experiments were performed as depicted by the arrows (2) and (3) in Figure 5-11. Run (2) monitored the response of the system to an increase in temperature and therefore enabled us to probe micelle dissolution. The results are shown in Figure 5-20. The Aniansson-Wall theory was used, as described previously, to predict the system response. Similar results are shown in Figure 5-21 for the quench from T_r=0.60 to T_r=0.55. The size distributions corresponding to the start- and end-points of these runs is shown in Figure 4-5(b). A significant concentration of aggregates is present in the micelle depleted zone (II) and therefore it was unnecessary to fit a functional form to the data as was done in the analysis of Run (1). Also, at the higher temperatures, the equilibrium statistics are beter as shown by the calculated $K_{eq,s}$ values shown in Figure 5-17(b) at $T_r = 0.60$. Excellent agreement is obtained in predicting the response of the system to an increase in temperature. The micelles expel monomers and the average aggregation number, N_n, decreases. On forming micelles (run (3)) the agreement is not as good. The free surfactant concentration is well described, but the Aniansson-Wall formalism predicts a slower response in the number concentration.

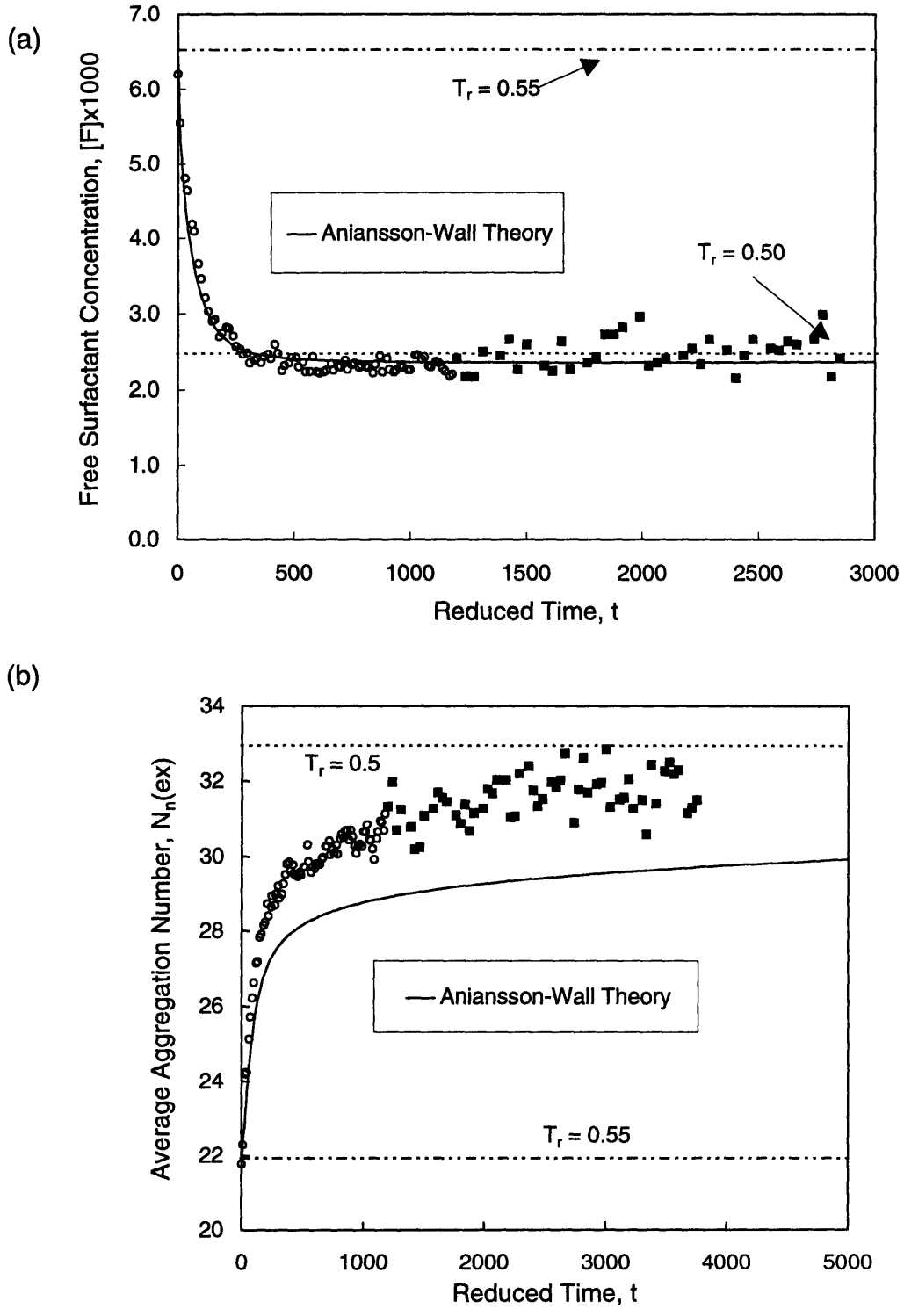

Figure 5-19: Comparison of simulated temperature jump data to that predicted using the Aniansson-Wall theory. (a) Time evolution of the free surfactant concentration ([F]) (b) and average aggregation number ($N_n(ex)$).

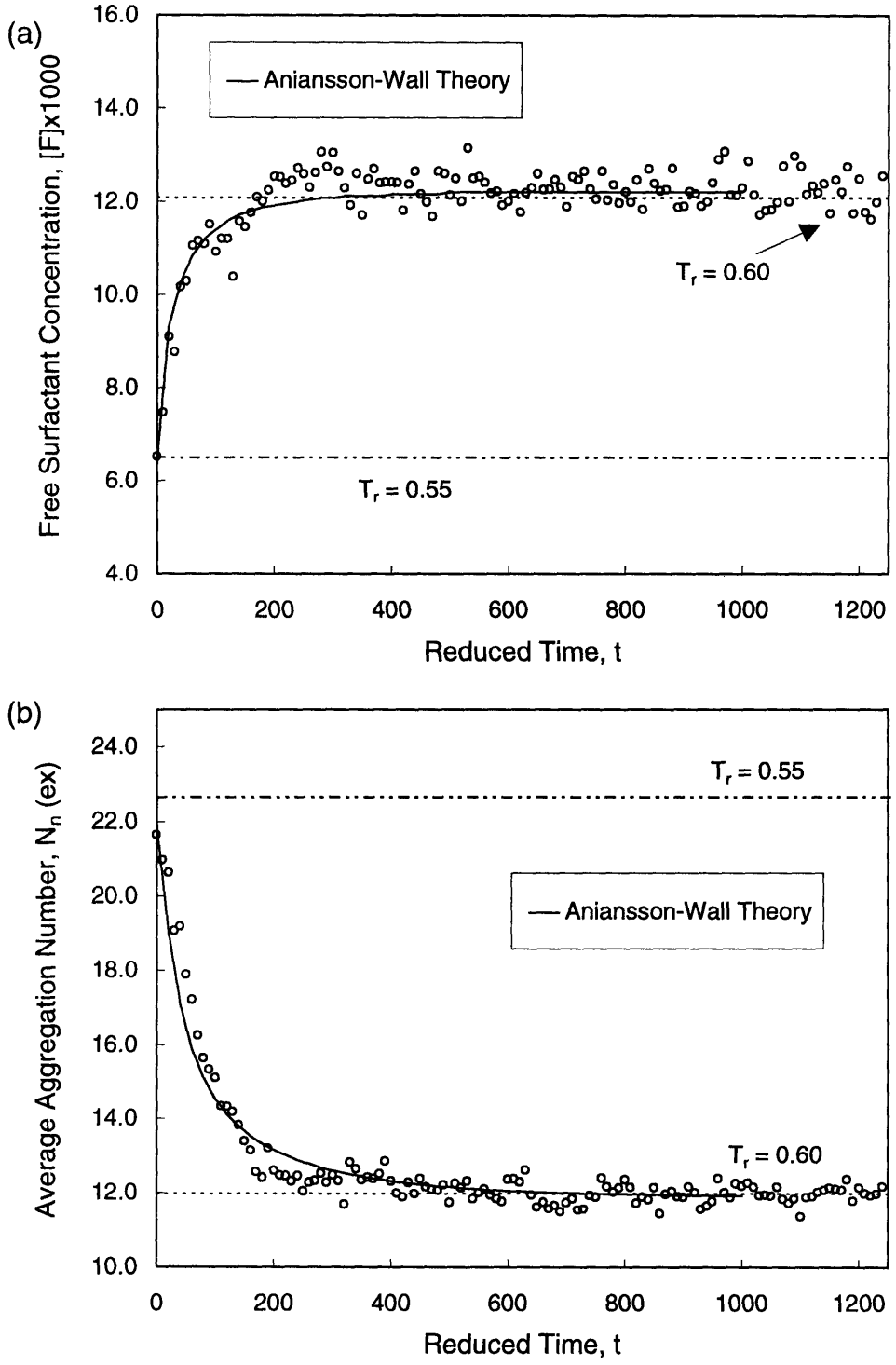

Figure 5-20: Temperature jump from T_r=0.55 to T_r=0.60. (a) Time evolution of the free surfactant concentration ([F]) (b) and average aggregation number ($N_n(ex)$)

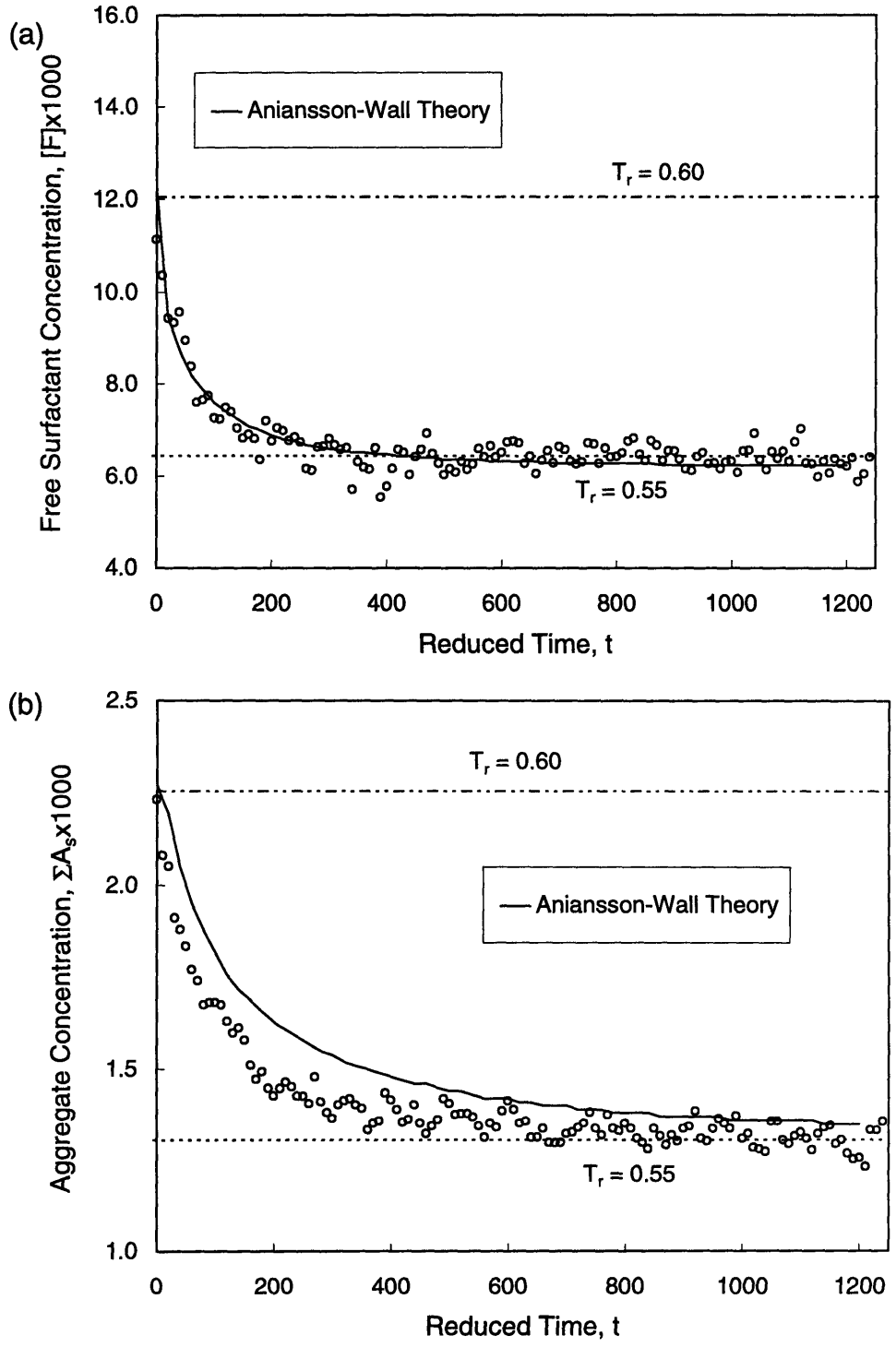

Figure 5-21: Temperature jump from T_r=0.60 to T_r=0.55.(a) Time evolution of the free surfactant concentration ([F]) (b) and aggregate concentration, $\sum_{i=2}^{\infty} A_s$

5.4 Conclusion

An attempt was made to extract information about the dynamics involved in micellar systems using stochastic dynamic simulations and to interpret these results based on available theory. In particular, by tagging surfactants in micelles, we have been able to evaluate a surfactant exit rate constant and relate this to the dissociation rate constant used in the step-wise association model of surfactant self-assembly. An activation energy of approximately 10-15 kT for chain extraction was obtained from the temperature dependence of the exit rate constant. A Helmholtz free energy profile for chain extraction was also evaluated.

The dissociation rate constants, together with the equilibrium number density distributions were used to evaluate numerically the Aniansson-Wall set of flux equations that describe the response of a system to a perturbation. The AW predicted response of the system to a temperature perturbation was compared to temperature jump computer experiments. Excellent agreement was obtained for the short time behavior which is associated with monomer insertion. Large deviations in the long time behavior, associated with the growth and dissolution of micelles, were ascribed to errors in estimating the dissociation rate and number density of aggregates in the all important micelle depleted zone.

Bibliography

[1] J. Lang, C. Tondre, R. Zana, R. Bauer, H. Hoffman, and W. Ulbricht, J. Phys. Chem. **79,** 276 (1975).

[2] R. J. Hunter, *Foundations of Colloid Science Vol. 1*, (Oxford Science Publications, 1991).

[3] H. Wennerström and B. Lindman, Physics Reports **52,** 1 (1979).

[4] E. A. G. Aniansson and S. N. Wall, J. Phys. Chem. **78,** 1024 (1974).

[5] M. Kahlweit and M. Teubwer, Advances in Colloid and Interface Science **13,** 1 (1980).

[6] E. A. Aniansson, S. N. Wall, M. Almgren, H. Hoffmann, I. Kielmann, W. Ulbricht, R. Zana, J. Lang, and C. Tondre, J. Phys. Chem. **80,** 905 (1976).

[7] M Kahlweit, Pure & Appl. Chem. **53,** 2069 (1981).

[8] H. A Kramers, Physica **7,** 284 (1940).

[9] A. Halperin and S. Alexander, Macromolecules **22,** 2403 (1989).

[10] T. Haliloğlu and W. L. Mattice, Chem. Eng. Sci. **49,** 2851 (1994).

[11] W. F. van Gunsteren, H. J. C. Berendsen, and J. A. C. Rullmann, Molec. Phys. **44,** 69 (1981).

[12] R. M. Levy, M. Karplus, and J. A. McCammon, Chemical Physics Letters **65,** 4 (1979).

[13] S. Glasstone, K. J. Laidler, and H. Eyring, *The Theory of Rate Processes*, (McGraw-Hill Book Company, Inc., New York , 1941).

[14] S. Z. Wan, Y. W. Xu, and C. X. Wang, J. Chem. Phys. **102,** 4976 (1995).

[15] R. Rey, J. Chem. Phys. **104,** 1966 (1996).

[16] R. W. Pastor and M. Karplus, J. Phys. Chem. **92,** 2636 (1988).

[17] S. Allison, R. Austin, and M. Hogan, J. Chem. Phys. **90,** 3843 (1989).

[18] T. Xiang, F. Liu, and D. M. Grant, J. Chem. Phys. **95,** 7576 (1991).

[19] F. Liu, W. J. Horton, C. L. Mayne, T Xiang, and D. M. Grant, J. Am. Chem. Soc. **114,** 5281 (1992).

[20] R. W Zwanzig, J. Chem. Phys. **22,** 1420 (1954).

[21] J. M. Haile, *Molecular Dynamics Simulations : Elementary Methods*, (John Wiley & Sons, INC, New York, 1992).

[22] H-X. Zhou, Chemical Physics Letters **164,** 285 (1989).

[23] V. I. Mel'nikov and S. V. Meshkov, J. Chem. Phys. **85,** 1018 (1986).

Chapter 6

Incorporation of a Potential of Mean Force in Stochastic Dynamics Simulations of Self-Assembly

6.1 Introduction

The purpose of performing stochastic dynamic simulations is to exclude the computationally intensive solvent effects present in MD simulations and to approximate them via a stochastic noise term and through a modified potential expression, called a potential of mean force (PMF). In Chapter 4 we investigated the self-assembly of a model amphiphile (A_2B_2) without including a potential of mean force. These simulations therefore do not take into account the effect of solvent structure and correspond to gas phase MD with a stochastic noise term that determines the molecular diffusivity and maintains the system at constant temperature via interaction with a heat bath. In situations where each amphiphile bead is far larger than the solvent molecules, the neglect of detailed solvent structure may be justified. In situations where bead and solvent molecules are comparable in size, solvent effects must be included. In this chapter we will address possible ways of including the solvent structure in stochastic dynamic simulations. A theoretical basis for the form of the potential of mean force will be presented and the limitations of this approach clarified. To

demonstrate this approach, the ability of SD to determine chain conformations and aggregation phenomena will be compared directly to equivalent MD simulations. Solvent memory effects are not included and therefore a delta correlated frictional kernel is employed.

The need for a potential of mean force was explained by Pratt and Chandler [1] and occurs naturally in the theoretical derivation of the Langevin equation by Deutch and Oppenheim [2]. The effect of including such an effective potential into the GLE has been discussed by Ciccotti and Ryckaert [3]. In this spirit Levy *et al.* [4] include in their SD simulations of butane and heptane the potential due to the solvent by the term $-kT \ln y$, where y is the cavity distribution function. For non-bonded interactions, the cavity distribution function for two methane molecules in water was used. The contribution of the solvent to the torsional potential was estimated by replacing each ethyl group by a sphere at the center of the ethyl C-C bond (pseudo-diatomic cavity model [5]). These simulations were performed in the diffusive limit (inertial effects were ignored).

Giró *et al.* [6] evaluated the success of incorporating a PMF by direct comparison to molecular dynamics simulation. A Langevin equation with a delta correlation memory function was employed (as in our work). A liquid krypton system was simulated at three different thermodynamic states (T, ρ). At each state the pair correlation function of krypton was calculated and then used as the input to subsequent SD simulations. The velocity autocorrelation function and pair correlation function obtained from the SD simulation of 107 atoms were compared to a corresponding system of 107 solute krypton atoms in 393 solvent krypton atoms. Good agreement was obtained in structural information, however the velocity autocorrelation did not show the characteristic backscattering that should be evident at high density. This was ascribed to assuming a delta correlated memory function. In subsequent work [7] an exponential memory function was included and the resultant autocorrelation functions more closely corresponded to the MD result. It was also found that the inclusion of the PMF did not effect the dynamics significantly. The PMF had a longer interaction range than that of the solvent-solvent forces and hence a larger cut-off distance was employed. In a later paper [8] dealing with identical solute-solvent molecules and the effect of changing the solute concentration, the authors observed large discrepancies from the MD result at high solute concentrations. A system of constant volume and number of solvent molecules was simulated with 32 - 152 solute atoms added. The authors failed to realise that increasing the number of solute atoms increases the solvent density and

hence modifies the potential of mean force that should be used. The potential of mean force between two solute atoms at infinite dilution is a function of the solvent density and temperature of the system.

Pastor *et al.* [9] performed Brownian Dynamics simulations of a single lipid chain in a membrane bilayer. A mean field approach was used to provide the potential energy surface of the membrane in which the chain resides. SD simulations of alanine dipetptide in water have also been performed [10]. The frictional coefficient on each atom was determined using the accessible surface area model that has been shown to reproduce the experimental diffusivities of simple molecules [11]. Stokes' law for a slip boundary condition is applied,

$$\xi_i = 4\pi\eta a_i/m_i \tag{6.1}$$

where η is the viscosity of pure solvent, m_i is the mass of the solute molecule and a_i is the hydrodynamic radius chosen to reproduce the exposed surface area. The solvent effect was accounted for by calculating the cavity distribution function for each pair of atoms in the molecule in pure solvent conditions and assuming that the superposition approximation holds, i.e. the molecular cavity distribution function may be taken as a product of pair atomic cavity distribution functions. The pair cavity distribution functions were obtained using the Ornstein-Zernike like RISM integral equation [12]. It is assumed that the solvent effect on the interaction of two isolated solute atoms (for which they calculated the cavity distribution function) is the same as that of two similar atoms interacting within the polyatomic molecule (dipeptide). This assumption will be good only for a highly hydrated molecule and serious deviations would be expected for the interior region of a collapsed protein molecule.

This chapter has the following structure. First we will discuss the theory behind the potential of mean force. We will then demonstrate how it may be calculated and subsequently apply the resulting potentials to simple solute-solvent systems in which all interactions are identical. The effect of solvent on single chains of length 4-16 beads is then presented and compared to the equivalent MD result. Finally, multiple chains in associating and non-associating conditions are investigated and compared to the MD result. Dynamics are not investigated since we realise that the short time dynamics will deviate considerably due to the absence of memory in our SD simulations and to probe the long time dynamics us-

ing MD is computationally difficult. The inclusion of a PMF is expected to influence the observed dynamics.

6.2 Theoretical Review

6.2.1 Single Component Systems

The probability of observing in a system of N molecules, *any* molecule in the element of volume $d\mathbf{r}_1$ at $\mathbf{r}_1$, a second molecule in volume element $d\mathbf{r}_2$ at $\mathbf{r}_2$, ..., and another in $d\mathbf{r}_n$ at $\mathbf{r}_n$ irrespective of the configuration of the remaining $N-n$ molecules is given by $\rho^{(n)}(\mathbf{r}_1, \mathbf{r}_2, \ldots, \mathbf{r}_n)d\mathbf{r}_1 \ldots d\mathbf{r}_n$ [13, 14] where

$$\rho^{(n)}(\mathbf{r}_1, \mathbf{r}_2, \ldots, \mathbf{r}_n) = \frac{N!}{(N-n)!} \frac{\int_V e^{-\beta U_N} d\mathbf{r}_{n+1} \ldots d\mathbf{r}_N}{Z_N} \tag{6.2}$$

and Z_N is the configurational integral for a system of N molecules, and U_N is the potential energy expression for the system (pairwise additive in our case) and is a function of the molecular coordinates $(\mathbf{r}_i, i = 1 \ldots N)$. For a fluid, $\rho^{(1)}$ is independent of location and corresponds to the macroscopic fluid density ρ i.e. $\int \rho^{(1)}(\mathbf{r}_1)d\mathbf{r}_1 = N$. A n^{th} order correlation function $g^{(n)}$ is defined to express deviations from independent behaviour, i.e. if the probability of a molecule being at $\mathbf{r}_1$ is independent of the probability of a particle being at $\mathbf{r}_2$ etc., then we can expect $\rho^{(n)}(\mathbf{r}_1, \mathbf{r}_2, \ldots, \mathbf{r}_n)$ to be the product of single particle probabilities $\rho^{(1)}(\mathbf{r}_i)$. Any deviation from this behaviour is incorporated in the correlation function $g^{(n)}$.

$$\rho^{(n)}(\mathbf{r}_1, \mathbf{r}_2, \ldots, \mathbf{r}_n) = \prod_{i=1}^{n} \rho^{(1)}(\mathbf{r}_i) g^{(n)}(\mathbf{r}_1, \mathbf{r}_2, \ldots, \mathbf{r}_n) \tag{6.3}$$

For a fluid, as mentioned earlier, $\rho^{(1)}(\mathbf{r}_i) = \rho$, the bulk density, and hence

$$\rho^{(n)}(\mathbf{r}_1, \mathbf{r}_2, \ldots, \mathbf{r}_n) = \rho^n g^{(n)}(\mathbf{r}_1, \mathbf{r}_2, \ldots, \mathbf{r}_n) \tag{6.4}$$

Consider the force acting on the i^{th} molecule of the subset n molecules in the systems. The force acting on molecule i is

$$\mathbf{f}_i = -\frac{\partial U_N}{\partial \mathbf{r}_i} \tag{6.5}$$

and its magnitude and direction are determined by the position of the N molecules in the

system. If we average Eq. 6.5 over the $(N-n)$ molecules (i.e. molecules not in the subset n) we obtain

$$\bar{\mathbf{f}}_i(\mathbf{r}^n) = \frac{\int -\frac{\partial U_N}{\partial \mathbf{r}_i} e^{-\beta U_N} d\mathbf{r}_{n+1} \dots d\mathbf{r}_N}{\int e^{-\beta U_N} d\mathbf{r}_{n+1} \dots d\mathbf{r}_N} \tag{6.6}$$

where $\bar{\mathbf{f}}_i$ is the average force exerted on molecule i averaged over all configurations of molecules $n+1 \dots N$ keeping the location of molecules $1 \dots n$ fixed [14]. Notice that the average force is still dependent on the set of coordinates of the n molecules $\mathbf{r}^n = (\mathbf{r}_1, \mathbf{r}_2, \dots, \mathbf{r}_n)$. By taking the derivative of Eq. 6.2 with respect to $\mathbf{r}_i$, and remembering that $\frac{1}{\rho^{(n)}} \frac{\partial \rho^{(n)}}{\partial \mathbf{r}_i} = \frac{\partial \ln(\rho^{(n)})}{\partial \mathbf{r}_i}$, one can write Eq. 6.6 as

$$\bar{\mathbf{f}}_i(\mathbf{r}^{(n)}) = \mathrm{kT} \frac{\partial \ln g^{(n)}}{\partial \mathbf{r}_i} = -\frac{\partial W^{(n)}}{\partial \mathbf{r}_i} \tag{6.7}$$

where the final equality serves as the definition of the potential of mean force (PMF)

$$W^{(n)} = -\mathrm{kT} \ln(g^{(n)}) \tag{6.8}$$

If we now employ the superposition approximation (assumes independent pair probabilities) we may rewrite Eq. 6.8 as :

$$W^{(n)} = \sum_{1 \le j < k < n} w_{jk} \tag{6.9}$$

where $w_{jk} = -\mathrm{kT} \ln g^{(2)}(|\mathbf{r}_j - \mathbf{r}_k|)$ and $g^{(2)}$ is simply the pair correlation function of the system under consideration. Hence the average force $\bar{\mathbf{f}}_i$ may be rewritten as :

$$\bar{\mathbf{f}}_i = \mathrm{kT} \sum_{k=1}^{n} \frac{d \ln(g^{(2)}(\mathbf{r}_{ik}))}{d\mathbf{r}_{ik}} = \mathrm{kT} \sum_{k=1}^{n} \frac{\mathbf{r}_{ik}}{r_{ik}} \frac{d \ln(g^{(2)}(r_{ik}))}{dr_{ik}} \tag{6.10}$$

where $r_{ik} = |\mathbf{r}_i - \mathbf{r}_k|$ is the scalar separation distance. This derivation can be extended to a multicomponent system which is performed in section 6.2.2. The applicable pair interaction terms in an SD simulation would therefore correspond to $-\mathrm{kT} \ln(g^{(2)}(r_{ij}))$, obtained at the temperature and density of interest.

6.2.2 Multicomponent Systems

Consider the canonical system $(\mathbf{N}, V, T)$ composed of the set of $\mathbf{N} = N_1, N_2, \dots, N_s$ particles, where we have s species with N_1 particles of species 1, and N_2 particles of species

2 etc. The probability of observing the set $\mathbf{n} = n_1, n_2, \ldots, n_s$ of particles in the volume element $\{\mathbf{n}\}d\{\mathbf{n}\}$ is then given by $\rho^{(n)}(\{\mathbf{n}\})d\{\mathbf{n}\}$ where

$$\rho^{(n)}(\{\mathbf{n}\}) = \prod_{i=1}^{s} \frac{N_i!}{(N_i - n_i)!} \frac{\int_V e^{-\beta U_{\mathbf{N}}} d(\{\mathbf{N}\} - \{\mathbf{n}\})}{Z_{\mathbf{N}}} \tag{6.11}$$

and the corresponding correlation function in a fluid is

$$g^{(n)}(\{\mathbf{n}\}) = \frac{\rho^{(n)}(\{\mathbf{n}\})}{\prod_{i=1}^{s} \rho_i^{n_i}} \tag{6.12}$$

where $\rho_i = N_i/V$. The shorthand notation $\{\mathbf{n}\}$ is used to represent the coordinates of the set of $\mathbf{n}$ particles. In an entirely analogous way to the derivation of the single component result, the average force exerted on particle i, averaged over the coordinates $(\{\mathbf{N}\} - \{\mathbf{n}\})$ of the $\mathbf{N} - \mathbf{n}$ particles, while the remaining $\mathbf{n}$ particles remain fixed at $\{\mathbf{n}\}$ is

$$\bar{\mathbf{f}}_i(\{\mathbf{n}\}) = \mathrm{kT} \frac{\partial \ln(g^{(n)}(\{\mathbf{n}\}))}{\partial \mathbf{r}_i} \tag{6.13}$$

The problem therefore involves making an estimate for the n^{th} order correlation function. For non-phase separating systems, the superposition approximation may be invoked as was done in section 6.2.1. In our case however, this is not possible since by definition microphase separation will occur when micelles form. We therefore need to further decompose the n^{th} order correlation function in a form that we may approximate and a component that we will simulate. It should be remembered that if the pair correlation functions for all species are known, the thermodynamic state of the system is specified.

Let's begin by introducing the following potential energy expression for a hypothetical system composed of n Brownian particles and N bath particles as used in the derivation of the Langevin equation.

$$\tilde{U} = U(\mathbf{r}^N) + \Phi(\mathbf{r}^N, \mathbf{R}^n) + \Psi(\mathbf{R}^n) \tag{6.14}$$

These terms represent solvent-solvent interactions, solvent-solute particle interactions and finally solute-solute particle interactions. All interactions will be assumed to be pairwise additive and to depend only the separation distance between the molecules. Using the

definition of the correlation function introduced section 6.2.2 we may write :

$$g^{(n)}(\mathbf{R}^n) = \frac{V^n \int e^{-\beta \tilde{U}} d\mathbf{r}^N}{\int e^{-\beta \tilde{U}} d\mathbf{r}^N d\mathbf{R}^n} + O(\frac{1}{n}) \tag{6.15}$$

Since the integration is over only the set of coordinates of the bath particles ($\mathbf{r}^N$), we can remove the Boltzmann factor associated with the interactions between the Brownian particles (solutes) to yield :

$$g^{(n)}(\mathbf{R}^n) = \frac{V^n e^{-\beta \Psi(\mathbf{R}^n)} \int e^{-\beta (U(\mathbf{r}^N) + \Phi(\mathbf{r}^N, \mathbf{R}^n))} d\mathbf{r}^N}{\int e^{-\beta \tilde{U}} d\mathbf{r}^N d\mathbf{R}^n} = e^{-\beta \Psi(\mathbf{R}^n)} y^{(n)}(\mathbf{R}^n) \tag{6.16}$$

This serves as the definition of the cavity distribution function $y^{(n)}(\mathbf{R}^n)$ where a cavity particle is distinguished only in the fact that it does not interact with other cavity particles (as reflected in the reduced potential energy expression in the Boltzmann factor). The cavity distribution function represents the solvent contribution to the interaction potential as can be seen by substituting the expression for $g^{(n)}(\mathbf{R}^n)$ into Eq. 6.13 yielding

$$\bar{\mathbf{f}}_i(\mathbf{R}^n) = -\nabla_{\mathbf{R}_i} [\Psi(\mathbf{R}^n) - \mathrm{kT} \ln \left(y^{(n)}(\mathbf{R}^n) \right)] \tag{6.17}$$

Therefore the problem reduces to determining the n^{th} order cavity distribution function. Notice the similarity with the Eq. 2.19 derived by Deutch and Oppenheim [2]. We are in a position to modify the direct solute-solute contribution, $\Psi(\mathbf{R}^n)$ since these are accounted for explicitly in the SD simulations. By decomposing $\Psi(\mathbf{R}^n)$ into an interaction term equivalent to the solvent-solute (Φ) term and a perturbation term (Ψ')

$$\Psi(\mathbf{R}^n) = \Phi(\mathbf{R}^n) + \Psi'(\mathbf{R}^n) \tag{6.18}$$

Eq. 6.17 can be rewritten as

$$\bar{\mathbf{f}}_i(\mathbf{R}^n) = -\nabla_{\mathbf{R}_i} [\Psi'(\mathbf{R}^n) - \mathrm{kT} \ln \left(e^{-\beta \Phi(\mathbf{R}^n)} y^{(n)}(\mathbf{R}^n) \right)] = -\nabla_{\mathbf{R}_i} [\Psi'(\mathbf{R}^n) - \mathrm{kT} \ln \left(\hat{g}^{(n)} \right)] \tag{6.19}$$

where $\hat{g}^{(n)}$ is the n^{th} correlation function of a hopefully well behaved, non-phase separating system with potential $\hat{U} = U(\mathbf{r}^N) + \Phi(\mathbf{r}^N, \mathbf{R}^n) + \Phi(\mathbf{R}^n)$, and therefore the superposition may be successfully applied. The actual use of this approach will be demonstrated by

examples in the subsequent section. It must however be emphasised that the successful use of this approach hinges on the ability to find a suitable system for which $\hat{g}^{(n)}$ can be accurately determined.

The PMF between solute molecules is therefore comprised of a modified direct contribution, $\Psi'(r)$ and a modified solvent contribution $-\mathrm{kT}\ln(\hat{g}(r))$. In the subsequent section we discuss how $\hat{g}(r)$ or its equivalent PMF, $\hat{W} = -\mathrm{kT}\ln(\hat{g}(r))$ may be calculated.

6.3 Calculation of PMF

6.3.1 Using the Pair Correlation Function g(r)

The potential of mean force may be directly calculated from the solute - solute pair correlation g(r) for the system under consideration.

$$W(r) = -\mathrm{kT}\ln(g(r)) \tag{6.20}$$

g(r) is directly accessible from molecular dynamics simulations. Sampling statistics are however very poor for a single pair of solute molecules in a solvent. This technique is therefore suitable only when we can average over a large number of particles, e.g. calculating the PMF between LJ solutes in a LJ fluid in which each solvent molecule is in fact a solute molecule and hence the pair correlation function can be obtained very accurately. Alternatively a biasing potential or umbrella sampling technique must be employed to restrict the solute molecules to the desired range (the effects of which must be subsequently removed analytically) [15].

For solute molecules that differ in character from the solvent, thermodynamic perturbation is a far more suitable technique to obtain the PMF.

6.3.2 Thermodynamic Perturbation Technique

NVT molecular dynamics simulations are performed in which the two solute molecules are constrained at a distance λ_i. The change in potential energy ($\Delta U_i = U_{i+1} - U_i$) is then calculated for a perturbation $\Delta\lambda$, keeping the position of the solvent molecules unchanged. An average is then taken over the ensemble of all possible solvent positions. The free energy difference (ΔA_i) associated with the perturbation from λ_i and λ_{i+1} is then given by [16]

$$\Delta A_i = -\mathrm{kT}\ln < e^{\frac{-\Delta U_i}{kT}} >_{\lambda_i} \tag{6.21}$$

where $<>_{\lambda_i}$ indicates an ensemble average over configurations where the constraint λ_i is imposed. The same technique was employed in Chapter 5 to calculate the free energy associated with the extraction of a surfactant chain from a micelle. The calculation of error bars was also discussed in detail in Chapter 5 and was employed in the same fashion in this

work. The PMF may then be calculated using :

$$W(\lambda_i) = \sum_{j=1}^{i} \Delta A_j \tag{6.22}$$

This technique has for example been employed to calculate the PMF between to two benzene molecules in water [17]. A novel and computationally efficient technique [18, 19] to calculate the free energy difference without performing extensive molecular dynamics simulations was recently applied to calculate PMF between two methane molecules in water and to study the solvent effects on butane conformations. This technique makes use of solute-solvent correlation functions.

Another technique using constrained MD, is to calculate the solvent contribution to the force on each solute molecule A and B ($\mathbf{F}_{AS}$ and $\mathbf{F}_{BS}$) constrained to lie a distance r apart. The solvent contribution to the force is then given by

$$\Delta F(r) = \frac{1}{2} < \mathbf{r}_{AB} \cdot (\mathbf{F}_{AS} - \mathbf{F}_{BS}) > \tag{6.23}$$

and integration thereof yields the solvent contribution to the PMF. This approach has been employed to determine the PMF of ion pairs (e.g. NaCl) in solution [20, 21].

6.3.3 Discussion

The PMF for a pair of Lennard-Jones (LJ) solutes in LJ solvents of varying quality are presented. Interactions are the energy-shifted Lennard-Jones potentials with cut-off distance r_c.

$$\phi(r) = \begin{cases} 4\epsilon\left[\left(\frac{\sigma}{r}\right)^{12} - \left(\frac{\sigma}{r}\right)^{6}\right] - \phi(r_c) & r \leq r_c \\ 0 & r > r_c \end{cases} \tag{6.24}$$

r is the separation distance and ϵ and σ are the well depth and size parameter in the LJ potential. For notational convenience we will refer to an interaction potential with $r_c = 2.5\sigma$ as being LJ attractive or LJ_a and that where the cut-off distance is $r_c = 2^{1/6}\sigma$ as LJ repulsive or LJ_r. Reduced coordinates, temperature and density are employed as described in Chapter 4. A reduced potential is defined as $U = \phi/\epsilon$. All MD NVT runs were performed using a leap-frog algorithm with velocity rescaling [22, 23]. The constraints were imposed using the SHAKE algorithm described in Chapter 3.

The potential of mean force between two LJ_a particles in a LJ_a solvent, obtained from the pair correlation function and using the perturbation scheme, is shown in Fig 6-1 at $\rho = 0.7$ and $T = 2.0$. The potential of mean force is indistinguishable from that of a LJ_r fluid (not shown) since it is the repulsive part of the potential that plays the major role in determining the pair correlation function. Also shown is the corresponding potential of mean force calculated using the thermodynamic perturbation scheme described in section 6.3.2 (error bars are equal to the size of the symbols). In calculating the PMF the reference free energy at $r_c = 2.5$ was taken to be zero. The perturbation scheme is computationally far more intensive requiring for each data point 300 000 timestep MD runs with 108 particles (order 1 hour cpu time on HP735/125MHz workstation). In contrast the pair correlation technique required a single 20000 timesteps MD simulation, since each solvent atom could in fact be taken as a hypothetical solute atom. It was therefore computationally expedient to truncate the PMF calculated using the thermodynamic perturbative scheme at $r_c = 2.5$. This simple test case was used to demonstrate that we can obtain the PMF using the thermodynamic perturbation scheme to sufficient accuracy. In comparison to the LJ potential (dot-dashed line in Figure 6-1), the oscillations in the PMF are indicative of the solvent structure (hydration shell) about the solutes. The range of the PMF is also considerably longer with oscillations still evident at r = 4 as noted by Giró *et al.* [6].

For two LJ_a solutes in a LJ_r fluid, the PMF is shifted by the LJ_a over the range $2^{1/6} < r < 2.5$ and by -1 over the range $0 < r < 2^{1/6}$. This follows directly from Eq. 6.21 in that only the direct solute-solute interaction has changed. If one wished to simulate using SD, a group of LJ_a particles in a LJ_r solvent in which the solvent-solute interactions are LJ_r then the relevant simulation potential ($W(r)$) would be

$$W(r) = \hat{W}_r(r) + H(r - 2^{1/6})H(2.5 - r)U(r) - H(2^{1/6} - r) \tag{6.25}$$

where $H(r)$ is the Heaviside unit step function and $\hat{W}_r$ is the potential of mean force for a system in which all interactions are LJ_r but at the same temperature and density. In the notation of section 6.2.2 the modified direct solute-solute contribution is

$$\Psi'(r) = H(r - 2^{1/6})H(2.5 - r)U(r) - H(2^{1/6} - r) \tag{6.26}$$

The PMF for two LJ_a solutes in a LJ_a solvent in which the solvent - solute interactions

are LJ_r is presented in Figure 6-2. The potential is considerably deeper than its counterpart in Figure 6-1 which reflects the fact that the solvent wishes to expel the solutes. This is manifested in a stronger affinity between the solute molecules. In order to use the calculated PMF in subsequent simulations, the PMF at T_r=2.0, $\hat{W}_r$, was subtracted from the data which was subsequently fitted to the following functional form

$$W(r) - \hat{W}_r(r) \quad = A\cos(Br + C) + D \tag{6.27}$$

where r is the separation distance and A through D are fitting parameters. The fit to the data is also shown in Figure 6-2. A predicted form of the PMF may be inferred from the following arguments. In a two component system (A=solvent-like, B=solute-like), it can readily be shown on a lattice that there is only one energy parameter of interest $\epsilon = \epsilon_{AB} - 1/2(\epsilon_{AA} + \epsilon_{BB})$. Therefore systems with the same value of ϵ, irrespective of how the energy is distributed among the individual interactions, are equivalent. One may therefore incorporate the LJ_a interactions between the solvent molecules (ϵ_{AA} interactions) into the direct solute-solute interaction (ϵ_{BB} interactions) yielding the following approximation for the PMF of two LJ_a solutes in an incompatible LJ_a solvent.

$$W(r) \approx \hat{W}_r(r) + 2H(r - 2^{1/6})H(2.5 - r)U(r) - 2H(2^{1/6} - r) \tag{6.28}$$

where $H(r)$ is the Heaviside unit step function and $\hat{W}_r$ is the potential of mean force for a system in which all interactions are LJ_r but at the same temperature and density. This predicted PMF is shown as the dotted line in Figure 6-2.

The potential of mean force is a function of the system density and temperature and hence must be obtained for each set of state variables (T,ρ). The temperature and density dependency is shown in Fig. 6-3 for a LJ_r system. As the temperature increases, so does the well depth and the magnitude of the potential oscillations. The net result is that U_r/kT is only slightly temperature dependent. As the density increases, the peaks and troughs in the PMF shift to lower values of the separation distance, r. The solvent contribution to the PMF may be obtained by simply subtracting the direct interaction contribution (solute-solute interaction term) from the potential of mean force. The obtained PMF's are for solutes at infinite dilution.

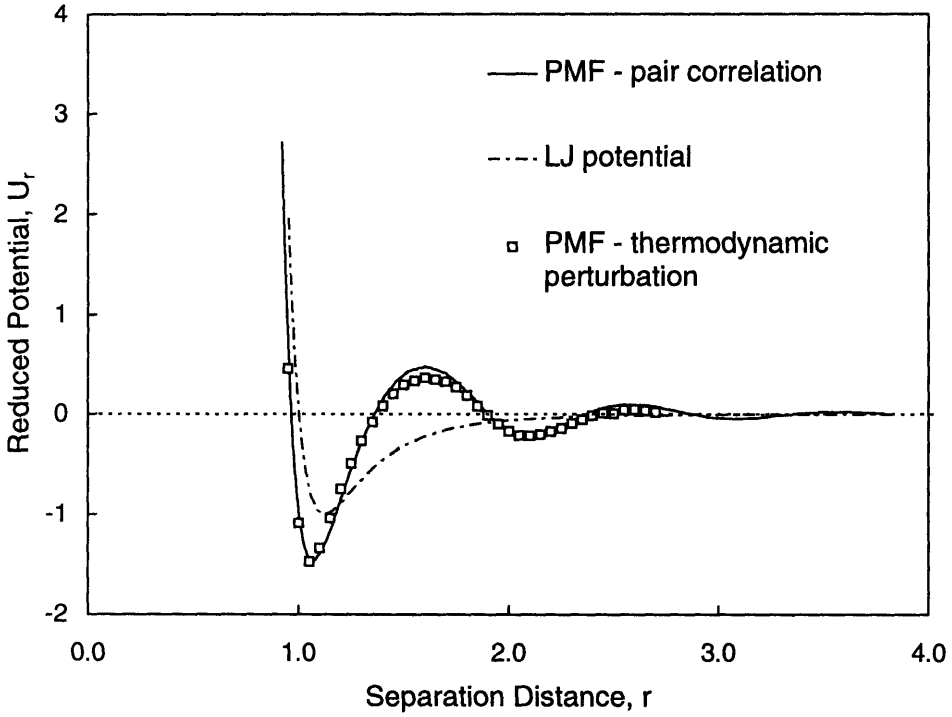

Figure 6-1: Potential of mean force between two LJ_a particles in a LJ_a solvent at $\rho = 0.7$ and $T = 2.0$. Symbols indicate PMF obtained using thermodynamic perturbation. Dashed-dotted line indicates LJ potential.

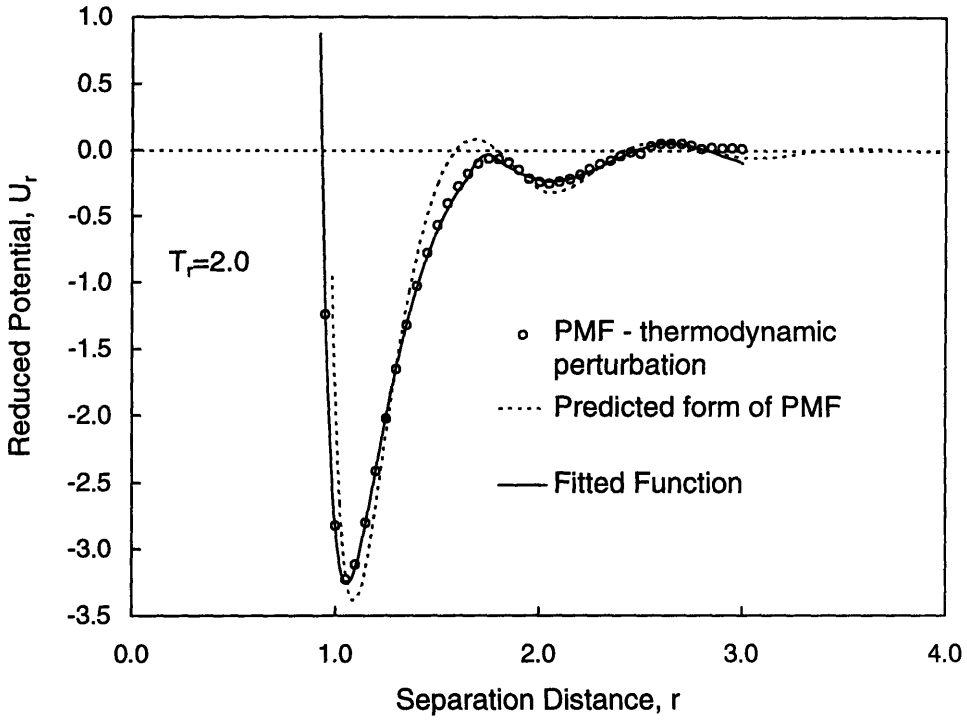

Figure 6-2: PMF of LJ_a solutes in incompatible LJ_a solvent where the solute-solvent interactions are LJ_r at $\rho = 0.7$, T_r=2.0

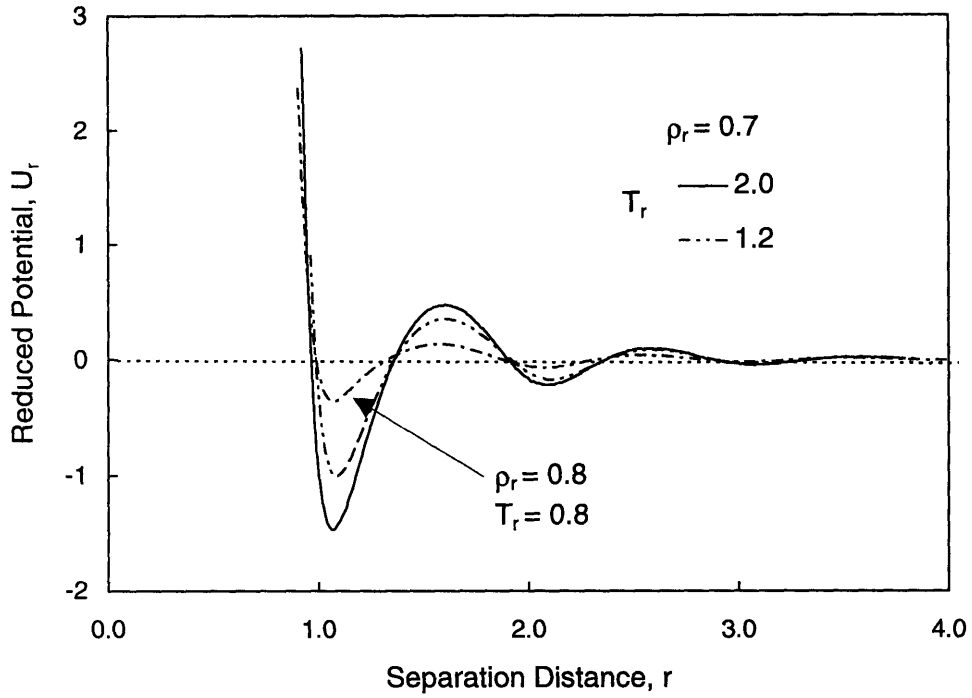

Figure 6-3: The effect of temperature on the PMF at $\rho = 0.7$ for a system of LJ_r solutes in a LJ_r solvent. Also shown is the PMF for $\rho = 0.8$, T_r=0.8. These results were obtained using the pair correlation function.

6.4 Single Chain Systems : Solvent Effects

6.4.1 Background

Initial work in this area included performing molecular dynamic simulations on hard sphere chains [24] of various lengths ($N = 10 - 50$) in the absence of solvent. Later solvent effects were taken into account [25] and FENE ($N = 5$ and 10) chains in a LJ solvent [26] were also simulated. Unfortunately all this work was performed at low density $\rho \approx 0.3$ and/or high temperature $T \approx 10$, hence the effect of solvent structure is minimal (in fact the solvent is gas-like). Dynamical properties were also investigated. Bruns and Bansal [27] attempted to model a nonamer (N=9) at realistic densities. However, they were unable to sample the configurational space and their results for solvent-immersed chains are meaningless. Sampling problems also plagued later work [28]. Smit *et al.* [29] and Luque *et al.* [30] have performed extensive studies looking at various chain lengths ($N = 8 - 20$), different chain models (rigid, FENE, harmonic) and different solvent quality. Solvent effects were found to be important in the equilibrium and dynamic properties. Thus it is important in our work to understand the effect of solvent structure on chain conformation. In the following sections we shall investigate this effect and check which details SD simulations are able to capture and what modifications are required to make the simulations more realistic. No work has been done to evaluate the success of incorporating a PMF in SD simulations on the calculated structural properties of chains.

6.4.2 Variables of Interest

In order to characterise equilibrium properties of polymer chains (length N) we employ the mean square end-to-end distance $< R^2 >$, the radius of gyration squared $< S^2 >$ and the ordered set of eigenvalues $(\lambda_1, \lambda_2, \lambda_3)$ from the moment of inertia tensor ($\mathbf{T}$). These properties are defined by :

$$< R^2 >=< |\mathbf{r}_N - \mathbf{r}_1|^2 > \tag{6.29}$$

and

$$< S^2 >= \left\langle \frac{\sum_{i=1}^{N} |\mathbf{r}_i - \mathbf{r}_{cm}|^2}{N} \right\rangle \tag{6.30}$$

where $\mathbf{r}_{cm}$ is the center of mass of the polymer chain and $\mathbf{r}_i$ is the position of the i bead in the polymer chain.

$$T_{\alpha,\beta} = \frac{\sum_{i=1}^{N}(r_{\alpha,i} - r_{\alpha,cm})(r_{\beta,i} - r_{\beta,cm})}{N} \tag{6.31}$$

The angular brackets denote a configurational average and α and β represent any of the cartesian coordinates (x,y,z). These variables have been traditionally used in the literature to compare properties of single polymer chains. These definitions can also be extended to aggregates of surfactant chains and have been employed to describe the shape of micelles in Chapter 4.

6.4.3 Static Properties

Molecular Dynamics (MD) simulations were performed at $\rho = 0.7$, $T_r = 2.0$ and $\Delta t = 0.005$ and compared to stochastic dynamics (SD) simulations with and without the relevant potential of mean force. Chain lengths from N=2 to N=16 were considered. All SD simulations included 4 non-interacting molecules ($\rho = 0.0001\sigma^3$) to improve sampling statistics and were simulated for 10^6 timesteps. MD simulations ranged in size from 500 to 4000 particles containing only a single chain molecule. All results are given in reduced units.

Table 6.1 shows how the radius of gyration squared and mean squared end-to-end distance are affected by the presence of the solvent for $r_c = 2^{\frac{1}{6}}$. The SD simulations consistently overestimate $< R^2 >$ and $< S^2 >$. The deviation from MD results becomes larger for longer chains. The large error bars associated with the long chain MD results are indicative of the difficulty associated with sampling the configuration space of a large polymer molecule (hence very long simulations are required). System size was found to have no effect on the MD results as shown in Table 6.1 for N=7 and N=10.

Table 6.2 shows the analogous set of results for a LJ_a solvent ($r_c = 2.5$) which are compared to SD results with attractive LJ interactions between the beads ($r_c = 2.5$). The MD and SD results are statistically indistinguishable. Also it should be noted that the MD results for ($r_c = 2.5$) and ($r_c = 2^{\frac{1}{6}}$) are similar. The potential of mean force (PMF) for LJ solutes in a LJ fluid was calculated in section 6.2.1 . The PMF was shown to be predominantly determined by the repulsive part of the interaction potential. This is confirmed by the fact that the configuration of the polymer chain calculated via MD were

Table 6.1: Solvent effects on polymer conformation : $r_c = 2^{\frac{1}{6}}$

Chain Length	MD				SD	
N	Timesteps	System Size	$< R^2 >$	$< S^2 >$	$< R^2 >$	$< S^2 >$
4	600 000	500	4.5 ±0.2	0.87 ±0.01	5.1 ±0.1	0.93 ±0.01
5	600 000	500	6.5 ±0.3	1.19 ±0.03	7.3 ±0.1	1.27 ±0.01
7	350 000	500	9.7 ±1.0	1.74 ±0.09	12.3 ±0.3	2.03 ±0.02
7	750 000	1372	10.3 ±.3	1.80 ±0.03	–	–
10	1 500 000	500	17.7 ±0.9	2.89 ±0.07	21.1 ±0.5	3.32 ±0.04
10	750 000	4000	16.7 ±0.6	2.81 ±0.05	–	–
16	500 000	2048	30.2 ±2.0	4.97 ±0.20	39.7 ±0.8	6.13 ±0.05

Table 6.2: Solvent effects on polymer conformation : $r_c = 2.5$

Chain Length	MD				SD	
N	Timesteps	System Size	$< R^2 >$	$< S^2 >$	$< R^2 >$	$< S^2 >$
4	350 000	500	4.53 ±0.08	0.88 ±0.01	4.54 ±0.05	0.877 ±0.005
5	350 000	500	6.3 ±0.2	1.17 ±0.02	6.3 ±0.1	1.17 ±0.01
7	500 000	500	10.3 ±0.4	1.80 ±0.04	9.91 ±0.15	1.76 ±0.02
7	750 000	1372	9.9 ±0.4	1.76 ±0.04	–	–
10	750 000	500	16.5 ±0.3	2.78 ±0.03	16.3 ±0.2	2.75 ±0.02
16	300 000	2048	31.9 ±2.0	4.99 ±0.20	27.8 ±0.3	4.67 ±0.03

Table 6.3: Incorporation of potential of mean force (PMF), T_r=2.0, ρ = 0.7. Effect of cut-off distance.

Chain Length N	PMF $R_c = 2.5$		PMF $R_c = 4.5$	
	$< R^2 >$	$< S^2 >$	$< R^2 >$	$< S^2 >$
4	4.61 ±0.05	0.885 ±0.005	4.65 ±0.05	0.890 ±0.005
5	6.47 ±0.06	1.184 ±0.006	6.57 ±0.06	1.194 ±0.006
7	10.6 ±0.1	1.83 ±0.01	10.9 ±0.2	1.86 ±0.01
10	16.2 ±0.2	2.75 ±0.02	17.8 ±0.5	2.96 ±0.04
16	27.0 ±0.8	4.62 ±0.1	32.1 ±0.8	5.3 ±0.1

unaffected by changing the cut-off distance. The fact that the SD simulation results with $r_c = 2.5$ agree with the MD results is fortuitous and reflects the high temperature at which these runs were performed. A consistent SD formalism would need to capture the invariance evident in MD with changing cut-off distance. The incorporation of a PMF achieves this since the pair correlation function and hence the PMF is determined by the rapidly varying repulsive portion of the potential. Therefore the PMF for LJ_a and LJ_r systems are nearly identical and the correct MD behavior is recovered.

Table 6.3 shows the effect of incorporating the relevant PMF into the SD simulations and the results are inline with the MD results shown in Tables 6.1 and 6.2. The extent of the PMF is considerably longer than the cut-off distance of the solvent. The effect of varying the cut-off distance of the potential of mean force (which has nothing to do with the cut-off of the underlying solvent) are shown in Table 6.3. For short chains ($N < 10$) no effect is visible, however, for longer chain lengths, $R_c = 4.5$ results in an over prediction of the chain dimensions. Incorporation of a PMF into the SD simulations worked equally well at T_r=0.8, $\rho = 0.8$ as shown in Table 6.4, where results from MD, SD including PMF and naive SD are compared. Two naive forms of SD may be envisaged. In the first case LJ_a interactions could be incorporated as shown in Table 6.4. This obviously does not yield the correct structural behaviour. The second case is to incorporate just the LJ_r interactions, yielding the same result as shown in Table 6.1. By comparing the MD results in Tables 6.1 and 6.4 the effect of density is to modestly decrease the conformational volume of the chains. Temperature effects are limited since we are dealing with a theta solvent in which all interactions are equivalent.

Thus far all the work has dealt with chains in a good solvent i.e. all interactions were

Table 6.4: Incorporation of PMF at T_r=0.8, $\rho = 0.8$

Chain Length N	MD		SD-PMF		SD-LJ_a	
	$< R^2 >$	$< S^2 >$	$< R^2 >$	$< S^2 >$	$< R^2 >$	$< S^2 >$
4	4.4 ±0.1	0.85 ±0.01	4.7 ±0.04	0.89 ±0.01	3.73 ±0.02	0.79 ±0.01
5	6.3 ±0.2	1.17 ±0.02	6.8 ±0.05	1.22 ±0.04	4.77 ±0.04	0.99 ±0.01
7	9.5 ±0.4	1.72 ±0.04	11.3 ±0.2	1.91 ±0.02	6.29 ±0.15	1.34 ±0.01
10	18.1 ±0.6	2.94 ±0.06	18.8 ±0.4	3.05 ±0.03	7.62 ±0.24	1.74 ±0.03

Table 6.5: Poor solvent : 1*LJ_a

Chain Length N	MD		PMF	
	$< R^2 >$	$< S^2 >$	$< R^2 >$	$< S^2 >$
4	3.86 ±0.05	0.81 ±0.01	3.98 ±0.29	0.81 ±0.03
5	5.27 ±0.11	1.04 ±0.01	5.38 ±0.29	1.06 ±0.03
7	7.23 ±0.60	1.45 ±0.06	7.15 ±0.33	1.43 ±0.03
10	9.86 ±0.60	1.96 ±0.07	9.02 ±0.70	1.90 ±0.07
16	11.6 ±1.0	2.71 ±0.01	10.28 ±0.57	2.43 ±0.07

equivalent. The utility of using SD-PMF simulations would be the ability to successfully account for chain behavior in solvents of varying quality. Towards this end, a chain of B beads in a solvent of A has been simulated, where B-B interactions are LJ_a while A-B interactions and A-A interactions are LJ_r. This is the simplest scenario where only the interactions among the chain beads is different and therefore the interaction potential is comprised of a direct contribution and the PMF of a LJ_r solvent. The direct contribution is LJ_a in the range $2^{1/6} < r < 2.5$. These results appear in Table 6.5. The PMF results seem to underpredict $< R^2 >$ and $< S^2 >$ by 10 % for chain lengths $n = 16$. Consistent results are also obtained by further increasing the strength of the attractive tail by a factor of two as shown in Table 6.6.

Finally a chain of B beads in a solvent of A has been simulated where A-A and B-B interactions are LJ_a while A-B interactions are LJ_r. In section 6.2.1 we calculated the PMF for such a system using the thermodynamic perturbation technique. These results appear in Table 6.7 and were independent of whether the fitted or predicted form of the PMF was used (Figure 6-2). The SD simulations, including the PMF, consistently underpredicted the chain conformation by about 10 %.

Table 6.6: Very poor solvent : 2*LJ_a

Chain Length N	MD		PMF	
	$< R^2 >$	$< S^2 >$	$< R^2 >$	$< S^2 >$
4	3.39 ±0.16	0.75 ±0.01	3.34 ±0.27	0.74 ±0.03
5	3.82 ±0.21	0.88 ±0.02	3.81 ±0.14	0.88 ±0.03
7	4.81 ±0.32	1.15 ±0.02	4.74 ±0.28	1.14 ±0.02
10	5.40 ±0.66	1.44 ±0.04	5.04 ±0.5	1.40 ±0.03
16	5.68 ±0.47	1.84 ±0.01	5.48 ±0.35	1.78 ±0.04

Table 6.7: LJ chain in incompatible LJ solvent : A-A and B-B interactions are LJ_a and A-B interactions are LJ_r at $T_r = 2.0$ and $\rho = 0.7$

Chain Length N	MD		PMF		% Deviation	
	$< R^2 >$	$< S^2 >$	$< R^2 >$	$< S^2 >$	$< R^2 >$	$< S^2 >$
4	3.63 ±0.10	0.78 ±0.01	3.33 ±0.05	0.74 ±0.01	8	5
5	4.46 ±0.20	0.98 ±0.01	3.97 ±0.02	0.90 ±0.01	11	8
7	5.45 ±0.16	1.26 ±0.01	4.88 ±0.04	1.15 ±0.01	10	9
10	6.57 ±0.25	1.63 ±0.02	5.45 ±0.05	1.44 ±0.01	7	12
16	6.98 ±0.20	2.10 ±0.03	6.15 ±0.07	1.85 ±0.01	12	12

6.5 Interacting Systems

Thus far we have limited our discussion to the incorporation of the PMF in single molecule systems only i.e. systems at infinite dilution. Since we are interested in demonstrating that solvent effects may be accounted for in an approximate manner in the simulation of micelle formation we need to demonstrate the applicability of this technique for multi-molecular/interacting systems.

The structural quantity of interest in self-assembling systems is the fraction of molecules that are associated in a cluster of a certain size ($s\rho_s / \sum s\rho_s$ in the notation introduced in Chapter 4). Towards this end we considered an 864 particle MD system at $T_r = 2.0$, $\rho = 0.7$ in which 108 particles are tagged as being of type 0. All particle interactions are LJ_a and the tagging serves only to follow a certain subset of the particles and to identify clusters that are formed among them. The clustering algorithm used is described in Chapter 3. The MD results were compared to a SD simulation incorporating the PMF, at that same total number density of tagged particles ([S]=0.0875). As can be seen from Figure 6-4 the MD data and SD-PMF data are indistinguishable. A similar run at a lower temperature ($T_r = 1.2$) is shown in Figure 6-5. If SD simulations with LJ_a interactions were performed i.e. if solvent structure is not incorporated in the SD simulation, the naive result shown in Figure 6-5 is obtained. The naive approach overestimates the clustering behaviour. Also, if LJ_r interactions were used in the SD simulations the results would be totally different, despite the fact that no observable change is expected for the MD case. This conclusion is similar to that drawn in section 6.4. The single chain MD results using LJ_r or LJ_a are equivalent since it is the rapidly varying part of the potential that determines the solvent structure.

Next a chain of length 4 was considered in which the beads were of type 0-0-1-1 respectively. The constraints were rigidly imposed using the SHAKE algorithm. Once again, the bead type designation was purely used as a tool to identify clusters and all potential interactions were equivalent (LJ_a). The results are shown in Figure 6-6 at two different chain concentrations. The chain concentrations is defined as : $[S] = N_c \times N_b / V_{sys}$, where N_c = number of chains and N_b = number of beads per chain, and V_{sys} is the simulation volume. The chain concentration is therefore proportional to the volume fraction. Typically 108 chains were simulated in order 3000 solvent molecules. The long range nature of the

PMF (Figure 6-1) is evident in that the results obtained using a PMF cut-off distance of R_c = 2.5 show significant deviation from the MD results. A cut-off distance of R_c = 4.5 showed excellent agreement with the MD results and was able to capture the trend to larger cluster as the concentration was increased from [S]=0.1037 to [S]=0.1555. The results presented thus far are nearly temperature independent since all interactions are equivalent i.e. we are dealing with an athermal system (theta solvent) and was confirmed by simulations at T_r=1.5 and T_r=1.2 (see for example Figures 6-4 and 6-5). In contrast, the naive approach of performing SD with LJ_a interactions gives rise to temperature dependent results.

The case of associating chains was investigated using chains of type A_2B_2 where the hydrophobic B groups were designated as type 0. In the MD simulations, the 0-0 interactions were taken to be LJ_a while all other interactions were LJ_r. The corresponding SD simulations incorporated the solvent contribution via a PMF (at the relevant temperature) while the additional direct contribution for 0-0 interactions is LJ_a for $2^{1/6} < r < 2.5$. Figure 6-7 compares the results obtained for MD, SD including the PMF and finally the naive approach of SD where solvent effects are not incorporated at T_r = 1.5 and [S]=0.1037. The naive approach underestimates the clustering behaviour. It is evident that the incorporation of a PMF is essential to characterise the true system. Structural properties, like the radius of gyration of the clusters, is also recovered if the correct PMF is employed (Figure 6-7(b)). In subsequent comparisons we will not consider SD results that do not include a PMF. The clustering behavior at two temperatures is compared to the MD simulation results in Figure 6-8(a). As the temperature is decreased from T_r = 2.0 to T_r = 1.5 the number of large clusters increases significantly and the SD-PMF results show the same behavior. As is evident from Figure 6-8(b), the MD and SD-PMF results are in excellent agreement even at low aggregation numbers, however even for this example we have not formed a micelle phase.

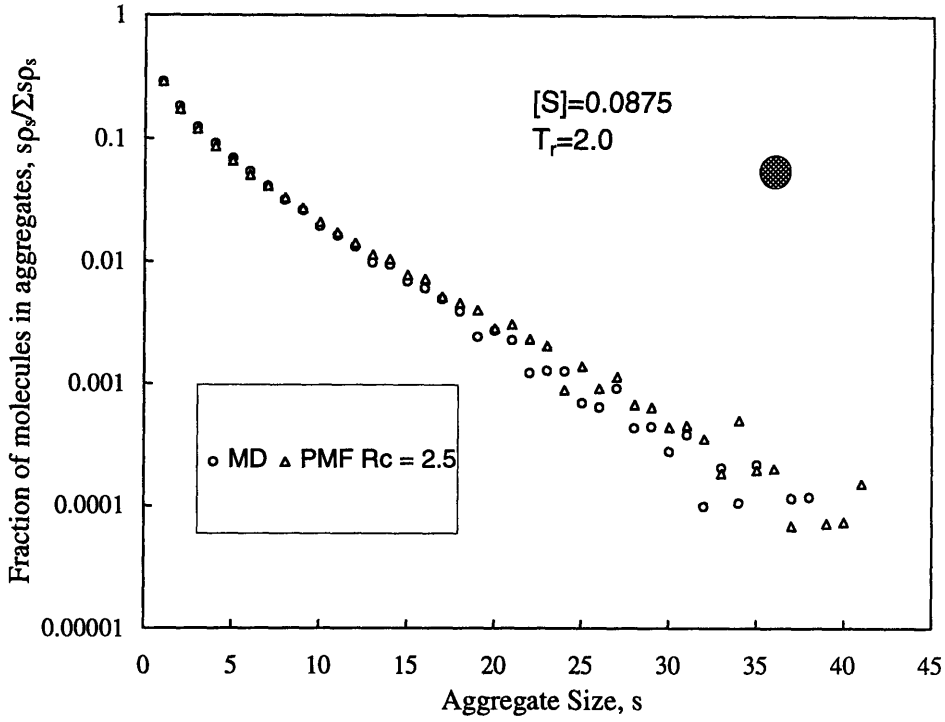

Figure 6-4: Effect of incorporating a PMF in SD simulations to represent the associating behaviour of LJ_a solutes in a LJ_a solvent

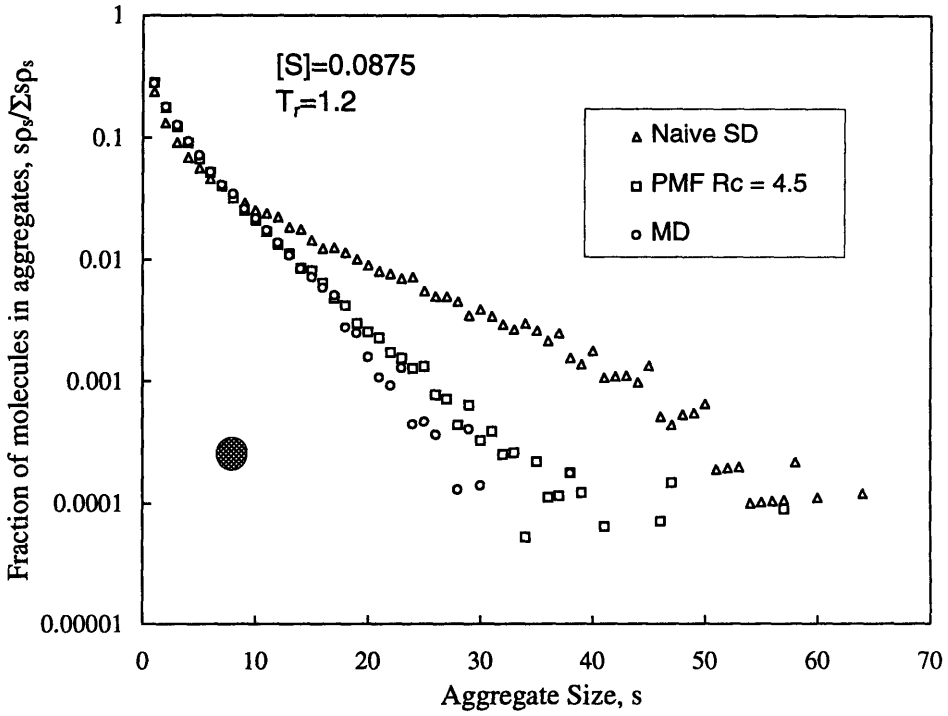

Figure 6-5: Effect of incorporating a PMF in SD simulations to represent the associating behaviour of LJ_a solutes in a LJ_a solvent at $T_r = 1.2$. Also shown is the naive result which would be obtained if the PMF was not included in the SD simulations.

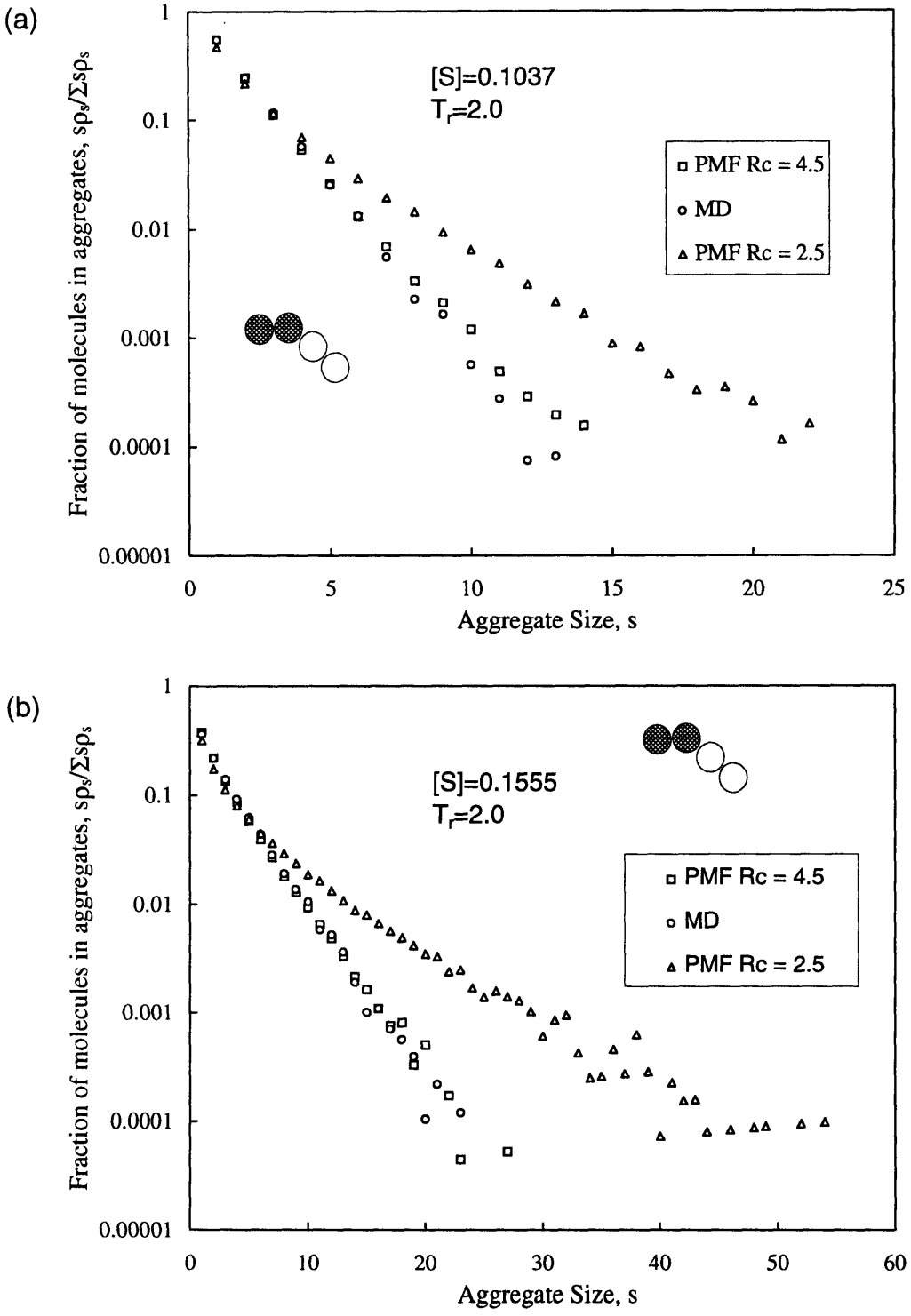

Figure 6-6: Interacting chains of four beads at concentrations (a) [S]=0.1037 (b) [S]=0.1555. A significant effect of the cut-off distance used for the PMF is found. All interactions are equivalent. The shading of the beads indicates that two beads were conceptually tagged so that a cluster could be defined by shaded beads being within a prescribed distance of each other.

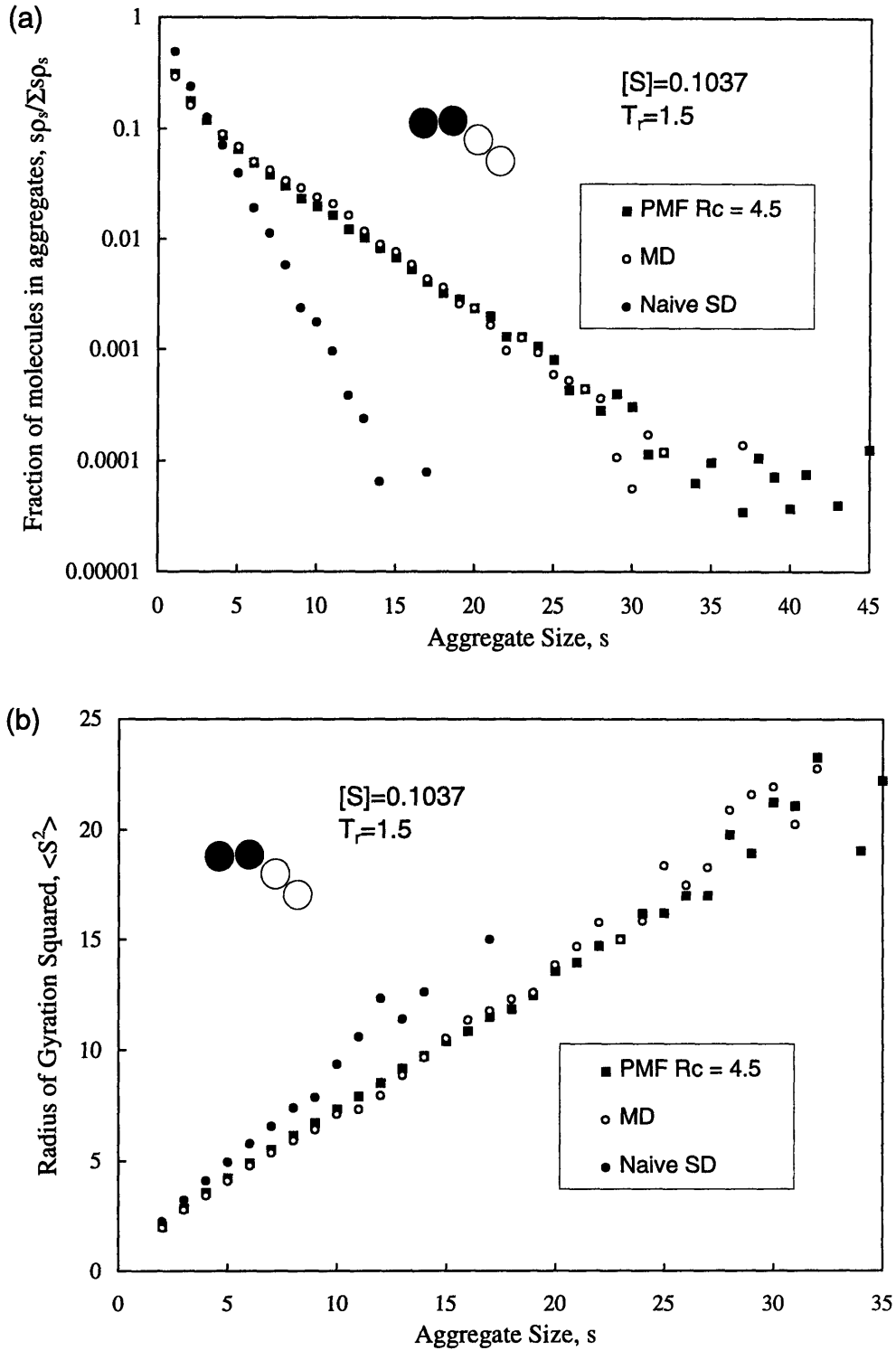

Figure 6-7: (a) Clustering behaviour of associating chains A_2B_2 at $T_r = 1.5$, [S] =0.1037. (b) Radius of gyration of clusters. SD simulations that do not include the relevant PMF are unable to account correctly for the solvent.

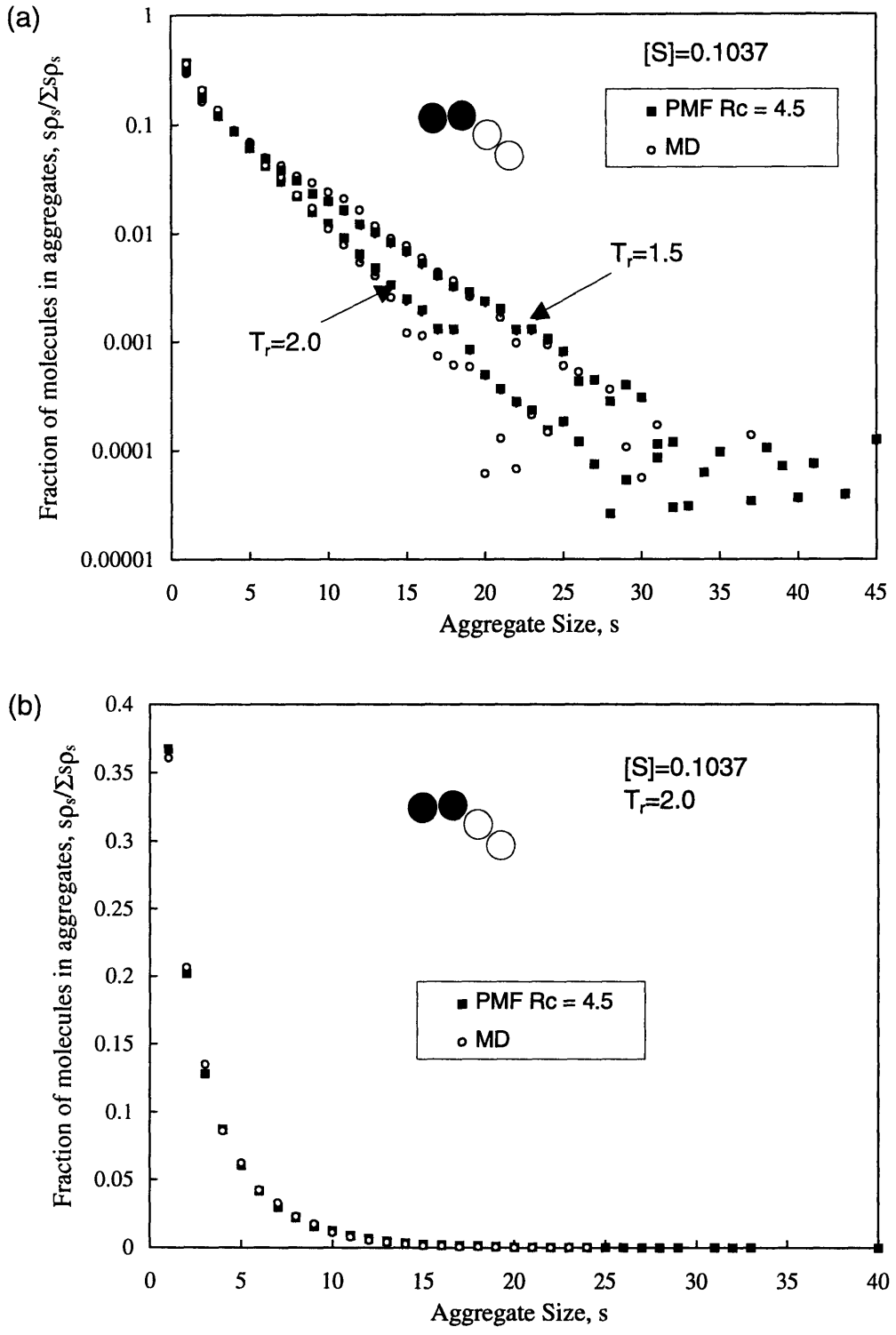

Figure 6-8: (a) Clustering behaviour of associating chains A_2B_2 at two temperatures. (b) Clustering behavior of A_2B_2 at T_r=2.0, [S]=0.1037 on linear axes.

6.6 Conclusion

In order to take solvent effects into account in SD simulations, a potential of mean force which incorporates the solvent contribution is required. For simple LJ systems of varying quality, the inclusion of the appropriate PMF enables SD simulations to reproduce the MD counterpart result for chains of length $N = 4 - 16$. The clustering behaviour of LJ beads and chains in equivalent solvents also appear consistent when using the correct PMF. All results presented were at relatively high temperatures. $T_r = 2.0$ is in effect above the critical temperature for a LJ fluid [31]. The success of this approach at lower temperatures and different densities still needs to be established. Preliminary work shows that consistent results are still obtained for $T_r = 0.8$,$\rho = 0.8$.

In order to really evaluate the ability of the PMF to account for solvent effects in micelle solutions, this work must be extended to system where micelles form. An immediate problem that exists is that very long MD runs are required (order weeks) to try to sample even small aggregates and hence direct comparison with MD is difficult. Furthermore, although for the simple test cases shown, a PMF could readily be calculated, in real micellar systems the nature of the solvent-solute and solvent-solvent interactions are vastly different in size, range and orientation. The ability of the superposition approximation to hold for such cases is extremely unlikely. However, for simple cases, as demonstrated by the test cases considered, some solvent effects may be accounted for directly using a PMF.

Bibliography

[1] L. R. Pratt and D. Chandler, J. CHem. Phys. **67,** 3683 (1977).

[2] J. M. Deutch and I. Oppenheim, J. Chem. Phys. **54,** 3547 (1971).

[3] G. Ciccotti and J-P. Ryckaert, J. Statis. Phys. **26,** 73 (1981).

[4] R. M. Levy, M. Karplus, and J. A. McCammon, Chemical Physics Letters **65,** 4 (1979).

[5] L. R. Pratt and D. Chandler, J. CHem. Phys. **73,** 3430 (1980).

[6] A. Giró, E. Guárdia, and J. A. Padró, Molecular Physics **55,** 1063 (1985).

[7] E. Guárdia and J. A Padró, J. Chem. Phys. **83,** 1918 (1985).

[8] E. Guárdia, A. Giró, and J. A Padró, J. Chem. Phys. **84,** 4769 (1986).

[9] R. W. Pastor, R. M. Venable, and M. Karplus, J. Chem. Phys. **89,** 1112 (1988).

[10] P. E. Smith, B. M. Pettitt, and M. Karplus, J. Phys. Chem. **97,** 6907 (1993).

[11] R. W. Pastor and M. Karplus, J. Phys. Chem. **92,** 2636 (1988).

[12] B. M. Pettit, M. Karplus, and P. J. Rossky, J. Phys. Chem. **90,** 6335 (1986).

[13] T. Hill, *Statistical Mechanics*, (DoverPublications Inc., New York, 1987).

[14] Münster, A., *Statistical Mechanics, Volume I*, (Springer-Verlag, Berlin, 1969).

[15] C. Pangali, M. Rao, and B. J. Berne, J. Chem. Phys. **71,** 2975 (1979).

[16] R. W Zwanzig, J. Chem. Phys. **22,** 1420 (1954).

[17] P. Linse, J. Am. Chem. Soc. **115,** 8793 (1993).

[18] G. Hummer and D. K. Soumpasis, Phys. Rev. E **49,** 591 (1994).

[19] M. Pellegrini and S. Doniach, J. Chem. Phys. **103,** 2696 (1955).

[20] M. Madhusoodanan and B. L. Tembe, J. Phys. Chem. **98,** 7090 (1994).

[21] E. Guàrdia, R. Rey, and J. A. Padró, Chemical Physics **155,** 187 (1991).

[22] M. P. Allen and D. J. Tildesley, *Computer Simulations of Liquids*, (Oxford Science Publications, Oxford Press, 1992).

[23] J. M. Haile, *Molecular Dynamics Simulations : Elementary Methods*, (John Wiley & Sons, INC, New York, 1992).

[24] D. C. Rapaport, J. Phys. A:Math. Gen. **11,** L213 (1978).

[25] D. C. Rapaport, J. Chem. Phys. **71,** 3299 (1979).

[26] M. Bishop, M. H. Kalos, and H. L. Frisch, J. Chem. Phys. **70,** 1299 (1979).

[27] W. Bruns and R. Bansal, J. Chem. Phys. **74,** 2067 (1981).

[28] P. G. Khalatur, Y. G. Papulov, and A.S. Pavlov, Molecualr Physics **58,** 887 (1986).

[29] B. Smit, K. R. Cox, and J. P. J. Michels, Molecualr Physics **66,** 97 (1989).

[30] J. Luque, J. Santamaria, and J. J. Freire, J. Chem. Phys. **91,** 584 (1989).

[31] B. Smit, J. Chem. Phys. **96,** 8639 (1992).

Part II

Interfacial Instability Associated with Interfacial Chemical Reactions

Chapter 7

Normal Mode Stability Analysis

7.1 Summary

When an aqueous solution of cetyltrimethylammonium bromide is contacted with a nitrobenzene solution containing picric acid, large scale motion of the interface is sometimes observed, accompanied by interfacial electrical potential oscillations with a period of order 3-10 seconds. This behaviour has been interpreted using a stability analysis on a two phase system (α,β) in which a solute $\mathcal{A}$ (in phase α) diffuses to the interface where it reacts with solute $\mathcal{B}$ (from phase β) to form product $\mathcal{P}$. Kinetics of the surface reaction are assumed to be infinitely fast. The stability of the system was analysed with respect to small perturbations in the spirit of normal mode stability analysis. Both oscillatory and stationary regimes were identified. For the simplified case in which component $\mathcal{A}$ is insoluble in phase β and components $\mathcal{B}$ and $\mathcal{P}$ are insoluble in phase α, the presence of three diffusing components considerably modifies the stability criteria relative to those for the diffusion of a single component across the interface. Over a narrow concentration range, an oscillatory instability with a period of order one second is predicted. This compares well with observed experimental results.

7.2 Introduction

Much experimental and theoretical work has been devoted to the development of an explanation for the interfacial turbulence that is frequently observed during heat or mass transfer across an interface. This work is of great importance to the chemical industry since interfa-

cial instability may increase the rate of mass transfer across an interface considerably. This has led to extensive work in the past four decades to develop criteria for interfacial stability. Due to the complexity of the systems, results have been qualitative in nature. Despite this complexity, these systems are now well understood.

7.3 Historical Review

The name of Italian physicist, Carlo Marangoni has become synonymous with motion and instability at fluid interfaces. The motion is caused by variations of interfacial tension that result from local variations in composition or temperature. This phenomenon is commonly referred to as the Marangoni effect. An in-depth and interesting historical review is provided by Scriven and Sternling [1].

Although the ideas of interfacial flows had been used to explain the tears of strong wine as early as 1855, the first theoretical analysis dealing with interfacial flows was performed by Pearson [2]. The analysis was performed in an attempt to explain the cellular convective patterns observed in drying paint films. Similar convective patterns were seen by H. Bénard on heating a thin layer of molten spermaceti[1] from below. This behaviour was initially ascribed to buoyancy; but, by performing a linear stability analysis, Pearson was able to show that above a critical value of B (ratio of surface tension to viscous forces) instability will occur due to interfacial flow. The analysis, although based on temperature variations, is completely analogous for concentration variations. Only the neutral stability curves were obtained (solutions which neither decay nor are amplified). Berg and Acrivos [3] extended Pearson's analysis to include the presence of surface active agents which impart both viscous and elastic properties to the interface. The surface viscosity resists motion in the film analogous to motion in a Newtonian fluid. This modifies the boundary condition at the free surface. The presence of surfactants was shown to increase the critical value of B by 3 to 4 orders of magnitude, thus inhibiting instability. This is in agreement with experimental results. Deformation of the interface was included by Scriven and Sternling [4]. They found that, for infinitely deep phases, there is no critical Marangoni number for the onset of stationary instability and that the limiting case of zero wave-number is always unstable. Also, it was found that the high surface tension limit yields unphysical results only at small

[1] spermaceti-white waxy substance contained in the head of sperm whale, used for candles and ointments

wave-numbers (i.e. large wavelength). Constraining the interface to be flat was found to have a stabilizing influence. Although this constraint leads to unphysical behaviour at low wave-numbers the assumption may be justified in many problems due to the simplifications introduced into the problem. The effect of gravity waves was also included [5] and shown to be important only at very small wave-numbers, in very thin films, and in extremely viscous fluids. Generally it appears that these effects may be neglected. Furthermore, Smith showed that for many situations the critical value of the Marangoni number is equivalent to the case of a non-deformable interface.

An analogous situation exists for concentration gradients and was analysed in detail by Sternling and Scriven [6] for the diffusion of a single component across an interface separating two infinitely deep immiscible fluids. Fourier perturbations were introduced in the linearized conservation equations and an implicit characteristic equation obtained. The characteristic equation relates the wave-number to the growth constant of the disturbance. Oscillatory as well as stationary instability was considered. Surface viscosity (shear and dilational) was included in the derivation of the characteristic equation. They concluded that, if the solute lowers surface tension, instability will occur for a certain range of wave-numbers if solute transfer is out of the phase of higher viscosity or lower diffusivity.

Rukenstein and Berbente [7] extended the work of Sternling and Scriven [6] by considering a solute $\mathcal{A}$ that reacts while diffusing in one of the phases to form a product $\mathcal{P}$. $\mathcal{A}$ and $\mathcal{P}$ are also soluble in both phases. Following a very similar analysis to Sternling and Scriven they demonstrated that even for very small rate constants the criteria for stability are modified.

At this stage, experimental measurements of the critical Marangoni number were found to be several orders of magnitude greater than those obtained from theoretical predictions. In an attempt to explain this discrepancy, Brian [8] included the effect of Gibbs adsorption in the concentration analog of Pearson's work and showed that surface convection has a profoundly stabilizing influence. In addition the critical Marangoni number tended to infinity for a critical value of the "adsorption number". Physically this stabilizing effect may be attributed to dilution of solute molecules in an expanding interface resulting in a higher surface tension which opposes further motion. For a contracting interface the solute is concentrated and reduces the surface tension thus preventing further contraction. In addition it was shown that the effect of surface diffusion is very much smaller than

the effect of surface convection. Brian and Smith [9] also concluded that no physically meaningful oscillatory modes of instability exist in this system.

Very few other works have included either oscillatory modes or non-zero growth rates in their analysis. This is because, as one tries to increase the complexity of the problem (including surface and gravity waves, electrostatics, and surface deformation), the problem is no longer analytically tractable. A qualitative understanding of many problems can be obtained simply by considering the neutral stability problem (growth rate set to zero) and this is commonly done in the literature.

Since the early 1970's, the field has been dominated by work of Sanfeld and his coworkers. This has been restricted to finding the neutral stability curves. They considered the influence of autocatalytic trimolecular reactions at an interface [10]. Components were in instantaneous equilibrium with the underlying bulk phases and diffusion in the bulk was neglected. Later [11] this analysis was extended to two fluctuating species where adsorption-desorption steps and the surface chemical reaction were the rate determining steps. This assumption implies that the interfacial sublayer is in instantaneous equilibrium with the corresponding bulk phase. Electrostatics were also included [12] and some work has been done on non-planar interfaces. For further details see their extensive review article [13].

Interfacial instability may also occur due to the absorption of a gas into a liquid film. Sakata and Funada [14] considered the absorption of a single component into a liquid film where it reacts to form a non-volatile product $\mathcal{P}$. Once again it was shown that surface deformation plays a role only at small wave-numbers. This analysis was extended [15] to include a solute $\mathcal{B}$ that reacts with the absorbed gas $\mathcal{A}$ to form a product $\mathcal{P}$.

A series of three papers dealt with the instability due to the transfer of matter across a deformable interface [16, 17, 18]. Oscillatory modes were included. Effects of surface diffusion, gravity, a deformable interface and exponential concentration profiles in the bulk phases did not change the results of Sternling and Scriven [6]. The only deviations were seen for very low surface tension (less than 1 dyne/cm) and for exponential concentration profiles. The authors proposed that the instability at low surface tension may explain the process of spontaneous emulsification [19]. Their's is a rather exhaustive piece of work and clearly shows that the assumptions of Sternling and Scriven do not affect the results obtained. In addition the results were related to the experimental results of Orell and Westwater [20] for ethylene glycol/ethylene acetate system in which acetic acid is used as the diffusing solute.

Surprisingly good agreement was obtained.

The effect of electrical forces on interfacial stability, including ion interactions [21], dipole interactions [22] and the effect of electrical double layers [23] have been studied.

7.4 Motivation

While the aforementioned studies have shed much light on the factors affecting interfacial stability, there are still many experimental observations that cannot yet be interpreted successfully using available results.

A case in point is the work of Nakache *et al.* [24, 25], who observed motion at an interface between an aqueous solution of cetyltrimethylammonium chloride (CTA^+Cl^- or $C_{16}^+Cl^-$) and an oil phase (nitrobenzene) containing picric acid (H^+Pi^-). They monitored oscillations in the pH, surface tension and electrical potential across the interface. We have obtained similar experimental results using 5 mM cetyltrimethylammonium bromide as the surfactant. Typical potential measurements across such an interface for a picric acid concentration of 1.5 mM are shown in Figure 1. Physical motion was observed in and normal to the plane of the interface, with periodically contracting and twitching cell-like structures at the interface (1-5 mm size range). A detailed experimental study of chemically driven non-linear waves and oscillations at an oil-water interface has also been reported by Kai *et al.* [26, 27]. The solutes were trimethyl stearyl ammonium chloride (in water) and iodine (in nitrobenzene). A commonly reported feature of this work is that the observed instabilities occur only in a narrow concentration range (of all species present), and only when the oil phase is slightly polar, so that picric acid (or equivalent) can exist in a dissociated form.

These instabilities cannot be explained using conventional stability criteria [28], since the surface active component is diffusing from the phase of higher diffusivity and lower viscosity to the phase with higher viscosity and lower diffusivity, conditions which favour stability according to the analysis of Sternling and Scriven. Nakache and Dupeyrat attempted to explain the phenomenon using a surface 'exchange' reaction as the CTA^+ ion moved into the oil phase to become the counterion of picrate ion:

$$C_{16}^+Cl^-{}_{water} + H^+Pi^-{}_{nitrobenzene} \rightleftharpoons C_{16}^+Pi^-{}_{nitrobenzene} + H^+Cl^-{}_{water} \qquad (7.1)$$

The rather exhaustive study of Sanfeld *et al.* [13] intimates that the observed instability

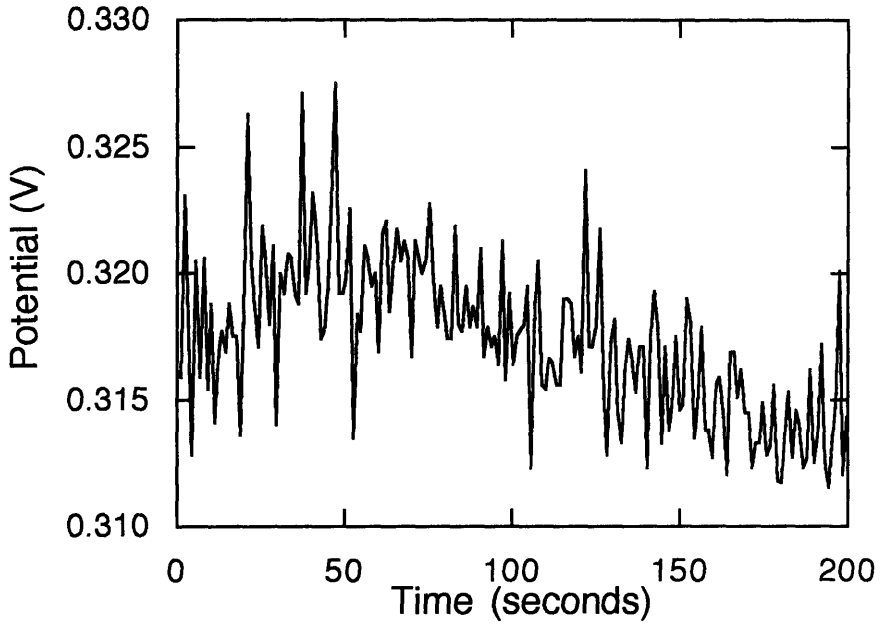

Figure 7-1: Potential variations across nitrobenzene-water interface with $[CTA^+Br^-]_{\text{water}}$ = 5mM, $[H^+Pi^-]_{\text{nitrobenzene}}$ = 1.5mM.

could possibly be explained by electrostatic effects at the interface. The maximum wavelength was found to be rather large at approximately 5 cm. Experimentally, however, it has been shown that surface motion is observed when potassium iodide (KI) is substituted for the picric acid (using CTA^+Cl^- as the surfactant), but that the system is stable when potassium bromide (KBr) is used [28]. Since KI and KBr have similar charge effects it seems unlikely that electrostatics are responsible for this behaviour. In addition, Sanfeld *et al.* [13] assumed that the adsorption/desorption steps are rate limiting and not diffusion in the bulk phases. Several authors have noted, however, that the potential energy barrier associated with the kinetics of adsorption/desorption phenomena of long chain molecules is very small [19], so that the transfer of these solutes is often controlled by diffusion. In particular, the adsorption of hexadecyltrimethylammonium bromide has been shown to be diffusion controlled at air-water and oil-water interfaces [29, 30]. Thus it would appear that the Sanfeld *et al.* [13] analysis is not entirely relevant for the interpretation of the experimentally observed surface oscillations discussed above.

In this chapter, we have used a normal mode stability analysis to explain the observed phenomenon based on simple diffusion/convection accompanied by an exchange reaction at the interface.

7.5 System under Study

We consider two semi-infinite liquid phases (α and β) in contact along a planar interface. A solute $\mathcal{A}$ in phase α diffuses to the interface where it reacts instantaneously at the interface with a component $\mathcal{B}$ to form a product $\mathcal{P}$ according to the reaction

$$\mathcal{A} + \mathcal{B} \rightleftharpoons \mathcal{P}$$

This reaction is characterized by the equilibrium constant

$$K_{eq} = \frac{C_P}{C_A C_B}$$

A schematic of the system, showing local equilibrium concentration profiles, is presented in Figure 2.

The interface is considered to be non-deformable. It has been shown that inclusion

of surface viscosity, surface diffusion and a deformable interface in a stability analysis for a single diffusing component gives results that compare well with those of Sternling and Scriven [16, 17, 18]. The constraint of a flat interface led to greater stability only at large wavelengths [4]. It is also assumed that the adsorption step and reaction kinetics are fast and diffusion is the rate limiting step, in accord with the observations recorded by Davies and Rideal [19], and the experimental measurements of van Hunsel *et al.* [29].

The theoretical development closely follows the pioneering work of Sternling and Scriven [6] and Ruckenstein and Berbente [7] to which the reader is referred for more detail. Sternling and Scriven [6] considered the diffusion of a single non-reactive surface active component across an interface. Ruckenstein and Berbente [7] extended this analysis to the case of diffusion across an interface accompanied by a chemical reaction within one of the bulk phases.

The stability of the system is analysed with respect to small two-dimensional perturbations. A single Fourier component suffices since any disturbance can be represented by superposition of such components. The objective of the analysis is to determine a relationship between the wavelength and growth rate of the disturbance.

7.6 Stability Analysis

7.6.1 Hydrodynamics

In each phase, the Navier Stokes and continuity equations can be written as

$$\rho \frac{D\mathbf{v}}{Dt} = -\nabla P + \mu \nabla^2 \mathbf{v} \tag{7.2}$$

$$\nabla \cdot \mathbf{v} = 0 \tag{7.3}$$

For the 2-dimensional case with the non-linear terms neglected, the pressure term can be eliminated to obtain

$$\frac{\partial^2 v_x}{\partial t \partial y} - \frac{\partial^2 v_y}{\partial t \partial x} = \nu \left(\frac{\partial^3 v_x}{\partial y \partial x^2} + \frac{\partial^3 v_x}{\partial y^3} - \frac{\partial^3 v_y}{\partial x^3} - \frac{\partial^3 v_y}{\partial x \partial y^2} \right) \tag{7.4}$$

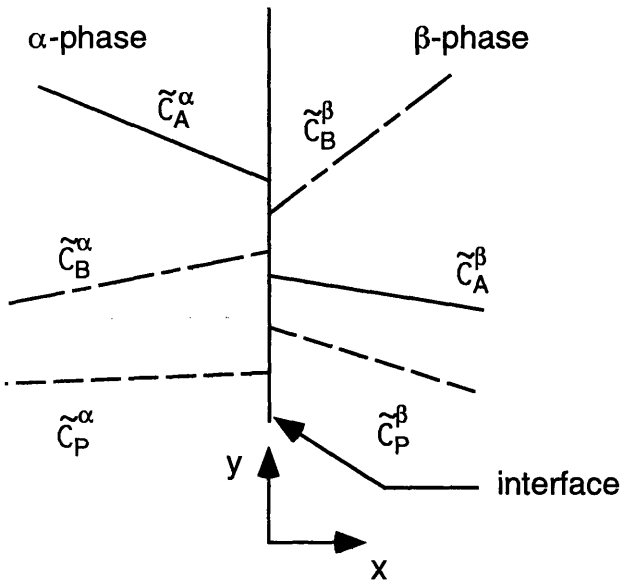

Figure 7-2: Unperturbed concentration profiles near an interface where $\mathcal{A}$ and $\mathcal{B}$ react at the interface to form product $\mathcal{P}$.

It is assumed that perturbations in the velocity can be represented by the equation

$$[v_x^\alpha, v_y^\alpha, v_x^\beta, v_y^\beta] = [U^\alpha(x), V^\alpha(x), U^\beta(x), V^\beta(x)]e^{iky+nt} \tag{7.5}$$

Superscripts indicate the relevant phase, either α or β, while k is the wave-number, which is inversely proportional to the wavelength of the disturbance ($\lambda = 2\pi/k$). The growth rate n, which may be complex, determines the nature of the disturbance. By substituting equation (7.5) into equation (7.4) we can solve for the coefficients of the perturbation. The eight boundary conditions required to evaluate the constants of integration are:

(i)-(iv) The velocity perturbations disappear far away from the interface:

$$\mathbf{v}^\alpha = \mathbf{v}^\beta = 0 \text{ as } x \to \pm\infty$$

(v)-(vi) The normal component of the velocity at the interface must be zero:

$$v_x^\alpha(0, y, t) = v_x^\beta(0, y, t) = 0$$

(vii) There is no slip at the interface:

$$v_y^\alpha(0,y,t) = v_y^\beta(0,y,t)$$

(viii) There must be continuity of the tangential component of the stress. If the interface behaves as a two dimensional Newtonian fluid with dilational viscosity κ and shear viscosity ϵ,then the following expression may be derived [31]:

$$\tau_{xy}^\alpha - \tau_{xy}^\beta = \frac{\partial \sigma_0}{\partial y} + (\kappa+\epsilon)\frac{\partial^2 v_y}{\partial y^2} \text{ at } x = 0$$

where $\tau_{xy}^j = \mu^j(\frac{\partial v_x}{\partial y} + \frac{\partial v_y}{\partial x})$. The two contributions of the surface viscosity are lumped for convenience into a single term $\mu_s = \kappa + \epsilon$.

The continuity equation may be restated in terms of the velocity perturbations in each phase as

$$\frac{dU(x)}{dx} = -ikV(x) \tag{7.6}$$

At this stage it is convenient to introduce the dimensionless coordinates $X = kx$ and $Y = ky$. Solutions for the velocity perturbations are:

for $n \neq 0$

$$\left.\begin{aligned} U^\alpha(X) &= A_1(e^X - e^{p^\alpha X}) \\ V^\alpha(X) &= iA_1(e^X - p^\alpha e^{p^\alpha X}) \end{aligned}\right\} X < 0 \tag{7.7}$$

$$\left.\begin{aligned} U^\beta(X) &= -A_1(\tfrac{1-p^\alpha}{1-p^\beta})(e^{-X} - e^{-p^\beta X}) \\ V^\beta(X) &= iA_1(\tfrac{1-p^\alpha}{1-p^\beta})(e^{-X} - p^\beta e^{-p^\beta X}) \end{aligned}\right\} X > 0 \tag{7.8}$$

for $n = 0$

$$\left.\begin{aligned} U^\alpha(X) &= A_2 X e^X \\ V^\alpha(X) &= iA_2(1+X)e^X \end{aligned}\right\} X < 0 \tag{7.9}$$

$$\left.\begin{aligned} U^\beta(X) &= A_2 X e^{-X} \\ V^\beta(X) &= iA_2(1-X)e^{-X} \end{aligned}\right\} X > 0 \tag{7.10}$$

where $p^j = \sqrt{1 + \frac{n}{k^2 \nu^j}}$. The tangential stress balance yields

$$\frac{\partial \sigma_0}{\partial y}|_{x=0} = 2\mu^\alpha ikA_2(1 + \frac{\mu^\beta}{\mu^\alpha} + \frac{\mu^s k}{2\mu^\alpha})e^{iky}, \text{ for } n = 0 \tag{7.11}$$

and

$$\frac{\partial \sigma_0}{\partial y}|_{x=0} = \mu^\alpha ikA_1(1 - p^\alpha)\{(1 + p^\alpha) + \frac{\mu^\beta}{\mu^\alpha}(1 + p^\beta) + \frac{\mu^s k}{\mu^\alpha}\}e^{iky+nt}, \text{ for } n \neq 0 \tag{7.12}$$

Expressions (7.11) and (7.12) differ from those obtained by Sternling and Scriven by a factor of $-ik$ on the right hand side, since Sternling and Scriven chose to introduce perturbations in the stream function, while in this analysis perturbations were introduced directly in the velocity terms.

The only outstanding variable to be calculated is $\frac{\partial \sigma_0}{\partial y}$. If surface tension is a function solely of the concentrations of species $\mathcal{A}$ and $\mathcal{P}$ at the interface, we can write

$$\frac{\partial \sigma_0}{\partial y}|_{x=0} = (\frac{\partial \sigma_0}{\partial C_A^\alpha})\frac{\partial C_A^\alpha}{\partial y}|_{x=0} + (\frac{\partial \sigma_0}{\partial C_P^\beta})\frac{\partial C_P^\beta}{\partial y}|_{x=0} = \zeta(\frac{\partial C_A^\alpha}{\partial y}|_{x=0} + \omega\frac{\partial C_P^\beta}{\partial y}|_{x=0}) \tag{7.13}$$

where

$$\zeta = \frac{\partial \sigma_0}{\partial C_A^\alpha}, \quad \omega = \frac{1}{\zeta}\frac{\partial \sigma_0}{\partial C_P^\beta}$$

The variables ζ and ω are physical constants of the system. If ζ is negative, component $\mathcal{A}$ is said to be surface active. Some substances, for examples sugars and salts, may increase the surface tension with increasing concentration, which leads to positive values of ζ. The variables ζ and ω may be obtained experimentally.

To determine the concentration distributions of all the components, a mass balance needs to be performed for each component.

7.6.2 Mass Balance

To find the concentration distribution in the perturbed state, we start with the diffusion equation.

$$\frac{DC_i^j}{Dt} = D_i^j \nabla^2 C_i^j \tag{7.14}$$

where subscript i refers to the species type ($\mathcal{A}$,$\mathcal{B}$ or $\mathcal{P}$) while j refers to the relevant phase (α, β). Perturbations of the form

$$C_i^j = \tilde{C}_i^j(x) + H_i^j(x)e^{iky+nt} \tag{7.15}$$

are introduced, where $\tilde{C}_i^j(x)$ represents the unperturbed concentration profiles. These steady state profiles are presented in Figure 2 and are obtained by solving the steady state diffusion equation for each component in each phase. A total of 12 arbitrary constants are introduced in the description of these linear profiles, and must be evaluated using the boundary conditions:

(i)-(iii) The phases are in thermodynamic equilibrium at the interface:

$$m_A C_A^\alpha = C_A^\beta$$
$$C_B^\alpha = m_B C_B^\beta$$
$$C_P^\alpha = m_P C_P^\beta$$

The asymmetric definition of the partition coefficients is unusual, but is selected to ensure that $0 \leq m_i < 1$ for the situation of interest to us. In the limit as the partition coefficients tend to zero ($m_i \to 0$), component $\mathcal{A}$ becomes insoluble in phase β and components $\mathcal{B}$ and $\mathcal{P}$ insoluble in phase α. This limit, it is thought, corresponds to the experimental system of Nakache and Dupeyrat.

(iv)-(v) Storage and diffusion within the interface are neglected, so the flux conditions at the interface are:

$$-D_A^\alpha \frac{\partial C_A^\alpha}{\partial x}|_{x=0} + D_A^\beta \frac{\partial C_A^\beta}{\partial x}|_{x=0} = -D_P^\beta \frac{\partial C_P^\beta}{\partial x}|_{x=0} + D_P^\alpha \frac{\partial C_P^\alpha}{\partial x}|_{x=0}$$
$$-D_B^\alpha \frac{\partial C_B^\alpha}{\partial x}|_{x=0} + D_B^\beta \frac{\partial C_B^\beta}{\partial x}|_{x=0} = -D_P^\beta \frac{\partial C_P^\beta}{\partial x}|_{x=0} + D_P^\alpha \frac{\partial C_P^\alpha}{\partial x}|_{x=0}$$

(vi) Chemical equilibrium at the interface:

$$K_{eq} = \frac{C_P^\beta}{C_A^\alpha C_B^\beta}|_{x=0}$$

(vii)-(xii) The remaining six degrees of freedom may be specified and characterize the unperturbed system uniquely. The following assignments are convenient:

$$\begin{aligned} \tilde{C}_A^\alpha|_{x=0} &= C_{A0}, \quad \tilde{C}_B^\beta|_{x=0} = C_{B0} \\ \frac{\partial \tilde{C}_A^\alpha}{\partial x}|_{x=0} &= Q_A^\alpha, \quad \frac{\partial \tilde{C}_B^\alpha}{\partial x}|_{x=0} = Q_B^\alpha \\ \frac{\partial \tilde{C}_P^\alpha}{\partial x}|_{x=0} &= Q_P^\alpha, \quad \frac{\partial \tilde{C}_A^\beta}{\partial x}|_{x=0} = Q_A^\beta \end{aligned}$$

The conditions of chemical equilibrium at the interface and conservation of mass yield steady state concentration profiles of the form:

$$\left.\begin{aligned} \tilde{C}_A^\alpha &= C_{A0} + Q_A^\alpha x \\ \tilde{C}_B^\alpha &= m_B C_{B0} + Q_B^\alpha x \\ \tilde{C}_P^\alpha &= m_P K_{eq} C_{A0} C_{B0} + Q_P^\alpha x \end{aligned}\right\} x < 0 \tag{7.16}$$

$$\left.\begin{aligned} \tilde{C}_A^\beta &= m_A C_{A0} + Q_A^\beta x \\ \tilde{C}_B^\beta &= C_{B0} + \tfrac{1}{D_B^\beta}(-D_A^\alpha Q_A^\alpha + D_A^\beta Q_A^\beta + D_B^\alpha Q_B^\alpha)x &&= C_{B0} + S_B^\beta x \\ \tilde{C}_P^\beta &= K_{eq} C_{A0} C_{B0} + \tfrac{1}{D_P^\beta}(D_A^\alpha Q_A^\alpha - D_A^\beta Q_A^\beta + D_P^\alpha Q_P^\alpha)x &&= K_{eq} C_{A0} C_{B0} + S_P^\beta x \end{aligned}\right\} x > 0 \tag{7.17}$$

The steady state profiles are distinguished by a tilde and the variables S_B^β, S_P^β denote the slopes of the steady state profiles of components $\mathcal{B}$ and $\mathcal{P}$ in phase β. Using equations (7.14) and (7.15) and neglecting all second order terms in the perturbation variables, we obtain a second order differential equation in H_i in each phase j:

$$\frac{d^2 H_i^j}{dX^2} - H_i^j\left(1 + \frac{n}{D_i^j k^2}\right) = \frac{U^j}{D_i^j k}\frac{d\tilde{C}_i^j}{dX} \tag{7.18}$$

The general solution may then be written as

$$H_i^j = A_{1i}^j e^{-q_i^j X} + A_{2i}^j e^{+q_i^j X} + \frac{I_i^j}{D_i^j k}\frac{d\tilde{C}_i^j}{dX} \tag{7.19}$$

where

$$I_i^j = e^{q_i^j X}\int e^{-2q_i^j X}\int e^{q_i^j X} U^j (dX)^2$$

and

$$q_i^j = \sqrt{1 + \frac{n}{D_i^j k^2}}$$

The constants of integration are evaluated using the interfacial boundary conditions, and the requirement that the perturbations vanish at $x = \pm\infty$. We obtain the expressions

$$\frac{dC_A^\alpha}{dy}|_{x=0} = ikH_A^\alpha(0)e^{iky+nt} \tag{7.20}$$

$$\frac{dC_P^\beta}{dy}|_{x=0} = ikH_P^\beta(0)e^{iky+nt} \tag{7.21}$$

where

$$\begin{aligned}
H_A^\alpha(0) &= \frac{-1}{(\theta_2 A+\theta_1 B)P+AB}\{ \\
&\quad (B + P\theta_2)[l_A^\alpha r_A^2(\dot{I}_A^\alpha(0) - q_A^\alpha I_A^\alpha(0)) - l_A^\beta(\dot{I}_A^\beta(0) + q_A^\beta I_A^\beta(0))] \\
&\quad -B[l_P^\beta r_P^2(\dot{I}_P^\beta(0) + q_P^\beta I_P^\beta(0)) - l_P^\alpha(\dot{I}_p^\alpha(0) - q_P^\alpha I_P^\alpha(0))] \\
&\quad +P\theta_2[l_B^\beta r_B^2(\dot{I}_B^\beta(0) + q_B^\beta I_B^\beta(0)) - l_B^\alpha(\dot{I}_B^\alpha(0) - q_B^\alpha I_B^\alpha(0))]\} \\
H_P^\beta(0) &= \frac{-D_A^\beta}{D_p^\alpha[(\theta_2 A+\theta_1 B)P+AB]}\{ \\
&\quad -(\theta_2 A + \theta_1 B)[l_P^\beta r_P^2(\dot{I}_P^\beta(0) + q_P^\beta I_P^\beta(0)) - l_P^\alpha(\dot{I}_p^\alpha(0) - q_P^\alpha I_P^\alpha(0))] \\
&\quad +\theta_1 B[l_A^\alpha r_A^2(\dot{I}_A^\alpha(0) - q_A^\alpha I_A^\alpha(0)) - l_A^\beta(\dot{I}_A^\beta(0) + q_A^\beta I_A^\beta(0))] \\
&\quad -\theta_2 A[l_B^\beta r_B^2(\dot{I}_B^\beta(0) + q_B^\beta I_B^\beta(0)) - l_B^\alpha(\dot{I}_B^\alpha(0) - q_B^\alpha I_B^\alpha(0))]\}
\end{aligned} \tag{7.22}$$

and

$$\theta_1 = \frac{KeqC_{B0}D_P^\alpha}{D_A^\beta}, \qquad \theta_2 = \frac{KeqC_{A0}D_P^\alpha}{D_B^\alpha}$$

$$r_A^2 = \frac{D_A^\alpha}{D_A^\beta}, \qquad r_B^2 = \frac{D_B^\beta}{D_B^\alpha}$$

$$r_P^2 = \frac{D_P^\beta}{D_P^\alpha}$$

$$l_A^j = \frac{1}{D_A^j k^2}\frac{d\tilde{C}_A^j}{dx}|_{x=0}, \qquad l_B^j = \frac{D_B^\alpha}{D_A^\beta D_B^j k^2}\frac{d\tilde{C}_B^j}{dx}|_{x=0}$$

$$l_P^j = \frac{D_P^\alpha}{D_A^\beta D_P^j k^2}\frac{d\tilde{C}_P^j}{dx}|_{x=0}$$

$$A = (r_A^2 q_A^\alpha + m_A q_A^\beta), \quad B = (r_B^2 q_B^\beta + m_B q_B^\alpha)$$

$$P = (m_P q_P^\alpha + r_P^2 q_P^\beta)$$

We can now relate the growth rate (n) to any wave-number (k) through an expression commonly referred to as the characteristic equation.

7.6.3 General Form of the Characteristic Equation

The characteristic equation is obtained by substituting equations (7.20),(7.21), and (7.22), into (7.12) and (7.13). The dimensionless growth constant G and wave-number W are defined as

$$G = (\frac{\mu^\alpha}{\zeta Q_A^\alpha})n, \quad \text{and} \quad W = (\frac{\nu^\alpha \mu^\alpha}{\zeta Q_A^\alpha})k^2$$

The wave-number W is the inverse of the Marangoni number (usually written with D_i replacing the kinematic viscosity) more commonly used in stability analyses involving surface driven flows. The only characteristic length in this problem is the wavelength of the disturbance since in this analysis it is assumed that the liquid layers extend to infinity.

The characteristic equation may be written as

$$
\begin{aligned}
G = \; & \frac{1}{[1+p^\alpha+\frac{\mu^\beta}{\mu^\alpha}(1+p^\beta)+\frac{\mu^s k}{\mu^\alpha}][(\theta_2 A+\theta_1 B)P+AB]}\times \\
& [\frac{D_A^\alpha}{D_A^\beta}\{B(1+\frac{\omega D_A^\beta}{D_P^\alpha}\theta_1)+P\theta_2\}\{\frac{q_A^\alpha-1}{q_A^\alpha+p^\alpha}-\frac{Q_A^\beta}{Q_A^\alpha r_A^2}\frac{q_A^\beta-1}{q_A^\beta+p^\beta}\}+ \\
& \theta_2\frac{D_B^\beta}{D_A^\beta}\frac{S_B^\beta}{Q_A^\alpha}(P-\frac{\omega D_A^\beta}{D_P^\alpha}A)\{\frac{q_B^\beta-1}{q_B^\beta+p^\beta}-\frac{Q_B^\alpha}{S_B^\beta r_B^2}\frac{q_B^\alpha-1}{q_B^\alpha+p^\alpha}\}- \\
& \frac{D_P^\beta}{D_A^\beta}\frac{S_P^\beta}{Q_A^\alpha}\{(1+\frac{\omega D_A^\beta}{D_P^\alpha}\theta_1)B+\frac{\omega D_A^\beta}{D_P^\alpha}\theta_2 A\}\{\frac{q_P^\beta-1}{q_P^\beta+p^\beta}-\frac{Q_P^\alpha}{S_P^\beta r_P^2}\frac{q_P^\alpha-1}{q_P^\alpha+p^\alpha}\}],\;\; n\neq 0
\end{aligned}
\tag{7.23}
$$

$$
\begin{aligned}
W = \; & \frac{r_A^2}{d^2[1+p^\alpha+\frac{\mu^\beta}{\mu^\alpha}(1+p^\beta)+\frac{\mu^s k}{\mu^\alpha}][(\theta_2 A+\theta_1 B)P+AB]}\times \\
& [\{B(1+\frac{\omega D_A^\beta}{D_P^\alpha}\theta_1)+P\theta_2\}\{\frac{1}{(q_A^\alpha+1)(q_A^\alpha+p^\alpha)}-\frac{Q_A^\beta}{Q_A^\alpha}\frac{1}{(q_A^\beta+1)(q_A^\beta+p^\beta)}\}+ \\
& \theta_2\frac{S_B^\beta}{Q_A^\alpha}(P-\frac{\omega D_A^\beta}{D_P^\alpha}A)\{\frac{1}{(q_B^\beta+1)(q_B^\beta+p^\beta)}-\frac{Q_B^\alpha}{S_B^\beta}\frac{1}{(q_B^\alpha+1)(q_B^\alpha+p^\alpha)}\}- \\
& \frac{S_P^\beta}{Q_A^\alpha}\{(1+\frac{\omega D_A^\beta}{D_P^\alpha}\theta_1)B+\frac{\omega D_A^\beta}{D_P^\alpha}\theta_2 A\}\{\frac{1}{(q_P^\beta+1)(q_P^\beta+p^\beta)}-\frac{Q_P^\alpha}{S_P^\beta}\frac{1}{(q_P^\alpha+1)(q_P^\alpha+p^\alpha)}\}],\;\; n\neq 0
\end{aligned}
\tag{7.24}
$$

$$
\begin{aligned}
W = \; & \frac{r_A^2}{8d^2[1+\frac{\mu^\beta}{\mu^\alpha}+\frac{\mu^s k}{2\mu^\alpha}][(\theta_2(r_A^2+m_A)+\theta_1(r_B^2+m_B))(r_P^2+m_P)+(r_A^2+m_A)(r_B^2+m_B)]}\times \\
& [\{(r_B^2+m_B)(1+\frac{\omega D_A^\beta}{D_P^\alpha}\theta_1)+(r_P^2+m_P)\theta_2\}\{1-\frac{Q_A^\beta}{Q_A^\alpha}\}+ \\
& \theta_2\frac{S_B^\beta}{Q_A^\alpha}((r_P^2+m_P)+\frac{\omega D_A^\beta}{D_P^\alpha}(r_A^2+m_A))\{1-\frac{Q_B^\alpha}{S_B^\beta}\}- \\
& \frac{S_P^\beta}{Q_A^\alpha}\{(1+\frac{\omega D_A^\beta}{D_P^\alpha}\theta_1)(r_B^2+m_B)+\frac{\omega D_A^\beta}{D_P^\alpha}\theta_2(r_A^2+m_A)\}\{1-\frac{Q_P^\alpha}{S_P^\beta}\}],\;\; n=0
\end{aligned}
\tag{7.25}
$$

where $d=\sqrt{D_A^\alpha/\nu^\alpha}$. It should be realised that equations (7.23) and (7.24) are equivalent and contain the same information.

The goal of this work, to generate an equation that relates the wavelength of the disturbance to the growth factor, has been achieved in equation (7.23). The characteristic equation is implicit in the dependent variable n, and hence for a particular wave-number we cannot simply obtain the complex growth constant. This difficulty was encountered by Sternling and Scriven [6], and was overcome by parameterizing equations (7.23) and (7.24) with a new independent variable ξ. Analysis of the characteristic equation in its parametric form is simplified if the surface viscosity is neglected. The surface viscosity has been shown [1] to render the interface more stable, especially at large wave-numbers, and can be incorporated readily through numerical solution of equation (7.23).

Before proceeding with an analysis of the characteristic equation, it is desirable to consider a number of limiting cases. In the limit as the variables K_{eq}, Q_B^α, Q_P^α, S_B^β, S_P^β, ω tend to zero, the problem reduces to that analysed by Sternling and Scriven [6]. The

expressions that are obtained,

$$G = -\frac{\frac{q_A^\beta - 1}{q_A^\beta + p^\beta} - \frac{q_A^\alpha - 1}{q_A^\alpha + p^\alpha}}{(1 + p^\alpha + \frac{\mu^\beta}{\mu^\alpha}(1 + p^\beta) + \frac{\mu^s k}{\mu^\alpha})(\frac{m_A}{r_A^2} q_A^\beta + q_A^\alpha)} \tag{7.26}$$

$$W = -\frac{\frac{r_A^2}{(q_A^\beta + 1)(q_A^\beta + p^\beta)} - \frac{1}{(q_A^\alpha + 1)(q_A^\alpha + p^\alpha)}}{d^2(1 + p^\alpha + \frac{\mu^\beta}{\mu^\alpha}(1 + p^\beta) + \frac{\mu^s k}{\mu^\alpha})(\frac{m_A}{r_A^2} q_A^\beta + q_A^\alpha)}, \quad n \neq 0 \tag{7.27}$$

$$W = -\frac{r_A^2 - 1}{8d^2(1 + \frac{\mu^\beta}{\mu^\alpha} + \frac{\mu^s k}{2\mu^\alpha})(\frac{m_A}{r_A^2} + 1)}, \quad n = 0 \tag{7.28}$$

differ from those of Sternling and Scriven [6] only in sign; these authors have the α phase correspond to positive values of x.

Another interesting case is when $\mathcal{A}$ is insoluble in phase β, $\mathcal{B}$ and $\mathcal{P}$ are insoluble in phase α, and the surface activity of the product is neglected . This corresponds to the limit of $m_i \to 0$, Q_B^α, Q_P^α, Q_A^β all equal to zero, and $\omega = 0$. While this system is a very simplified representation of the complicated chemistry involved in the experiments of Nakache and Dupeyrat, it is felt that it can cast some insight into their experimental observations. It also forms the basis for the remaining analytical analysis. The following expressions are obtained:

$$G = \frac{\frac{(1+\phi_2)(p^\alpha - q_A^\alpha)}{(1+q_A^\alpha)(d^2-1)} - \phi_2 t^2 \frac{(p^\beta - q_B^\beta)}{(q_B^\beta+1)(d^2e^2-t^2)} - s^2 \frac{(p^\beta - q_P^\beta)}{(q_P^\beta+1)(d^2e^2-s^2)}}{q_A^\alpha(1 + \phi_2 + \phi_1)(1 + p^\alpha + \frac{\mu^\beta}{\mu^\alpha}(1 + p^\beta) + \frac{\mu^s k}{\mu^\alpha})}, \quad n \neq 0 \tag{7.29}$$

$$W = \frac{\frac{(1+\phi_2)}{(1+q_A^\alpha)(q_A^\alpha + p^\alpha)} - \frac{\phi_2 t^2}{(q_B^\beta+1)(q_B^\beta+p^\beta)} - \frac{s^2}{(q_P^\beta+1)(q_P^\beta+p^\beta)}}{d^2 q_A^\alpha(1 + \phi_2 + \phi_1)(1 + p^\alpha + \frac{\mu^\beta}{\mu^\alpha}(1 + p^\beta) + \frac{\mu^s k}{\mu^\alpha})}, \quad n \neq 0 \tag{7.30}$$

$$W = \frac{(1 + \phi_2 - t^2\phi_2 - s^2)}{8d^2(1 + \phi_1 + \phi_2)(1 + \frac{\mu^\beta}{\mu^\alpha} + \frac{\mu^s k}{2\mu^\alpha})}, \quad n = 0 \tag{7.31}$$

Dimensionless variables introduced here are

$$d = \sqrt{D_A^\alpha/\nu^\alpha}, \qquad e = \sqrt{\nu^\alpha/\nu^\beta}$$

$$\xi = n/k^2 D_A^\alpha = G/d^2 W$$

$$s^2 = \frac{D_A^\alpha}{D_P^\beta}, \qquad t^2 = \frac{D_A^\alpha}{D_B^\beta}$$

$$\phi_1 = \frac{\theta_1 r_P^2 q_P^\beta}{r_A^2 q_A^\alpha} = \frac{K_{eq} C_{B0} q_P^\beta}{s^2 q_A^\alpha}, \quad \phi_2 = \frac{\theta_2 r_P^2 q_P^\beta}{r_B^2 q_B^\beta} = \frac{K_{eq} C_{A0} t^2 q_P^\beta}{s^2 q_B^\beta}$$

$$q_A^\alpha = \sqrt{1+\xi}, \quad q_B^\beta = \sqrt{1+t^2\xi}, \quad q_P^\beta = \sqrt{1+s^2\xi}$$
$$p^\alpha = \sqrt{1+d^2\xi}, \quad p^\beta = \sqrt{1+d^2e^2\xi}$$

When the diffusion of component $\mathcal{B}$ is very fast, which implies that $t \to 0$ and hence $\phi_2 \to 0$, equations (7.29) and (7.30) simplify to the result for the diffusion of a single component, if it is noted that component $\mathcal{P}$ is equivalent to $\mathcal{A}$ in the β phase. In this case, the partition coefficient m_A is given by $K_{eq}C_{B0}$.

7.7 Analysis of the Characteristic Equation

7.7.1 Physical Significance

Only real values of the dimensionless wave-number, W, have any physical significance, while, in general, the growth rate may be complex : $n = \hat{n} + i\tilde{n}$. The amplitude of the disturbance is determined by $\hat{n}$ while the frequency is determined by $\tilde{n}$.

If $\hat{n} < 0$ the disturbance is damped, while disturbances for which $\hat{n} > 0$ are unstable and are amplified. Two kinds of instability exist. Stationary instabilities occur when $\tilde{n} = 0$ and disturbances grow in place without oscillation. In contrast, oscillatory phenomena occur for $\tilde{n} \neq 0$, in which case the period is $(2\pi)/\tilde{n}$. The disturbance is propagated in the y direction at a speed $\tilde{n}/k$. In the limiting case of $\hat{n} = 0$, there is neutral (marginal) stability and the disturbance neither grows nor decays.

The very nature of the analysis, based on small perturbations, usually restricts the

results to short times, since, as the perturbations grow, non-linear effects may dominate the growth process. It is hoped, however, that observed disturbances will exhibit a wave-number, k_{max}, which is close to that predicted for the maximum growth rate based on the linear stability analysis.

7.7.2 Interpretation

Since we cannot solve explicitly for n, G and W are treated as parametric functions in the variable $\xi = \hat{\xi} + i\tilde{\xi}$.

$$\xi = \frac{n}{k^2 D_A^{\alpha}} = \frac{G}{d^2 W}$$

Since W must be real, the parametric curves of interest are $\tilde{W} = 0$.

To obtain curves describing the various forms of instability in the ($\hat{G}$, $\hat{W}$) plane, the values that ξ can take on must be determined. Various forms of the parametric curve $\tilde{W} = 0$ are shown for the different system parameters in Figure 3, where only the first quadrant is given, since this is the only quadrant that needs to be considered (Sternling and Scriven, 1959). The limiting behaviour of G and W must be obtained to proceed further, as discussed below. This technique provides a systematic way to look for solutions to the problem, although one is not guaranteed to find all solutions.

Limiting Behaviour

A convenient way to identify some of the gross features of the parametric curves of $\tilde{W} = 0$ in the plane $(\hat{\xi}, \tilde{\xi})$ is to find those points at which they intersect the axes. By considering sign changes as $\hat{\xi}, \tilde{\xi} \to 0$ and $\to \infty$ we can conclude whether an even or odd number of roots occurs. From expansions of q_i and p^j in power series of ξ, the limits as $\hat{\xi}, \tilde{\xi} \to 0$ and $\hat{\xi}, \tilde{\xi} \to \infty$ of W and G can be determined. Limiting relationships from which signs at zero and infinity may be deduced are given in Table 7.1.

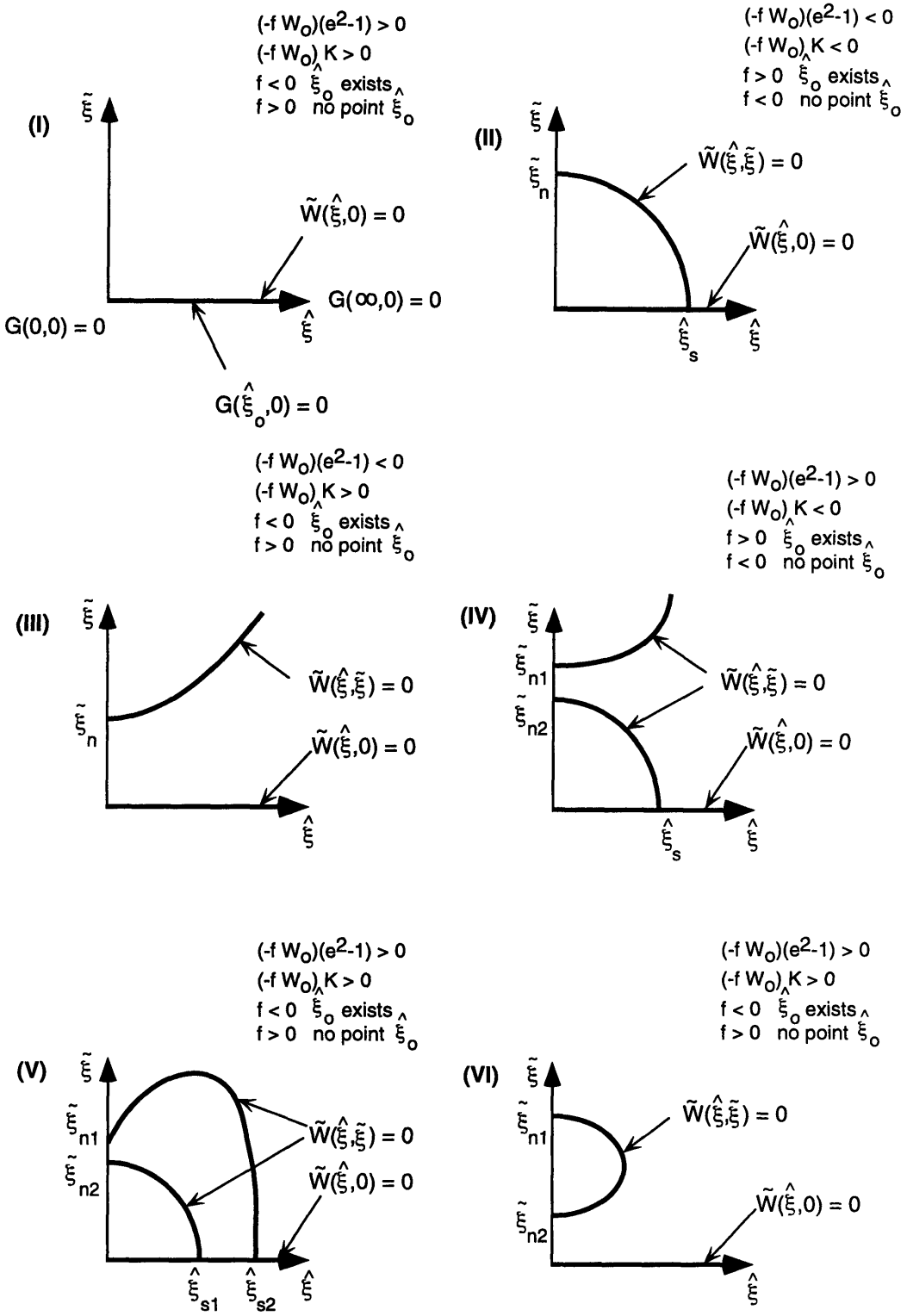

Figure 7-3: Curves of $\tilde{W} = 0$ in the ξ plane. Curves (I)-(III) were orginally presented by Sternling and Scriven [6]. The variables f and K are defined in Table 7.1

Table 7.1: Limiting behaviour of G and W

	$\hat{\xi} = 0$	$\hat{\xi} \to 0$	$\hat{\xi} \to \infty$
$\tilde{\xi} = 0$	–	$\hat{W} = -W_o(1 - f\hat{\xi})$ $\hat{G} = -W_o\hat{\xi}$	$\hat{W} = K\hat{\xi}^{-2}$ $\hat{G} = K\hat{\xi}^{-1}$
$\tilde{\xi} \to 0$	$\tilde{W} = W_o f\tilde{\xi}$	–	–
$\tilde{\xi} \to \infty$	$\tilde{W} = -(e^2-1)\tilde{\xi}^{-\frac{5}{2}}$	–	$\hat{W} = (e^2-1)\hat{\xi}^{\frac{-5}{2}}$ $\tilde{W} = -K\hat{\xi}^{-2}$
$\tilde{\xi} > \hat{\xi}$	–	–	$\hat{W} = -K\tilde{\xi}^{-2}$

where

$$K = \{\phi_2^\infty \frac{(s+de)(e+s)(e^2-t^2)}{(t+ed)(e+t)(e^2-s^2)} + 1\}(e^2-s^2)$$

$$f = (s^2+1)/2 + d^2/4\{(\frac{1+\mu^\beta e^2/\mu^\alpha}{1+\mu^\beta/\mu^\alpha}) + (\tau_1(t^2e^2-1) + (s^2e^2-1))/W_o\}$$
$$+ \frac{\tau_1(t^2-s^2)(t^2-1)}{2W_o(1+\tau_1+\tau_2)}\{(t^2-s^2)/(t^2-1) + 1 + 2\tau_2 + \tau_1\} + \frac{\tau_2 s^2 + \tau_1 + 1}{2(\tau_2+\tau_1+1)}$$

$$W_o = (s^2-1) + \tau_1(t^2-1)$$

$$\tau_1 = K_{eq}C_{A0}t^2/s^2$$

$$\tau_2 = K_{eq}C_{B0}/s^2$$

$$\phi_2^\infty = K_{eq}C_{A0}t/s$$

Curves in the ξ Plane

A qualitative understanding of the curves $\tilde{W} = 0$ is obtained by considering the limiting behaviour of G and W. The two requirements for the stationary state ($\tilde{W} = 0$ and $\tilde{n} = 0$) lead to the conclusion that the real axis ($\tilde{\xi} = 0$) *always* represents such a curve. Furthermore, the real axis corresponds to the only curve of stationary instability. From the definition of G and considering its limiting behaviour it can be shown that $G(0,0) = G(\infty,0) = 0$ which is equivalent to $\hat{n} = 0$. These are neutrally stable points. There may be other neutrally stable points along the real axis depending on the roots of the equation $G(\hat{\xi},0) = 0$. If $\hat{G}(\rightarrow 0,0)$ and $\hat{G}(\rightarrow \infty,0)$ have opposite signs there is at least one additional root of $G(\hat{\xi},0) = 0$ say $\hat{\xi}_0$. There may indeed be an odd number of roots. From the first row of Table 7.1 it is seen that if $-KW_o > 0$, that is, $\hat{G}(\rightarrow 0,0)$ and $\hat{G}(\rightarrow \infty,0)$ have the same sign, there may be zero or an even number of roots of G on the $\hat{\xi}$ axis. These points correspond to additional neutrally stable points.

Similar criteria can be applied for the intersection of the curve $\tilde{W} = 0$ with the imaginary axis. From the first column of Table 7.1, it is apparent that, if $\tilde{W}(0,\infty)$ and $\tilde{W}(0,0)$ are of opposite sign ($-fW_o(e^2 - 1) < 0$), then one may expect at least one intersection with the imaginary axis. This point is labelled $\tilde{\xi}_n$. In the case where the oscillatory curve intersects the real axis, this point represents a singular point in $\tilde{W}$ and corresponds to a local extremum in W. The necessary condition [6, 7] is that $\frac{\partial \hat{W}}{\partial \hat{\xi}} = 0$. Let $\hat{\xi}_s$ represent such a point. When $-fW_oK > 0$ no such point exists. Note that for $f > 0$ the condition for a singular point is equivalent to that for the existence of a root of $G(\hat{\xi}_0,0) = 0$. These arguments were used to derive the curves shown in Figure 3.

Curves **(I)**-**(III)** in Figure 3 were originally presented by Sternling and Scriven [6], who could show for their characteristic equation that only a single point $\hat{\xi}_o$ could exist. In addition, they ruled out the possibility of additional curves $\tilde{W} = 0$ intersecting the imaginary axis on physical grounds, since this would require the existence of more than one neutrally stable oscillatory disturbance. In our system we can no longer discount this possibility. In fact, since we are dealing with a situation of two chemical species diffusing to an interface where they react to form a product, we may expect a *combination* of the curves in the complex plane owing to the linear nature of the analysis.

The new curves that have been identified in the complex plane are presented in Figure 3,

labelled as **(IV)** through **(VI)**. Curve **(IV)** is clearly a combination of curves **(II)** and **(III)** and is characterised by a single root (representing a singular point) on the $\hat{\xi}$ axis. The parametric curve $\tilde{W} = 0$ also crosses the $\tilde{\xi}$ axis twice. The presence of multiple roots severely restricts conclusions that may be drawn merely by looking at the sign of limiting values of W and G. This difficulty is clearly demonstrated by curve **(V)** which has double roots on the real and imaginary axis and hence the same limiting signs as for curve **(I)**.

More curves likely exist in the complex plane, but only those curve types that have actually been observed in the numerical solution of the problem are presented here. For convenience these curves are referred to by specifying Type **(number)** in subsequent sections.

7.7.3 Curves in the Plane $(\hat{W}, \hat{G})$

Physically the wave-number k^2 must be positive. For disturbances that are amplified or are neutral we must consider $\hat{n} \geq 0$. As a result $\hat{G}$ and $\hat{W}$ have the same sign. Curves of $\hat{G}$ versus $\hat{W}$ thus occur in the first or the third quadrant. The third quadrant corresponds to the situation where ζ andQ_A^α have opposite sign. Since $\zeta < 0$, that is component $\mathcal{A}$ is surface active, the third quadrant corresponds to positive Q_A^α. Curves in the third quadrant represent $\mathcal{P}$ diffusing to the interface to form $\mathcal{A}$ and $\mathcal{B}$ which then diffuse away from the interface. If Q_A^α is negative, relevant curves appear in the first quadrant and correspond to component $\mathcal{A}$ and $\mathcal{B}$ diffusing towards the interface.

The curves in the $(\hat{W}, \hat{G})$ plane shown in Figure 4 enable one to investigate the dependence of the amplification factor $(\hat{n})$ on the wave-number (k). The curves of stationary instability are drawn in solid lines while oscillatory phenomena are shown by the dashed lines. Only curves with positive W_o are shown, since curves of negative W_o are identical except for an exchange between the first and third quadrants.

To determine the location of the stationary instability curve, we note from Table 7.1 that for $(\hat{\xi} \to 0, \tilde{\xi} = 0)$, $\hat{W} \to -W_o$ and $\hat{G} \to 0$. This represents a neutrally stable point which intersects the $\hat{W}$ axis at $-W_o$. As $(\hat{\xi} \to \infty, \tilde{\xi} = 0)$ both $\hat{W}$ and $\hat{G} \to 0$ from the side of sign(K). If the point $\hat{\xi}_o$ exists, the stationary instability curve will pass through the origin twice. Using these simple arguments, an idea of the form of the stationary curves may be obtained.

In drawing the oscillatory instability curves, it is convenient to know the sign of $\hat{W}(0, \tilde{\xi}_n)$.

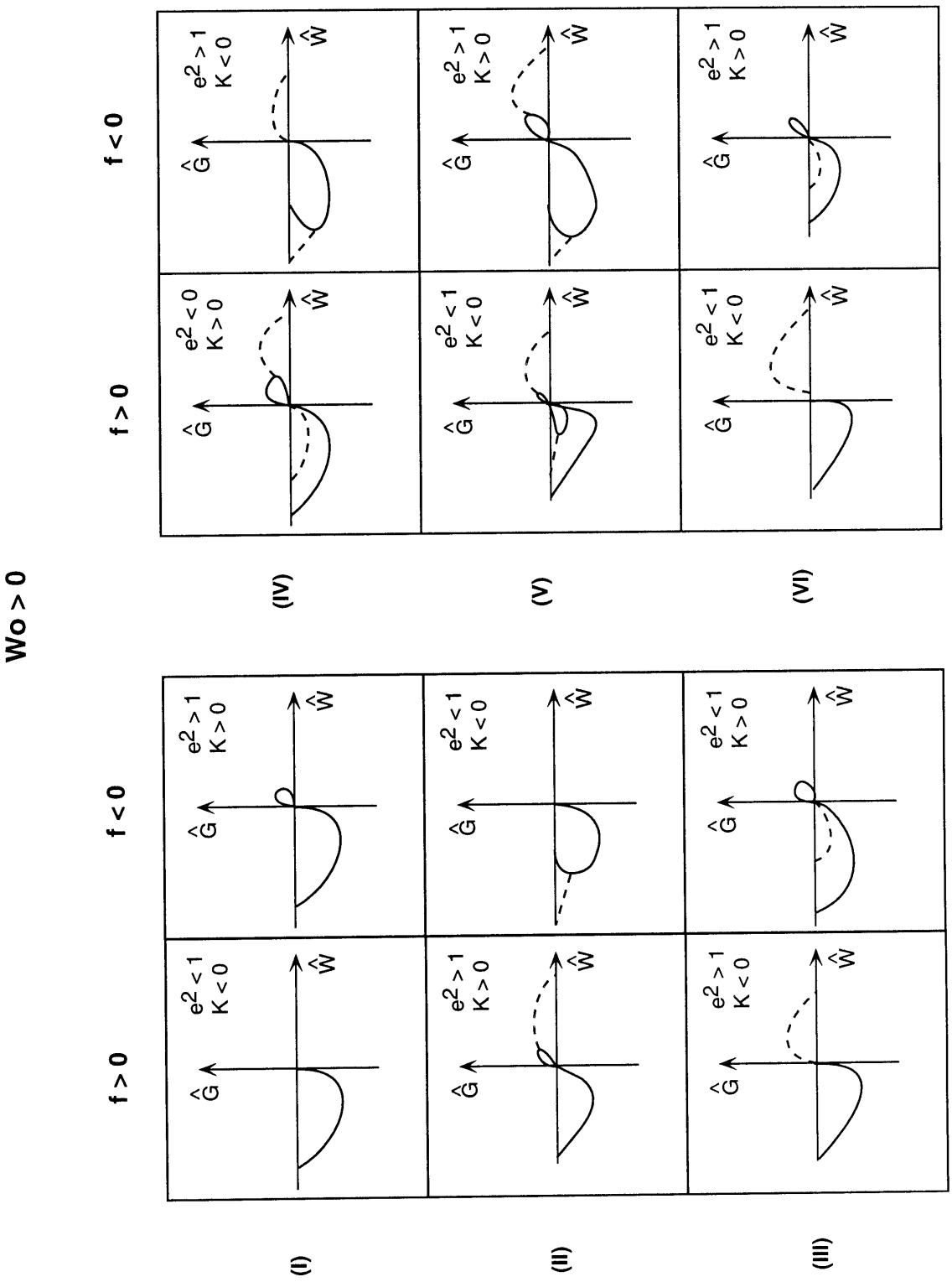

Figure 7-4: Amplification versus wave-number plots for $W_o > 0$. Curves for $W_o < 0$ are obtained by exchanging curves in the first and third quadrants.

Unfortunately the sign of the term actually depends on the magnitude of $\tilde{\xi}_n$ which is inaccessible in general. The shape and location of these curves are inferred based on two criteria. If the parametric curve $\tilde{W} = 0$ intersects the stationary instability curve, that is the point $\hat{\xi}_s$ exists, it is possible to draw two conclusions: (i) The oscillatory instability curve must intersect the stationary instability curve in $\hat{G}$, $\hat{W}$ coordinates, and (ii) the point of intersection must be an extremum for $\hat{W}$. Alternatively, if the curve in the complex plane asymptotically approaches that of a parabola (curve **(III)** in complex plane), the oscillatory instability curve approaches the origin in the $(\hat{W}, \hat{G})$ plane from the $-K$ side. These arguments were used to generate the oscillatory instability curves.

7.8 Numerical Solutions

7.8.1 Program Strategy

Two strategies were employed in order to determine the solutions to the characteristic equations. They will briefly be discussed in the subsequent sections.

Determine Curves in ξ Plane

Once the values of all physical variables have been set, the limiting behaviour is calculated and based on this information we know what type of curves we may expect in the complex plane. To obtain the stationary instability curve we simply choose a set of values $\hat{\xi}$ which span the entire axis and evaluate $\hat{G}$ and $\hat{W}$. Determining the oscillatory curves is somewhat more difficult. First we determine roots of $\tilde{W} = 0$ on the $\tilde{\xi}$ axis. This is done using the bisection method. Once we have determined the intersection point we simply repeat the procedure for different values of $\hat{\xi}$. At each step in the process the variables $\hat{G}$ and $\hat{W}$ are evaluated together with the velocity and concentration eigenvectors.

Finding minima of F^2 for a particular value of k

Rewriting the characteristic equation (Eq. 7.23) in the form $F(n,k) = 0$, it can be shown that the minima of $F^2 = FF^*$ correspond to the roots of the equation $F(n,k) = 0$ [17]. For a particular value of the wavenumber k, we use the simplex algorithm to determine the location of the minimum of F^2. This is clearly a two dimensional minimization problem since $\hat{n}$ and $\tilde{n}$ need to be determined. Initially we start off with an arbitrary set of three points specifying the vertices of the simplex triangle. If we converge to the minimum, we increment k and repeat the procedure using the previous minimum as a starting point. This ensures that once we jump onto a curve of $F^2 = 0$ we actually stay on it for all values of k. The initial simplex triangle is determined by trial and error. Irrespective of the initial guess one does reach a minimum, but the minimum may correspond to curves in the second and fourth quadrants of the $(\hat{W}, \hat{G})$ plane.

7.9 Results and Discussion

To sample the entire parameter space is clearly a huge task. In an attempt to understand the observed instability in the experimental system of Nakache *et al.*, the variable space was restricted to that corresponding to the experimental system. Table 7.2 contains estimates of all relevant physical quantities and Table 7.3 contains the resulting dimensionless variables used.

Table 7.2: Physical constants

Variable	α - phase (water)	β - phase (nitrobenzene)
ρ (kg/m^3)	998[a]	1204[b]
$\mu \times 10^3$(kg/m.s)	1.002[a]	2.03[b]
$D_A \times 10^{10}$(m^2/s)	3.8[c]	3.0[c]
$D_B \times 10^{10}$(m^2/s)	8.2[c]	6.6[c]
$D_P \times 10^{10}$(m^2/s)	3.4[c]	2.8[c]

[a]Rogers, G. F. C. and Mayhew, Y. R. , Thermodynamic and Transport Properties of Fluids, Basil Blackwell, 1980

[b]CRC Handbook of Chemistry and Physics, D. R. Lide, 73 Edition, CRC Press, Ann Arbor, 1993

[c]Calculated using Wilke Chang group contribution techniques, Reid, R. C.; Sherwood, T. K. *The Properties of Gases and Liquids*, McGraw-Hill : New York, 1958. $A = C_{16}^{+}Cl^{-}$, $B = H^{+}Pi^{-}$, and$P = C_{16}^{+}Pi^{-}$

The three unknown physical parameters represent the the limiting concentrations of components $\mathcal{A}$ and $\mathcal{B}$ as the interface is approached, namely C_{A0} and C_{B0}, and the equilibrium constant K_{eq} for the interfacial reaction.

7.9.1 Varying K_{eq}

As a first step it was assumed that $C_{A0} = 5 \times 10^{-3}$ and $C_{BO} = 1.5 \times 10^{-3}$M while K_{eq} was varied. The concentrations were chosen to correspond to the experimental system. Only the magnitude of the product $K_{eq}C_{i0}$ is important (i is compenent A or B). The results are shown in Figure 5(a)-(c).

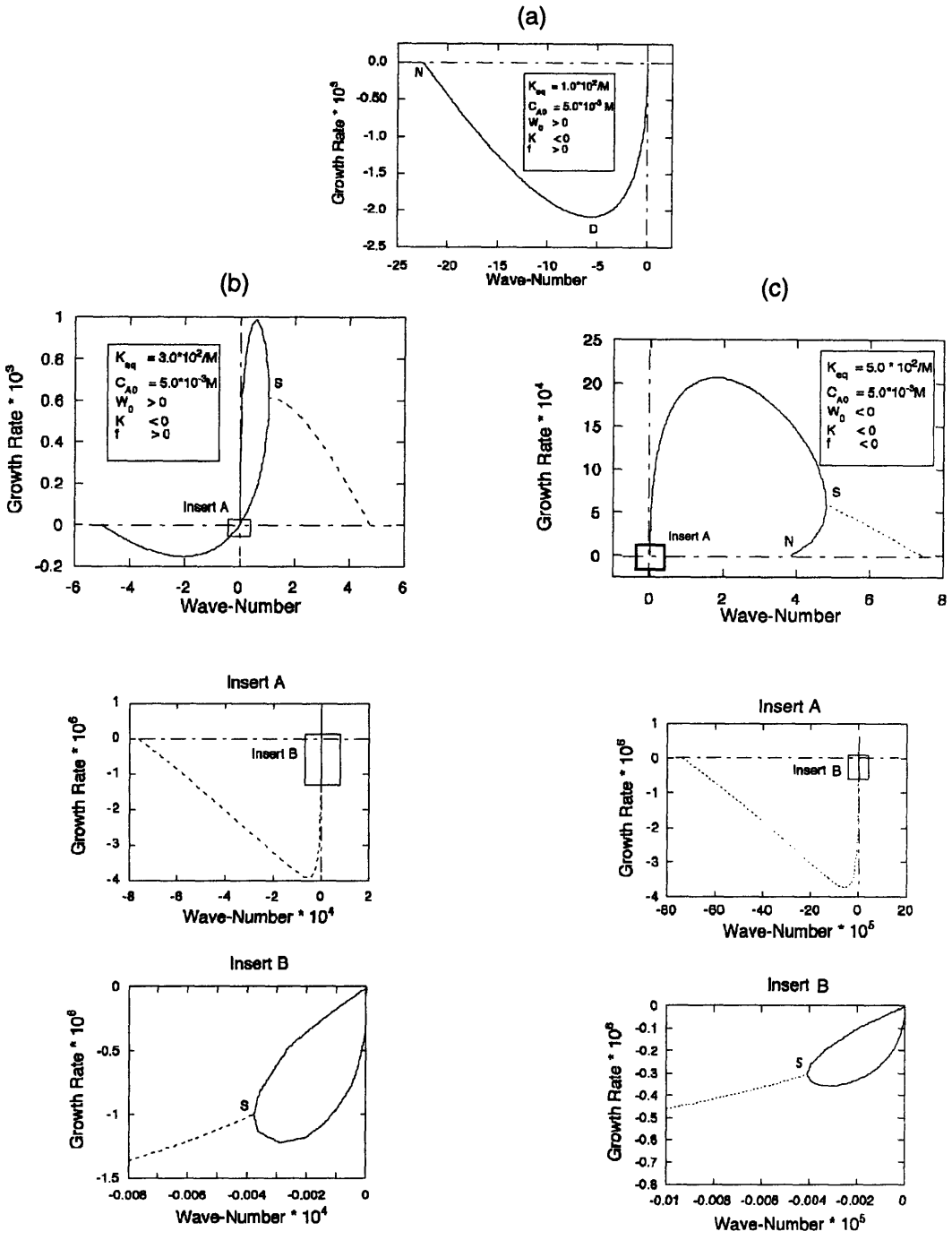

Figure 7-5: Effect of variations in K_{eq} on the growth rate ($\hat{G}$) versus wave-number ($\hat{W}$) plots for $C_{A0} = 5 \times 10^{-3}$M and $C_{B0} = 1.5 \times 10^{-3}$M. (a) $K_{eq} = 1.0 \times 10^2$/M, Type **(I)**. Single stationary curve in third quadrant. (b) $K_{eq} = 3.0 \times 10^2$/M, Type **(V)**, (c) $K_{eq} = 5.0 \times 10^2$/M, Type **(V)**.

Table 7.3: Value of dimensionless variables

Variable	Value
e^2	0.595
t^2	0.568
s^2	1.36
$d^2 \times 10^4$	3.8

For small values of the equilibrium constant ($K_{eq} \leq 1.0 \times 10^2$), the system has a single stationary instability in the third quadrant (Figure 5(a)), corresponding to a curve of Type **(I)** in the ξ plane. Point N corresponds to a neutrally stable point while point D represents the maximum growth rate and hence dominant disturbance. The system is stable to all disturbances in the first quadrant. If the equilibrium constant is increased three-fold, the situation changes considerably and corresponds to a Type **(V)** curve, as shown in Figure 5(b). Note that the limiting signs are unchanged. The stationary instability curve is unique in that it has a **triple** root at the origin causing two closed loops to develop, each of which is intersected by an oscillatory curve. Of particular interest is the large variation in the order of the wave-numbers and growth rates for these curves. Although this system does have an oscillatory instability in the first quadrant, the dominant growth rate corresponds to a stationary state.

As K_{eq} is increased to 5.0×10^2, the stationary loop in the first quadrant grows at the expense of the stationary loop in the third quadrant. Eventually a neutrally stable point N develops in the first quadrant (Figure 5(c)). There exists only a single closed loop for the stationary curve, restricted to the third quadrant. Two oscillatory curves still intersect the stationary curve at local maxima of $\hat{W}$, one in each quadrant (represented by points S in Figure 5(c)). As K_{eq} is further increased, the neutrally stable point N moves to higher wave-numbers until there is no longer a local maximum of $\hat{W}$ in first quadrant, and hence no oscillatory instability in the first quadrant. The closed loop in the third quadrant eventually disappears as K_{eq} is increased further. It is interesting to note how the curves in the ξ plane change. With increasing K_{eq}, Type **(I)**, **(V)**, **(II)** and finally **(III)** curves are spanned.

7.9.2 Varying C_{A0} for $K_{eq} = 1.0 \times 10^2$

The stability behaviour changes considerably with increases in the concentration of component $\mathcal{A}$ at the interface. Initially the entire first quadrant is stable for $C_{A0} = 5.0 \times 10^{-3}$M as shown in Figure 5(a). As the concentration increases slightly to $C_{A0} = 6.5 \times 10^{-3}$M, the first quadrant has only an oscillatory curve as shown in Figure 6(a). For small wave-numbers, the system is stable, however. This is the only curve in which the oscillatory instability is also the dominant instability in the first quadrant. At higher concentrations, a large stationary curve dominates the first quadrant (Figure 6(b)). In summary, by increasing concentration, curves of Type **(I), (VI), (V)** are spanned.

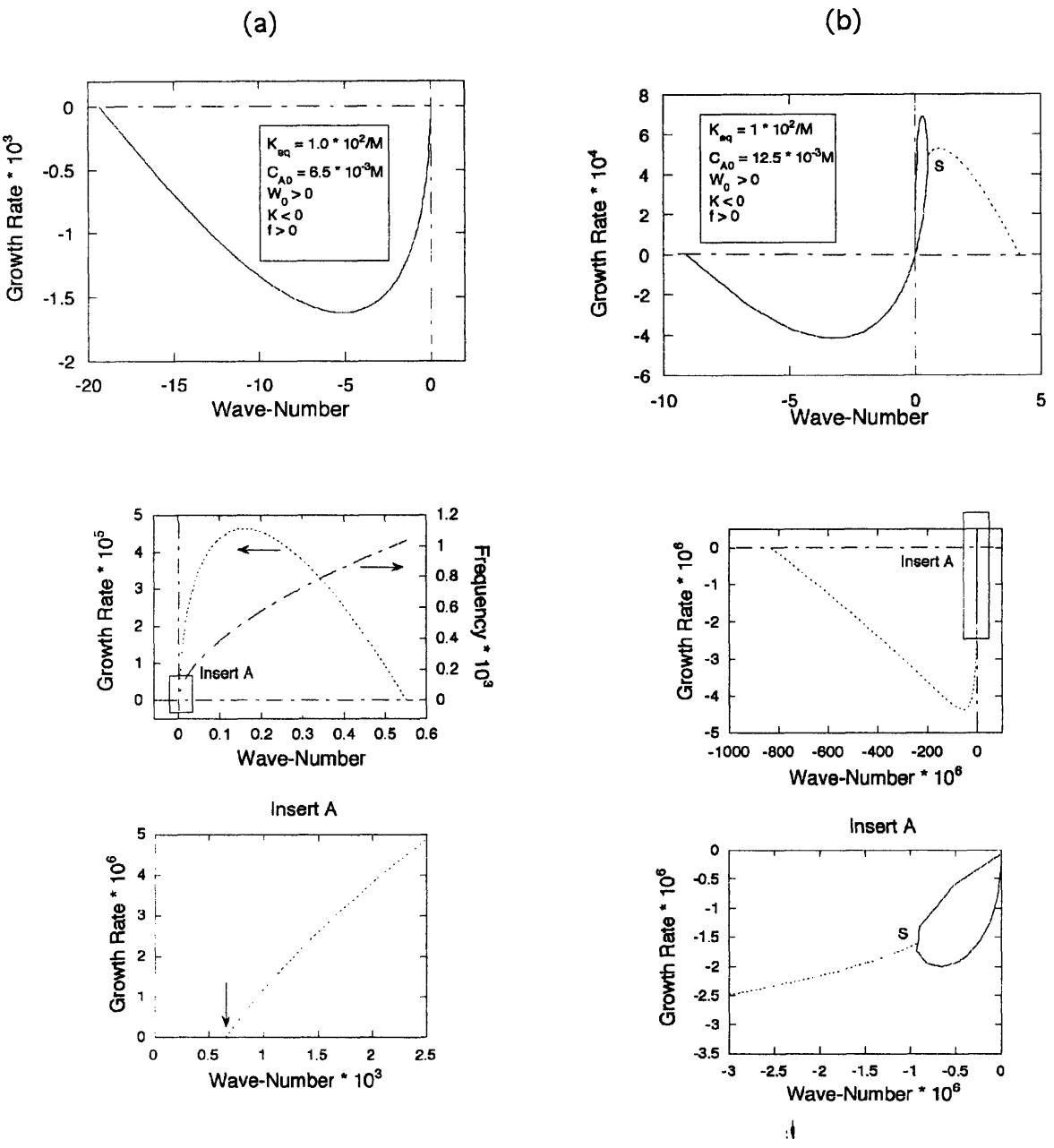

Figure 7-6: Effect of variations in C_{A0} on the growth rate versus wave-number plots for $C_{B0} = 1.5 \times 10^{-3}$M and $K_{eq} = 1 \times 10^2$/M. (a) $C_{A0} = 6.5 \times 10^{-3}$M, Type **(VI)**. Oscillatory instability in first quadrant, but stable for very small wave-numbers. (b) $C_{A0} = 12.5 \times 10^{-3}$M, Type **(V)**.

7.9.3 Disturbance Propagation

The stationary state is characterised by an increase in the concentration of species $\mathcal{A}$ at points on the interface where flow is directed towards the interface. As a result the surface tension is lowered, resulting in flow along the interface to regions with lower $\mathcal{A}$ concentration. Regions in which $\mathcal{A}$ is depleted correspond to areas in which the bulk flow is away from the interface. This is depicted schematically in Figure 7. The concentration variations thus promote the velocity perturbations, resulting in the disturbance being amplified. In the stationary state, the velocity and concentration variations are in phase, and the disturbance grows in place. For the oscillatory regime, the concentration variations and the velocity perturbations are slightly out of phase. The phase shift, of order 0.1 degrees, is surprisingly small and results in the disturbance being propagated in the negative y-direction.

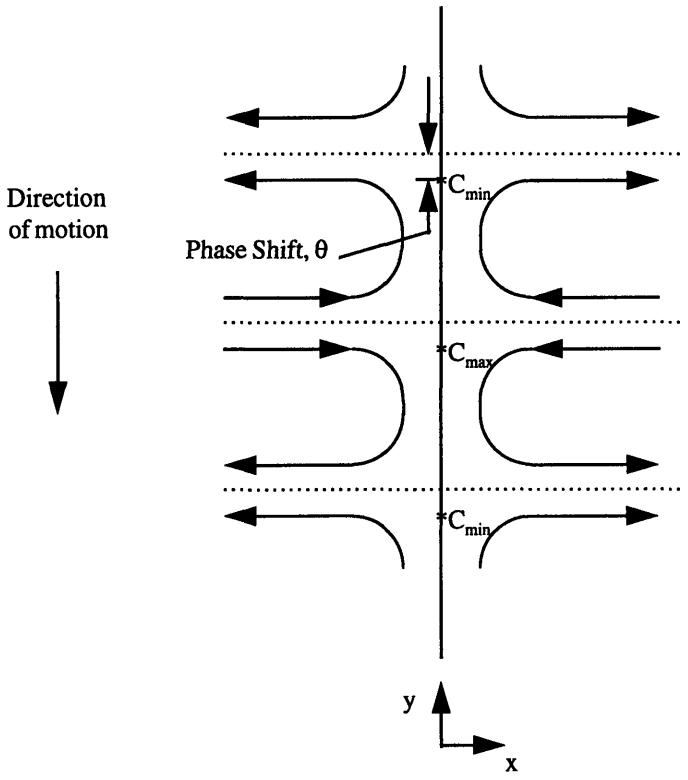

Figure 7-7: Imposed velocity perturbations and resulting phase shift in concentration variations.

7.9.4 Comparison to Experimental Results

Nakache *et al.* [24] noted that oscillations appear only in a narrow concentration range, from $1. \times 10^{-4}$M to $4. \times 10^{-4}$M for CTA^+Cl^- and from $1. \times 10^{-4}$M to $1. \times 10^{-3}$M for H^+Pi^-. The stability results shown in Figure 5(a), 6(a), 6(b) display a similar sensitivity to concentration changes. Based on order of magnitude estimates for Q_A^α and ζ ($Q_A^\alpha = -10^5 \text{mol/m}^4$ and $\zeta = -10^{-2}\text{m}^3/\text{s}^2$), the period ($2\pi/\tilde{n}$) at the maximum growth rate in Figure 6(a) was found to be 0.5 s. In addition, the λ_{max} was calculated to be 0.2 mm, the amplification factor 1.35/s ($\hat{n}$) and the speed of propagation 0.4 mm/s ($\tilde{n}/k$). Experimental values of the period range from a few seconds to minutes and the size of the disturbance may range from millimeters to centimeters. The period and λ_{max} are in good qualitative agreement with experimental values, but are about 10 fold smaller. Sources of error include estimation of diffusion coefficients, concentration coefficient of surface tension (ζ) and the slope of the concentration profile (Q_A^α). Edge effects which are neglected in this analysis may also be significant in the experimental system. In addition, and perhaps most importantly, the linear analysis can describe only the onset of instability since it neglects higher order effects.

Experimentally it was found by Kai *et al.* [27], that the frequency and amplitude of the disturbance increased with increasing concentration product, $C_{A0}C_{B0}$. The stability analysis predicts an increase in the growth rate and frequency of the oscillation with increasing C_{A0} at constant C_{B0} (Figure 6(a)-(b)).

The sensitivity to the equilibrium constant, K_{eq}, was demonstrated in Figures 5(a)-(c). This could explain why oscillations are still observed when picric acid is replaced by KI, but not by KBr. The exchange reactions are expected to have different equilibrium constants which will affect the stability behaviour. Nakache *et al.* [24, 25] also noted that on replacement of picric acid by potassium picrate, oscillations were no longer evident. It was noted that the dissociation constant for potassium picrate in nitrobenzene exceeds that for picric acid by a factor of 10^3, leading to radically different interfacial concentrations.

7.10 Conclusion

For systems in which a rapid, reversible interfacial reaction is controlled by diffusion of the two reacting species toward the interface, a linear stability analysis predicts oscillatory instabilities over a narrow concentration range only, and over a narrow range of reaction

equilibrium constant values, in accord with reported experimental observations. It is unnecessary to invoke non-linear reaction schemes or electrostatic effects to account for the observed behaviour. It is recognised that the reactions under consideration are diffusion controlled, not adsorption controlled, and that specific chemical effects can be accounted for directly through the equilibrium constants values. Electrostatic effects appear not to be important since small changes in the chemical make-up of the system (e.g., KI versus KBr, which are similar electrostatically) can lead to dramatic changes in the stability of the interface.

Nomenclature

Regular Characters

A_1 : Constant of integration, for $n \neq 0$, [m/s]
A_2 : Constant of integration, for $n = 0$, [m/s]
$A = (r_A^2 q_A^\alpha + m_A q_A^\beta)$: [-]
$B = (r_B^2 q_B^\beta + m_B q_B^\alpha)$: [-]
C_i : concentration of species i, [mol/l]
C_{i0} : concentration of component i at interface, [mol/l]
$\tilde{C}_i^j$: steady state concentration profile of species i in phase j
$d = \sqrt{D_A^\alpha / \nu^\alpha}$: [-]
$\frac{D}{Dt}$: substantial derivative $= \frac{\partial}{\partial t} + \mathbf{v} \cdot \nabla$
D_i^j : diffusivity of component i in phase j, [m^2/s]
$e = \sqrt{\nu^\alpha / \nu^\beta}$: [-]
$G = (\frac{\mu^\alpha}{\zeta Q_A^\alpha}) n$: dimensionless growth rate, [-]
$H_i^j(x)$: conc. perturbation coefficient, component i in phase j, [mol/l]
k : wave-number, [m^{-1}]
k_{max} : wave-number at maximum growth rate, [m^{-1}]
K_{eq} : equilibrium concentration, [l/mol]
m_i : partition coefficient of component i, [-]
$n = \hat{n} + i\tilde{n}$: complex growth rate, [s^{-1}]
$p^j = \sqrt{1 + \frac{n}{k^2 \nu^j}}$: [-]
P : pressure, [Pa]
$P = (m_P q_P^\alpha + r_P^2 q_P^\beta)$: [-]
$q_i^j = \sqrt{1 + \frac{n}{D_i^j k^2}}$: [-]
Q_i^j : slope of concentration profile, component i in phase j, [mol/m^4]
$r_A^2 = \frac{D_A^\alpha}{D_A^\beta}$: [-]
$r_B^2 = \frac{D_B^\beta}{D_B^\alpha}$: [-]
$r_P^2 = \frac{D_P^\beta}{D_P^\alpha}$: [-]
$s^2 = \frac{D_A^\alpha}{D_P^\beta}$: [-]
S_B^β : slope of steady state profile of component $\mathcal{B}$ in phase β, [mol/m^4]
S_P^β : slope of steady state profile of component $\mathcal{P}$ in phase β, [mol/m^4]
t : time, [s]
$t^2 = \frac{D_A^\alpha}{D_B^\beta}$: [-]
$U^j(x)$: x component coefficient of velocity perturbation in phase j, [m/s]
$\mathbf{v}$: velocity vector [m/s]
v_i^j : velocity component in i direction in phase j, [m/s]
$V^j(x)$: y component coefficient of velocity perturbation in phase j, [m/s]
$W = (\frac{\nu^\alpha \mu^\alpha}{\zeta Q_A^\alpha}) k^2$: dimensionless wave-number, [-]
x, y, z : spatial coordinates, [m]
X, Y, Z : dimensionless spatial coordinates wrt k, [-]

Greek characters

α, β	: refer to liquid phases (water, oil)
ϵ	: shear viscosity, [kg/s]
$\zeta = \frac{\partial \sigma_0}{\partial C_A^\alpha}$	: concentration coefficient $\mathcal{A}$ of interfacial tension,[m^3/s^2]
$\theta_1 = \frac{KeqC_{B0}D_P^\alpha}{D_A^\beta}$	: [-]
$\theta_2 = \frac{KeqC_{A0}D_P^\alpha}{D_B^\alpha}$	: [-]
κ	: dilational viscosity, [kg/s]
λ	: wavelength $= 2\pi/k$, [m]
λ_{max}	: wavelength at maximum growth rate $= 2\pi/k$, [m]
μ	: dynamic viscosity, [kg/ms]
ν	: kinematic viscosity, [m^2/s]
$\xi = \frac{nk^2}{D_A^\alpha}$	: $= \frac{G}{d^2W}$, parameterising variable, complex
ρ	: fluid density, [kg/m^3]
σ_0	: surface tension, [N/m=kg/s^2]
τ_{xy}^j	: component x,y of stress tensor, [kg/ms^2]
$\phi_1 = \frac{\theta_1 r_P^2 q_P^\beta}{r_A^2 q_A^\alpha}$	: [-]
$\phi_2 = \frac{\theta_2 r_P^2 q_P^\beta}{r_B^2 q_B^\beta}$	: [-]
$\omega = \frac{1}{\zeta}\frac{\partial \sigma_0}{\partial C_P^\beta}$	: relative concentration coefficient, [-]
∇	: del operator $= \mathbf{i}\frac{\partial}{\partial x} + \mathbf{j}\frac{\partial}{\partial y} + \mathbf{k}\frac{\partial}{\partial z}$, [$m^{-1}$]

Script characters

$\mathcal{A}$	: component A, cetyltrimethylammonium chloride $C_{16}^+Cl^-$
$\mathcal{B}$	: component B, picric acid, H^+Pi^-
$\mathcal{P}$	: component P, complex product, $C_{16}^+Pi^-$

Bibliography

[1] L. E. Scriven and C. V. Sternling, Nature **187,** pages 186–188 (1960).

[2] J. R. A. Pearson, Journal Fluid Mechanics **4,** pages 489–500 (1958).

[3] J. C. Berg and A. Acrivos, Chemical Engineering Science **20,** 737 (1965).

[4] L. E. Scriven and C. V. Sternling, Journal of Fluid Mechanics **19,** pages 321–340 (1964).

[5] K. A. Smith, Journal Fluid Mechanics **24,** pages 401–414 (1966).

[6] C. V. Sternling and L. E. Scriven, A.I.Ch.E. Journal **5,** pages 514–523 (1959).

[7] E. Ruckenstein and C. Berbente, Chemical Engineering Science **19,** pages 329–347 (1964).

[8] P. L. T. Brian, AIChE Journal **17,** pages 765–772 (1971).

[9] P. L. T. Brian and K. A. Smith, AIChE Journal **18,** pages 231–233 (1972).

[10] A. Steinchen-Sanfeld and A. Sanfeld, Chemical Physics **1,** pages 156–160 (1973).

[11] W. Dalle Vedove, P.M. Bisch, and A. Sanfeld, Journal of Non-Equilibrium Thermodynamics **5,** pages 35–53 (1980).

[12] A. Sanfeld and A. Steinchen, Faraday Discussion of Chemical Society **77,** pages 169–179 (1984).

[13] A. Sanfeld, A. Steinchen, M. Hennenberg, P. M. Bisch, and D. Van Lamesweerde-Gallez, Lecture Notes in Physics **105,** pages 168–204 (1979).

[14] M. Sakata and T. Funada, Journal of the Physical Society of Japan **50,** pages 696–702 (1981).

[15] T. Funada and M. Sakata, Journal of the Physical Society of Japan **57,** pages 476–489 (1988).

[16] M. Hennenberg, T. S. Sorensen, and A. Sanfeld, Journal of the Chemical Society Faraday Transactions II **73,** pages 48–66 (1977).

[17] T. S. Sorensen, F. Y. Hansen, J. Nielsen, and M. Hennenberg, Journal of the Chemical Society Faraday Transactions II **73,** pages 1589–1601 (1977).

[18] T. S. Sorensen, M. Hennenberg, and F. Y. Hansen, Journal of the Chemical Society Faraday Transactions II **999,** 1005 (1978).

[19] John T. Davies and E. K. Rideal, *Interfacial Phenomena*, (Academic Press, New York, 1963).

[20] A. Orell and J. W Westwater, American Institute of Chemical Engineers **8,** 350 (1962).

[21] P.M. Bisch, D. van Lamsweerde-Gallez, and A. Sanfeld, Journal of Colloid and Interface Science **71,** pages 501–512 (1979).

[22] D. van Lamsweerde-Gallez, P.M. Bisch, and A Sanfeld, Journal of Colloid and Interface Science **71,** pages 513–521 (1979).

[23] C. A. Miller and L. E. Scriven, Journal of Colloid and Interface Science **33,** pages 360–370 (1970).

[24] Evelyne Nakache, Monique Dupeyrat, and Michele Vignes-Adler, Journal of Colloid and Interface Science **94,** pages 187–200 (1983).

[25] Evelyne Nakache, Monique Dupeyrat, and Michele Vignes-Adler, Faraday Discuss. Chem. Soc. **77,** pages 189–196 (1984).

[26] Shoichi Kai, Eiji Ooishi, and Masahide Imasaki, Journal of the Physical Society of Japan **54,** pages 1274–1281 (1985).

[27] Shoichi Kai, Stefan Muller, Toshio Mori, and Mutsumaru Miki, Physica D **50,** pages 412–428 (1991).

[28] M Dupeyrat and E Nakache, Physicochemical Hydrodynamics **2,** pages 591–597 (1977).

[29] J. van Hunsel, G. Bleys, and P. Joos, Journal of Colloid and Interface Science **114,** 432 (1986).

[30] Donn N. Rubingh and Paul M. Holland, *Surfactant Science Series, Cationic Surfactants, Physical Chemistry*, (Marcel Dekker, Inc.: New York, 1991).

[31] L. E. Scriven, Chemical Engineering Science **12,** pages 98–108 (1960).

Chapter 8

Summary and Future Directions

In this thesis we have investigated the self-assembly of short model amphiphiles of type A_2B_2 using stochastic dynamics (SD) simulations. The use of SD is inspired by the fact that the explicit incorporation of the solvent molecules is computationally too intensive. Furthermore, the time scales associated with solvent motion is orders of magnitude faster than those in micellar systems. In this work, therefore, the solvent effect is accounted for in an approximate manner using a stochastic noise term and a solvent modified interaction potential. Although a sound theoretical basis exists for projecting out the rapidly varying degrees of freedom associated with the solvent, the resulting exact expressions are still intractable and one must resort to simplified and often *ad hoc* modifications of these expressions. In our work, we have assumed that the system can be characterized by a delta correlated memory function, which is clearly unphysical at short times, but yields diffusive dynamics at long times.

The ability of SD simulations to provide equilibrium thermodynamic and structural properties of micellar systems was demonstrated in Chapter 4. The micelle structures formed spontaneously and the simulations were not confined to a lattice. The approach is quite general and may be applied to branched surfactants and to mixed surfactant systems. These simulations correspond to gas phase MD simulations (NVT ensemble) since bare Lennard-Jones (LJ) interaction potentials were employed and no attempt was made to include the structure of solvent through a potential of mean force. The micelle structure, size distribution and critical micelle concentrations are directly accessible from such simulations and provides a tool for evaluating the effect of amphiphile structure on micelle formation and

the means to validate existing theoretical expressions that are used to explain micellization. The simulation of triblock copolymers with a insoluble interior block ($A_iB_jA_k$) would serve as an interesting system to study, as would the solubilization capacity of such model micellar systems. As the chain length increases and/or the aggregation number rises, larger systems and longer simulations are required. Care should be taken that the system under study should not undergo macroscopic phase separation. Simulations of order 1000 chains with 20 beads per chain represent the present computational limit.

The dynamics of micelle formation and dissolution were investigated by computer temperature jump "experiments" in Chapter 5. By tagging surfactants or determining the free energy profile for chain extraction, surfactant entry and exit rates could be calculated. By performing such simulations, existing theories could be tested against the simulation results. An example was provided by using the Aniansson -Wall model to predict the time evolution of the system in response to a temperature perturbation which could then be directly compared to the simulation results. These ideas could be extended to probe micelle-micelle coalescence, the exchange of solubilizate between micelles and the effect of cosurfactants on the mechanism of micelle dissolution. Only through such simulations can we obtain a direct molecular level understanding of the dynamics involved in self-assembled systems. Future work should focus on using the obtained free energy profile for chain extraction in conjunction with rate theory (e.g. Kramers' theory) to determine the surfactant exit rate constants. Further evaluation of free, associated surfactant and micelle diffusion coefficients is still required.

In Chapter 6 we dealt with the incorporation of solvent effects into SD simulations. By studying single chains (length N= 4 - 16) and multiple chain systems in associating and non-associating conditions we were able to demonstrate that using a potential of mean force in SD simulations enabled the exact MD results to be recovered. This approach is inherently flawed since it relies on the superposition approximation. In all the cases that we considered, the interactions could be subdivided into a direct solute-solute contribution which could be explicitly accounted for in the simulations and a background PMF contribution which corresponded to a LJ repulsive system. The greatest challenge in using SD simulations to model realistic systems, lies in the incorporation of solvent effects in an exact manner. The use of liquid-state theory or density functional theory seems an appropriate route to pursue and one may visualize a two tiered approach, where the surfactant molecules are accounted

for using SD simulations while the solvent is modeled as a continuum via density functional theory. This approach would also facilitate the modeling of interfacial behaviour.

A problem closely related to the formation of micelles is the behaviour of surfactant laden interfaces. The transport of surface active solutes across an interface may affect th e stability of the interface. A particular example of how reacting species may affect interfacial stability is considered in Part II of the thesis using a continuum approach. The implementation of molecular level simulations of surfactant interfaces and transport across such an interface would be a natural extension of the work described in Part I of the thesis.